SAPIENZA
UNIVERSITÀ DI ROMA

SEARCHES FOR HIGH ENERGY NEUTRINOS FROM GRB130427A WITH THE ANTARES NEUTRINO TELESCOPE

Facoltà di Scienze Matematiche, Fisiche e Naturali

Corso di Laurea Magistrale in Astronomia e Astrofisica

Candidate

Silvia Celli

ID number 1419462

Thesis Advisor

Prof. Antonio Capone

Academic Year 2014/2015

SEARCHES FOR HIGH ENERGY NEUTRINOS FROM GRB130427A WITH THE ANTARES NEUTRINO TELESCOPE
Master thesis. Sapienza – University of Rome

This thesis has been typeset by LaTeX and the Sapthesis class.

Author's email: silvia.celli@roma1.infn.it

To my parents.

"Pronaque cum spectent animalia cetera terram,
os homini sublime dedit caelumque videre
iussit et erectos ad sidera tollere vultus."
Ovidio, Metamorfosi

"I do not know what I may appear to the world,
but to myself I seem to have been
only like a boy playing on the sea-shore,
and diverting myself in now and then
finding a smoother pebble
or a prettier shell than ordinary,
whilst the great ocean of truth
lay all undiscovered before me. "
Isaac Newton

"On fait la science avec des faits,
comme on fait une maison avec des pierres;
mais une accumulation de faits n'est pas plus une science
qu'un tas de pierres n'est une maison."
La Science et l'Hypothèse, Henry Poincaré

Contents

Introduction

For a long time since the origin of the humankind, people studied the Universe relying on the observations of the sky in the visible light: only in the XIX Century, the discovery of the ultra-violet and infra-red light from Johann Ritter and Wilhelm Herschel, together with the detection of radio waves by Heinrich Hertz, definitely showed that the light spectrum extends to lower and higher energies outside the human visibility region. In this way **Multi-wavelength** astronomy was born. An example of our Galaxy in different wavelengths of the electromagnetic spectrum can be seen in Figure 1.

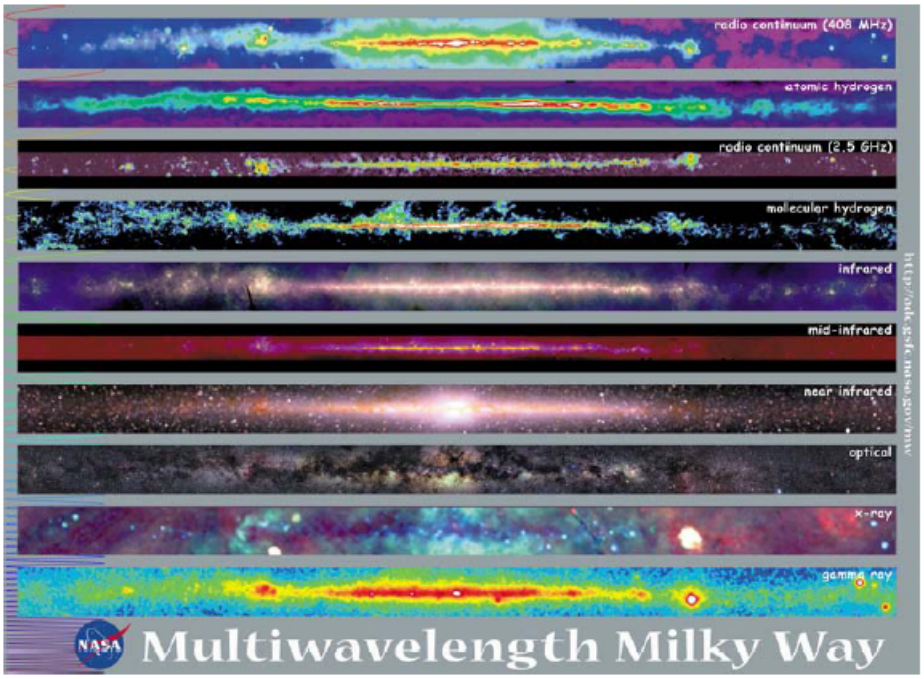

Figure 1. This picture represents the Milky Way as seen in different wavelengths: it is built up collecting results from several observations, obtained with different experimental techniques. (Figure from [70]).

Meanwhile, investigations concerning the particles flux coming from the Universe, the so-called Cosmic Rays (CRs), discovered by Victor Hess in 1912, showed that the radiation from space not only extends to a much larger energy range than previously thought (see CR energy spectrum in Figure 1.9), but also comprises various components. Indeed, when a high-energy cosmic ray interacts with an atmosphere nucleus, it produces many particles: these themselves collide with other nulcei, producing a "cascade" of particles that is called Extensive Air Shower (EAS). The main components of this atmospheric shower are the hadronic component (mainly mesons, like K and π), the electromagnetic component (photons and $e^{\pm}$ pairs) and the muonic component (μ). **Multi-messenger** astronomy therefore began to

develop.
Nowadays, astronomy exploits the entire electromagnetic wavelengths range, from low-energy radio waves, optical and X-rays up to high-energy gamma-ray photons. At the same time, attempts are made to identify the different cosmic ray components and to probe the Universe in the light of other astrophysical messengers, such as gravitational waves or neutrinos.
We are experiencing the beginning of a new field of research: multi-messenger astronomy is the only way to access as high energies as the one reached by cosmic accelerators; at present, the highest energy particles accelerator is the Large Hadron Collider (LHC) at CERN (see Figure 3 and [63]), designed for proton-proton collisions at an energy in the centre of mass of 13 TeV. LHC represents the frontier in the field of particles accelerators and, considering the current technological skills and knowledge, LHC limits seem to be very hard to overcome.

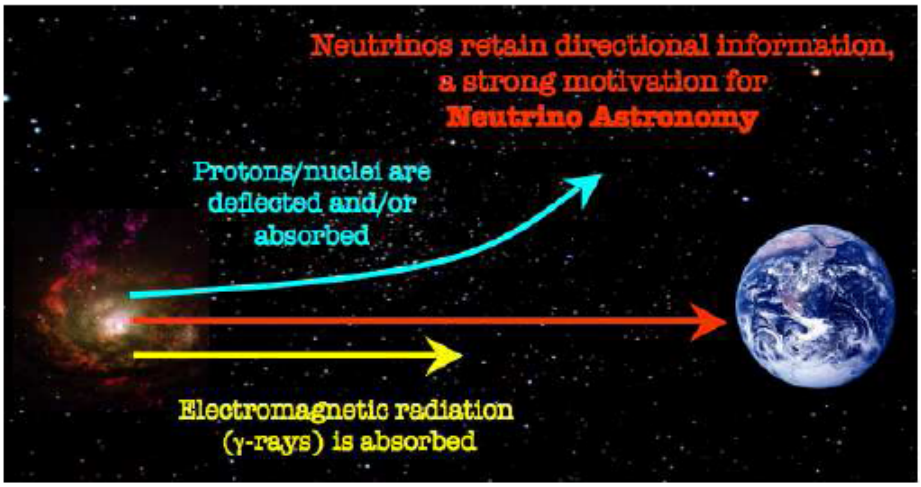

Figure 2. The picture points out the main motivation for looking at neutrinos in the frame of multi-messenger astronomy. On the left side, a far away cosmic accelerator is depicted, assumed as source of cosmic messengers, as charged particles, photons and neutrinos. Photons are affected by electromagnetic interaction and may be absorbed during their propagation. Effects of electromagnetic interaction on charged particles (protons and nuclei) produce particles absorption and deflection by magnetic fields, causing the loss of pointing properties. On the contrary, neutrinos are weakly interacting and therefore they can travel unperturbed through the low density interstellar medium, able to reach the Earth, where they eventually may be detected, preserving directional information on the cosmic source. (Figure from [37]).

The multi-messenger approach is a complementary source of information for the classical photon-astronomy: the case of neutrinos is of particular interest. Since neutrinos carry no charge, they are not perturbed by magnetic fields and point directly back to their site of emission: this allows to make a point source analysis through neutrino messenger, in the same way that has always been done through photons. Furthermore, neutrinos can escape the innermost dense regions of astrophysical objects long before they become optically thin and release photons: this allows to probe the inner regions of astrophysical sources, where the physics is highly dominated by general relativity. The motivations for neutrino astronomy are depicted in Figure 2. In contrast to electromagnetic emission and cosmic rays, the detection of neutrinos alone could unambiguously prove the acceleration of hadronic particles in an astrophysical process. Thus the observation of high-energy neutrinos could bring the only conclusive identification of sources of the most energetic cosmic rays.
In addition, cosmic neutrinos of the highest energies are of particular interest since the photon range above a certain energy is significantly reduced due to the interaction with the low energy Cosmic Microwave Background (CMB): the result of this interactions is a pair

Figure 3. The LHC experiment at CERN.

production. So, photons of energy higher than a PeV are stopped: in this way they can only travel as far as the nearest active galaxy, which significantly limits the possibilities for astronomy at the highest energies (see [60]). Neutrinos of the same and higher energy, on the other hand, do not suffer from these interactions, in fact they can travel over cosmological distances without being deflected.

The first compelling evidence for a neutrino signal from space was found in 1987, when more than twenty neutrinos of $\simeq$ MeV energies were detected in several instruments in coincidence with supernova SN1987 (see [14], [28] and [56]), as shown in Figure 4.

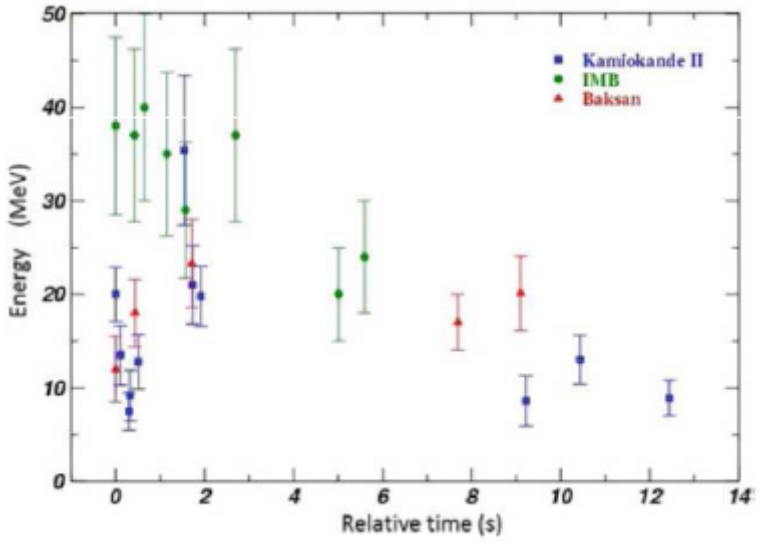

Figure 4. Detected neutrino signals in coincidence with SN1987 from Kamiokande II, IMB and Baksan.

This discovery demonstrated that it is feasible in principle, even if highly challenging, to detect cosmic neutrinos. There are numerous motivations to carry on this search, in particular the request of finally identifying the sources of the most energetic cosmic rays and understand their internal dynamic. Indeed, the production of high-energy neutrinos has been proposed to occur in several kinds of astrophysical sources, where hadrons may be accelerated, such as

Active Galactic Nuclei (AGN), Gamma-Ray Bursts (GRBs), Supernova Remnants (SNRs) and microquasars. Many of these astrophysical accelerator show transient behaviour: variations in the energy output of these powerful astrophysical objects cover a large range in the time domain, from seconds for GRBs (see [86]) to weeks for AGN.
The detection of astrophysical sources through messengers is very difficult, due to a small number of expected events and a large background contamination. A way to overpass this difficulty is to combine the detection of non electromagnetic messengers with the electromagnetic signal, to provide a multi-messenger dataset: the present thesis work is an attempt made in this context, that is the search for neutrinos emissions from GRBs in coincidence with the gamma emission.

There are currently two operating large-volume neutrino telescope in the world: the Northern hemisphere ANTARES (Astronomy with a Neutrino Telescope and Abyss environmental RESearch), located in the Mediterranean Sea, and the Southern hemisphere IceCube telescope, located in the South Pole ice. These telescopes are designed to search for high-energy cosmic neutrinos (>100 GeV) generated in extreme astrophysical sources. Each detector is able to monitor with a high duty cycle a full hemisphere of the sky, if we just consider up-going events, that is events coming from below the detector's horizon (that traversed the whole Earth before reaching the detector), for which the research is optimised in order to reduce the huge background of events. These two experiments are complementary: since they are located in different hemispheres, their visibility allows to cover the full sky. Most importantly, ANTARES can see the Galactic Centre, to monitor the activity of the huge black hole ($\sim 4 \times 10^6 M_\odot$, where $M_\odot$ indicates a solar mass) at the centre of our Galaxy. In Figure 5 the ANTARES and IceCube visibilities are shown.
The recent IceCube 5.7σ discovery of extraterrestrial high-energy neutrinos (see [2] and [3]) opened new windows in the field of astroparticle physics. This result has fixed the scale of neutrino fluxes in the Universe and has inspired a large number of hypotheses for their origin, mainly due to the poor localisation of the events: the 37 cosmic neutrino events are reported in the map of Figure 6, while in Figure 7 it is shown how the measurements differ from the expected background. In particular, there are hints of a small excess of down-going events, possibly indicating the presence of a Galactic component or an enhancement from the Southern sky (see [83]).

Searches for transient astrophysical phenomena offer very promising opportunities for high-energy neutrino telescopes, because the relative short duration of the events means that the level of background contamination is strongly reduced. Targeted searches performed offline by the ANTARES telescope on GRBs, AGN flares and microquasar outbursts have so-far yielded limits on the neutrino production in these sources. Moreover, taking full advantage of the possibilities offered by multi-messenger searches for transient sources, a multi-wavelength follow-up program, denoted as TAToO (Telescopes-ANTARES Target of Opportunity), has operated within the ANTARES Collaboration since 2009. The network was composed of two small robotic optical telescopes, TAROT and ROTSE, and of the *Swift* X-ray telescope (XRT). In 2013, ROTSE has been dismissed. The scientific program is based on optical and X-ray follow-ups of selected high-energy events, very shortly after their detection (see [12]) up to two months later.

This thesis has been developed in the context of the ANTARES Collaboration: it concerns one of the ever most intense transient source of the gamma sky, GRB130427A, in particular the search for a neutrino coincidence in the ANTARES data, since this source was below ANTARES horizon at the trigger time.
In Chapter 1 the sources of our interest (GRBs) will be sound out, together with the photo-

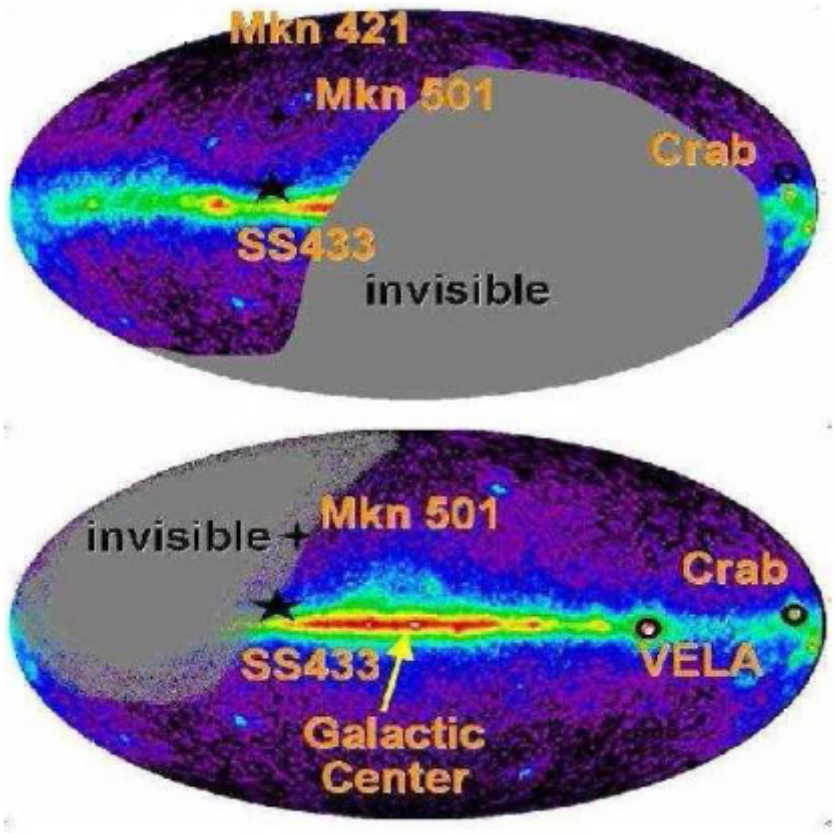

Figure 5. Field of view of a neutrino telescope at the South Pole (top panel) and in the Mediterranean Sea (bottom panel), in galactic coordinates. Invisible regions in the sky represent the direction of down-going events. Some candidate neutrino sources are indicated in the map. It is clear that, on the contrary of the South Pole telescope, a Mediterranean observatory would have access to the Galactic centre, that is a very promising object of investigation.

hadronic model that predicts neutrinos production. Then, in Chapter 2 neutrino physics will be introduced and the detection technique on which a neutrino telescope is based will be illustrated, with a deep overview on the ANTARES detector. In Chapter 3 the analysis leading to the burst's identification will be described, in Chapter 4 the burst analysis will be illustrated and in Chapter 5 results of a Time-Resolved analysis on the burst and of a serendipitous search will be presented. Finally, in Chapter 6 the next generation of neutrino telescope, KM3NeT, will be introduced and in Chapter 7 conclusions will be discussed.

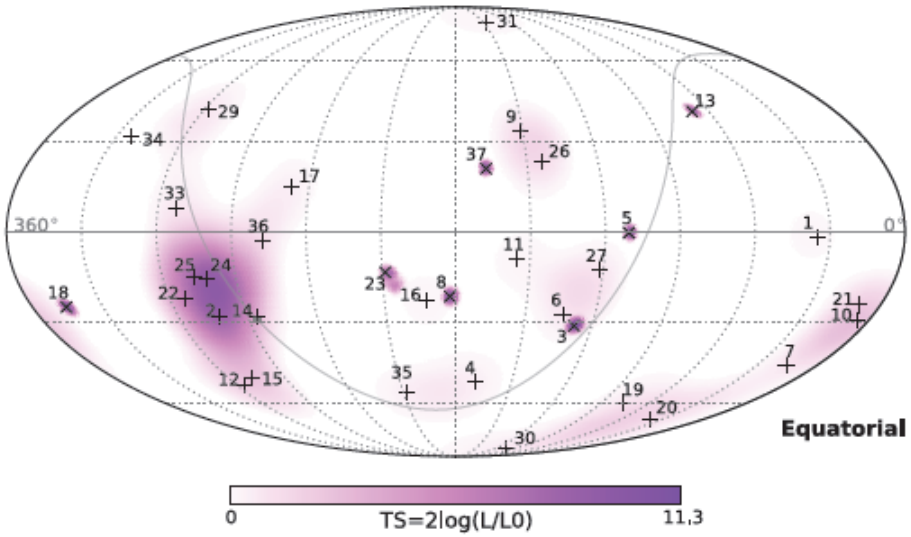

Figure 6. Sky map in equatorial coordinates RA and DEC of the first significant evidence for a cosmic neutrino signal in the IceCube data from the years 2010 to 2013. Cascade-like event signatures are marked with +, muon events are marked with x. The probability for a point source at each of the locations is color-coded, through the values of a Test Statistic (TS). No indication for significant clustering could be found. (Figure from [3]).

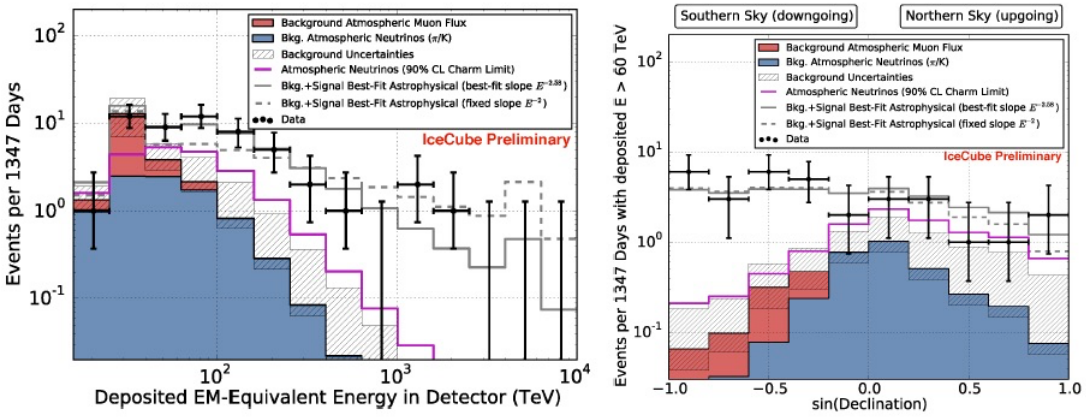

Figure 7. On the left side, the number of detected neutrino events as a function of the energy deposited: data are in black, atmospheric muons are in red, atmospheric neutrinos are in blue, background uncertainties are in gray dashed, a fit to the data with fixed spectral slope equal to 2 is in gray solid line, another fit to the data giving a best-fit spectral slope equal to 2.38 is in gray dotted line: it is evident the excess for energies higher than PeV (1 PeV = 10^3 TeV =10^{15} eV). On the right side, the same legend is for number of detected neutrino events as a function of the direction: the excess is associated with down-going events.

Chapter 1

Gamma-Ray Bursts

Gamma-Ray Bursts are time-limited and intense pulses of soft γ-rays. The bursts last from a fraction of a second to several hundred seconds. GRBs come from cosmological distances, so that they appear to be randomly distributed in the sky. The overall observed fluences range from 10^{-3} erg/cm^2 to 10^{-7} erg/cm^2 (the lower limit depends, of course, on the characteristics of the detectors measuring them and not on the bursts themselves). This corresponds to isotropic luminosity of 10^{51}-10^{54} erg/s, making GRBs the most luminous objects in the sky. However, because most GRBs are narrowly beamed, the corresponding energies are "only" around 10^{51} erg, making them comparable to supernovae in the total energy release.
GRBs are generally followed by **afterglows**, lower energy, long lasting emissions in the X-ray, optical and radio wavelengths. In some cases the radio afterglow has been observed several years after the bursts. Afterglow allows spectroscopy to be performed and the burst's position to be accurately determined: this enables the identification of host galaxies in almost all cases and the determination of the corresponding redshift, that ranges up to z$\sim$10.
Even if not all observed features are understood, there is an overall agreement between the observations and the **fireball model**. According to the fireball model GRBs are produced when the kinetic energy of an ultra-relativistic flow is dissipated: the GRB is created by internal dissipation within the flow, while the afterglow via external shocks with the circumburst medium. In this thesis I will focus on the internal-external shock fireball model.
Numerous observations of GRBs and of afterglows allow to constrain the fireball model and to describe the emitting region: the evidence on the nature of the inner engine that powers the GRB and produces the ultra-relativistic flow is, however, indirect. The energetic requirements and the time scales suggest that a GRB involve the formation of a black hole via a catastrophic stellar collapse event or possibly a neutron star merger. Additional indirect evidence arises from the requirement that the fireball model also describes the long (several dozen seconds) activity of the inner engine: this hints towards an inner engine built on an accreting black hole. On the other hand, the evidence of association of GRBs with star forming regions indicates that GRBs progenitors are massive stars. Finally, the appearance of supernova bumps in some afterglow light curves suggests a stronger association with stellar collapse.

In this chapter I will review the theory of GRB, focusing as mentioned earlier on the fireball internal-external shock model. I will begin in Section 1.1 with a brief presentation of the discovery of GRBs and of their observational properties. In Section 1.2 I will turn to analyse some generally accepted ingredients of the fireball model, such as the essential ultra-relativistic nature of this phenomenon as well as the synchrotron emission and particle acceleration in relativistic shocks. Then, the dichotomy between a spherical and a jet-like geometry is presented in Section 1.3, followed by an examination of different "inner engines" and of various aspects related to their activity in Section 1.4. Moreover, a review of the mod-

els describing the photon prompt emission of GRBs and other related emissions, especially high energy neutrinos, but also Ultra High Energy Cosmic Rays (UHECRs) and gravitational radiation, is given through Sections 1.5, 1.6 and 1.7.

1.1 A brief history of the discovery of Cosmic Gamma-Ray Bursts

In October 1963, the US Air Force launched the first in a series of satellites inspired by the recently signed Nuclear Test Ban Treaty. Signatories of this treaty agreed not to test nuclear devices in the atmosphere or in space. The *Vela* (from the Spanish verb *velar*, to watch) series satellites were part of an unclassified research and development program whose goal was to monitor nuclear tests from space and give the US a mean of verifying the conditions of the treaty. Each satellite operated in pair with an identical satellite on the opposite side of a circular orbit 250000 km in diameter so that no part of the Earth was shielded from direct observation. The *Vela* satellites carried X-ray, γ-ray and neutron detectors as instrumentation. The X-ray detectors were intended to directly sense the flash of X-rays from a nuclear blast. Although most of the energy of a bomb blast in space would have been directly visible as an X-ray flash, a simultaneous indication by the γ-ray detectors would have provided a confirming signature of the nuclear event. A further confirmation would come from the detection of neutrons. The *Vela* designers were also aware that detonating a nuclear bomb behind a thick shield or on the dark side of the Moon would have effectively hidden the initial flash of X-rays from the satellites' view. Hence the γ-ray detectors could also look for hard γ-radiation resulting from the cloud of radioactive material blown out after the nuclear blast: this blast cloud could not have been totally shielded from view and would have expanded rapidly. It would easily have been detected in γ-rays even if the detonation had taken place behind the Moon, out of direct view of the satellites' X-ray detectors.
The *Vela* satellites generally performed well and greatly exceeded their expected operational lifetimes. The satellites' capabilities were steadily improved with each launch. In particular, *Vela* 5a and 5b (launched in 1969) and *Vela* 6a and 6b had sufficient timing accuracy that they could reasonably determine directions to the triggered events. For these later satellites, the light travel time from one spacecraft to another, across the orbital diameter (around 1 second), was greater than the resolution time of the event's onset (about 0.2 seconds). The event angle with respect to the line between a pair of satellites could thus be determined based on the difference in trigger times for the two satellites. Direction angles for a single event observed by multiple pairs of satellites could then be combined to determine the possible direction for the source of the event.
In 1972, thanks to the timing accuracy of the later *Vela* satellites, Ray Klebesadel, Ian Strong and Roy Olsen of Los Alamos Scientific Laboratories were able to deduce the directions of the events with sufficient accuracy to rule out the Sun and Earth as sources. They concluded that the γ-ray events were "of cosmic origin". In 1973, this discovery was announced in Ap.J. letters. Their paper discusses 16 cosmic gamma-ray bursts observed by *Vela* 5a, 5b, 6a and 6b between July 1969 and July 1972.
Using a hard X-ray detector on board *IMP-6* intended to study solar flares, Tom Cline and Upendra Desai of NASA/GSFC were the first to confirm this finding and provide some spectral information that showed that the burst spectra peaked at γ-ray energies. Thus the events were not simply the high energy tail of an X-ray phenomenon. A collimated γ-ray telescope on board *OSO-7* was also able to confirm the direction of one of the events, supporting the original conclusions of cosmic origin. These confirming results, published close on the heels of the original discovery, gave the whole scenario an aura of enhanced mystery. The excitement created in the astronomical community was evidenced by a burst of publications of instrumental and theoretical papers on the newly discovered "cosmic gamma-ray bursts". For more

information on GRBs discovery see [71].

The first significant step in understanding GRBs was the launch in 1991 of the *Compton Gamma-Ray Observatory* (CGRO). The all-sky survey from the BATSE instrument showed that bursts were isotropically distributed, strongly suggesting a cosmological origin with essentially zero dipole and quadrupole components, as can be seen in Figure 1.1.

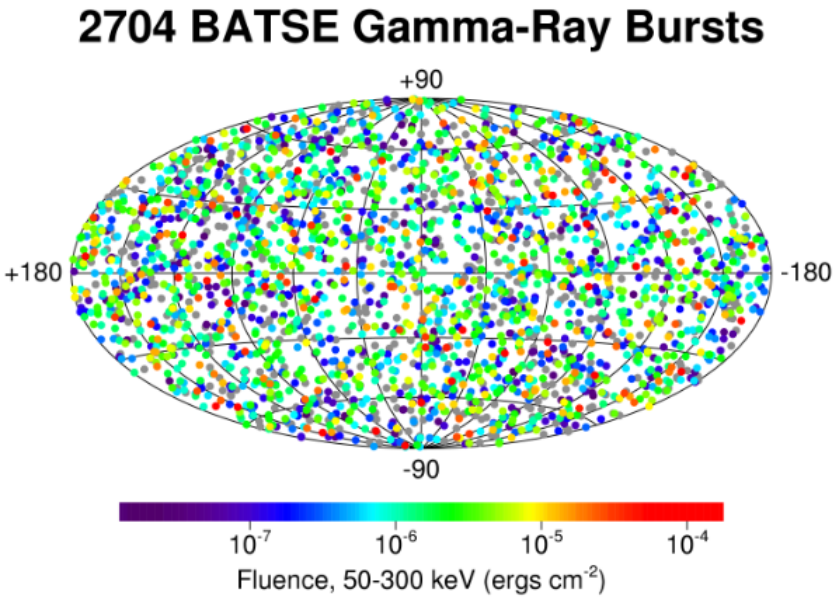

Figure 1.1. The distribution of 2704 bursts detected by BATSE between 1991 and 2000 in galactic coordinates. The uniformity of the distribution strongly points toward an extragalactic origin of the bursts. (Figure from [24]).

The next major developments came after 1997, when the Italian-Dutch satellite *Beppo-SAX* succeeded in detecting fading X-ray images which, after a delay of 4-6 hours for processing, led to positions, allowing follow-ups at optical and other wavelengths. This paved the way for the measurement of redshift distances, the identification of candidate host galaxies and the confirmation that GRBs were indeed at cosmological distances. A consolidation of the progress made by *Beppo-SAX* was possible through the *HETE-2* satellite, after the demise of CGRO and *Beppo-SAX*.
The third wave of significant advances in the field is due to the *Swift* multi-wavelength satellite, launched in 2004 and still operative, which achieved the long-awaited goal of accurately localized afterglows starting a minute or so after the burst trigger, at γ-ray, X-ray and optical wavelengths, thanks to its three instruments: the Burst Alert Telescope (BAT), the X-Ray Telescope (XRT) and the Ultra-Violet Optic Telescope (UVOT).
Finally, of particular interest is the *Fermi* satellite: launched in 2008 and still operative, it has on-board two instruments sensitive up to high-energy γ-rays. Covering basically the entire sky (except the part occulted by the Earth), the Gamma-ray Burst Monitor (GBM) detects around 300 GRBs per year and provides spectroscopic information of the γ-ray emission in unprecedented detail. Together with the Large Area Telescope (LAT), energies over seven orders of magnitude are covered from $\sim$ keV up to and exceeding 300 GeV.

1.2 GRB fireball model

The energy involved in GRB explosions is huge. No matter in which form the energy is initially injected, a quasi-thermal equilibrium (at relativistic temperatures) between matter and radiation is reached, with the formation of electron-positron pairs accelerated to relativistic speeds by the high internal pressure. This is a fireball (see [35]). When the temperature of the radiation (as measured in the comoving frame) drops below ~ 50 keV, the pairs annihilate faster than the rate at which they are produced. But the presence of even a small amount of barions, corresponding to only $\sim 10^{-6}$ $M_\odot$, makes the fireball opaque to Thomson scattering: the internal radiation thus continues to accelerate the fireball until most of its initial energy has been converted into bulk motion. After this phase the fireball expands at a constant speed and at some point becomes transparent, so that radiation can escape. In Figure 1.2 a schematic picture of the internal-external shock fireball model is represented.

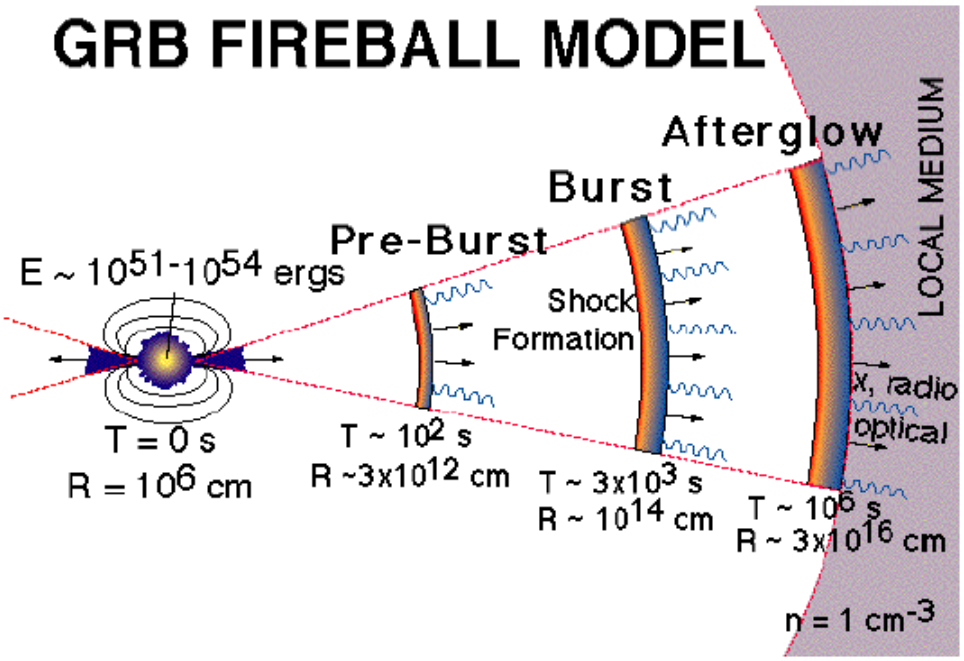

Figure 1.2. A schematic picture of the fireball model. (Figure from [49]).

The compactness problem

Even before the discovery that GRBs are at cosmological distances, researchers were puzzled about such rapidly variable and strong high energy fluxes. In fact, even if bursts were close by (in the Galactic halo, for example), they would be highly super-Eddington and this poses the problem to explain how high energy γ-rays can survive against the $\gamma\gamma \longrightarrow e^+e^-$ process. In fact, from the minimum variability time scale (time needed to double or halve the flux) we can estimate, by a causality argument, the size R of the emitting region. Therefore we can form the luminosity to size ratio L/R which controls the processes involving photons and in particular the $\gamma\gamma \longrightarrow e^+e^-$ process (in fact its optical depth $\tau_{\gamma\gamma} \propto R(L/R^2) \propto L/R$). Now, the L/R ratio is too large (and therefore GRBs are too compact) to let any photon above threshold for pair production to survive. For more details see [75].

Relativistic motion

If the source is moving relativistically toward the observer, then the observed photon energies are blue-shifted and the typical angles (as observed in the laboratory frame) between pho-

tons are smaller, decreasing the probability for them to interact. This solves the compactness problem. Bulk Lorentz factors $\Gamma > 100$ are required to avoid strong suppression of high energy γ-rays due to photon-photon collisions.
There is however a second argument demanding for strong relativistic motion, concerning the very fast observed variability. In fact the size associated with one millisecond is R $\sim 3 \times 10^7$ cm, which is much too small to be optically thin. To match the observed time-scales with the size at which the fireball becomes transparent ($R_t \sim 10^{13}$ cm) we need a Doppler contraction of time given approximately by $ct_{var} \sim R_t(1-\beta)$, yielding $\Gamma \simeq 400$.

1.2.1 The internal/external shock scenario

If the central engine does not produce a single pulse, but works intermittently, it can produce many shells (i.e. many fireballs) with slightly different Lorentz factors. Late but faster shells can catch up early slower ones, producing shocks which give rise to the observed burst emission. In the meantime, all shells interact with the interstellar medium and at some point the amount of swept up matter is large enough to decelerate the fireball and produce other radiation which can be identified with the afterglow emission observed at all frequencies.
This is currently the most accepted picture for the burst and afterglow emission: according to this scenario, the burst emission is due to collisions of pairs of relativistic shells (internal shocks), while the afterglow is generated by the collisionless shocks produced by shells interacting with the interstellar medium (external shocks). All the radiation we see is believed to come from the transformation of ordered kinetic energy of the fireball into random energy. For internal shocks, this must happen at some distance from the explosion site, to allow the shells to be transparent to the produced radiation ($R_t \sim 10^{13}$ cm). For external shocks, the deceleration radius, where the fireball starts to emit the afterglow, depends on the density of the interstellar medium (and by the possible presence of a stellar wind), by the energy of the fireball and its bulk Lorentz factor. For densities of the order of 1-10 proton/cm^3, we get R $\sim 10^{16}$ cm as a typical value for the start of the afterglow.

1.2.2 Radiation mechanisms

It is reasonable to assume that internal and external shocks can amplify seed magnetic fields and accelerate electrons to relativistic energies. These are the basic ingredients for the synchrotron process, which is therefore a strong candidate for the origin of the observed radiation of both the prompt and the afterglow emission. In the case of the prompt emission, photons are then taken to higher energy thanks to Inverse Compton: indeed, in the internal shock scenario we have collisions of pairs of shells which are both relativistic, with bulk Lorentz factors Γ_1 and Γ_2. After the collision, the merged shell is still relativistic, with a bulk Lorentz factor which is between Γ_1 and Γ_2. The energy which is liberated in the process is therefore a small fraction of the initial one, unless the ratio Γ_1/Γ_2 is huge. If the Lorentz factors of the shells are distributed in a large interval, then a very fast shell moving in the photon field created by previous collisions would scatter these ambient photons and would produce very high energy γ-rays through the Inverse Compton process. The different energy ranges reached with synchrotron and Inverse Compton mechanisms are shown in Figure 1.3.

1.3 Spheres versus jets

A hot issue in the GRB field is the possible collimation of the emitting plasma, leading to anisotropic emission able to relax the power requirements, at the expense of an increased burst event rate. In this respect polarization studies could be crucial, since there can be a

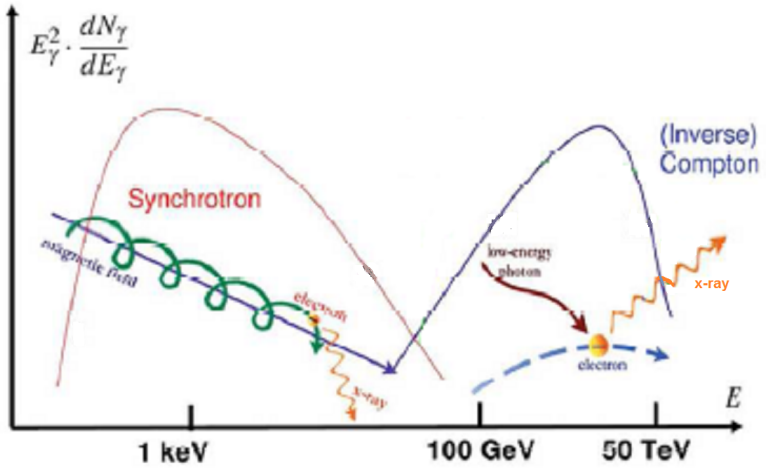

Figure 1.3. Synchrotron and Inverse Compton energy spectrum.

link between the deceleration of a collimated fireball, the time behavior of the polarized flux and its position angle, and the light curve of the total flux.

An argument in favour of the collimation comes from the breaks seen in light curves: assume that the burst is collimated within a cone of semi-aperture θ. Assume also that, initially, the bulk Lorentz factor of the fireball is such that $1/\Gamma < \theta$. In this case, because of relativistic beaming, the observer (which is within the cone defined by θ) will receive light only from a section of the emitting surface, of aperture $1/\Gamma$ and radius R/Γ, where R is the distance from the apex of the cone. This is illustrated in Figure 1.4. Initially, this area increases both because R increases with time and because Γ decreases. This leads to the estimate of how the received flux varies in time. If the fireball is spherical, this will continue as long as the motion is relativistic. But if the fireball is collimated, there is a time when $1/\Gamma$ becomes comparable to θ. After this time the observed area will increase only because R increases while the decrease in Γ will not "enlarge" the available surface (we are ignoring here the complications due to side expansion, which does not change qualitatively the argument). Since the rate of increase of the observed emitting area changes, then there will be a change in the slope of the light curve. An achromatic break is predicted.
An argument against strong collimations comes from Iron lines: the presence of sometimes broad iron lines in the X-ray afterglow of some bursts imply that a dense, possibly iron-rich material must be present in the vicinity of the burst site. The large densities involved suggest that the line emission process is fast photo-ionization and recombination by an optically thick slab, reprocessing the ionizing continuum in its $\tau \sim 1$ layer (where τ is the relevant optical depth). The observed line flux would then be proportional to the projected emitting area, which becomes very small if the burst and afterglow fluxes are collimated in a cone as narrow as 2°. Nowadays, this argument is still controversial and some more studies are needed.

1.4 Progenitor candidates

The fireball model tells us how GRBs operate. However, it does not answer the most interesting astrophysical question: what produces them? Which astrophysical process generates the energetic ultra-relativistic flows needed for the fireball model? Several observational clues help us answer these questions.

- **Energy**: The total energy involved is as large as $\sim 10^{54}$ erg, a significant fraction of the

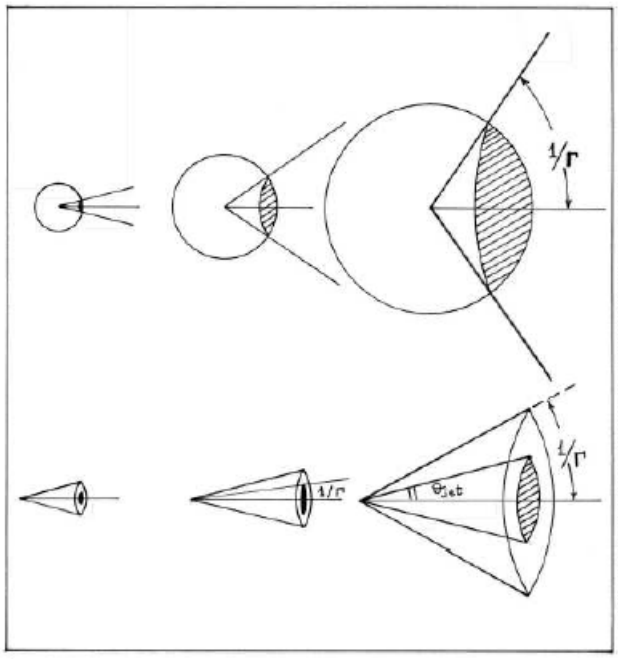

Figure 1.4. Spheres or jets? This figure tries to explain a possible way to discriminate between the two possibilities. During the initial phases of the afterglow, the bulk Lorentz factor is large, and consequently the observer sees only the fraction of the emitting area inside a cone with aperture angle $\sim 1/\Gamma$. There is no difference between a sphere and a jet during this phase. In the spherical case the emitting area continues to increase both because the radius of the sphere increases and because Γ decreases, allowing more surface to be within the $1/\Gamma$ cone. In the case of collimation in a jet, once $1/\Gamma$ becomes comparable to the jet opening angle θ, the observed surface increases only because the distance to the jet apex increases. The light curve predicted in the two cases is therefore the same at early times, but in the jet case there will be a break at a particular time (when $1/\Gamma \sim \theta$), after which the light curve decreases more rapidly than in the spherical case. (Figure from [49]).

binding energy of a stellar compact object. The inner engine must be able to generate this energy and accelerate $\sim 10^{-5} M_\odot$ to relativistic velocities.

- **Collimation**: Most GRBs are collimated with typical opening angles $1^\circ < \theta < 20^\circ$. The inner engine must be able to collimate the relativistic flow.

- **Long and Short Bursts**: The bursts are divided in two groups, according to their overall duration T: long bursts with T > 2 seconds and short ones with T < 2 seconds. As the duration is determined by the inner engine, this may imply that there are two different inner engines.

- **Time Scales**: The variability time scale, $t_{\rm var}$, is as short as the ms time-scale. The overall duration of long GRBs is of the order of 50 seconds. According to the internal shocks model these time scales are determined by the activity of the inner engine. $t_{\rm var} \sim$ 1 ms suggests a compact object. T ~ 50 s is much longer than the dynamical time scale, suggesting a prolonged activity. This requires two different time scales operating within the inner engine, ruling out any "explosive" model that release the energy in a single explosion.

These clues, most specifically the last one, suggest that GRBs arise due to accretion of a massive ($\sim 0.1 M_\odot$) disk onto a compact object, most likely a newborn black hole. A compact object is required because of the short time scales. Accretion is needed to produce the two different time scales and in particular the prolonged activity. A massive ($\sim 0.1 M_\odot$) disk

is required because of the energetics. Such a massive disk can form only simultaneously with the formation of the compact object. This leads to the conclusions that GRBs accompany the formation of black holes.
For the class of long GRB the candidates are massive stars whose core collapses to a black hole (BH), either directly or after a brief accretion episode, possibly in the course of merging with a companion: the initial system consists of a neutron star (NS) and a FeCO star, the final one is either a NS-NS system or a NS-BH. This scenario is referred to as the collapsar or hypernova scenario, which received strong support through the secure spectroscopic detection in some cases of an associated supernova event.
For short bursts the most widely speculated candidates are neutron star binaries: the two NSs lose orbital angular momentum by gravitational wave radiation and undergo a merger. The final state can be either a single NS, if the initial mass of the system is not enough to overcome the critical mass to produce a BH, or a BH.
A detailed scheme of all possible scenarios is shown in Figure 1.5, while an artistic representation of these situations is shown in Figure 1.6.

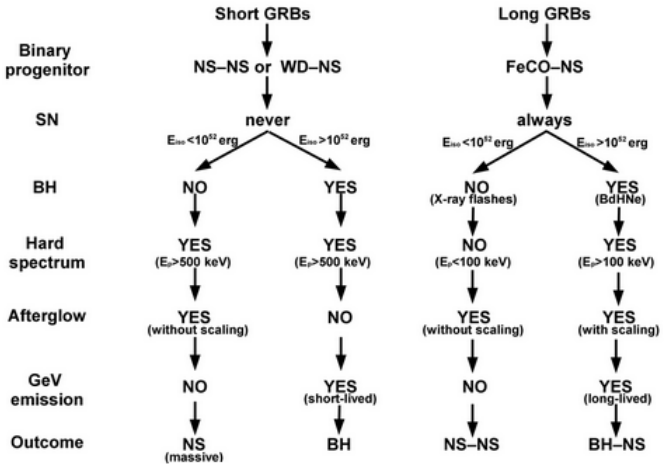

Figure 1.5. This scheme describes both long and short GRBs as a result of a binary process: it also shows the possible kind of emissions and outcomes from each family.

Both of these progenitor types are expected to have as an end result the formation of a few solar mass black hole, surrounded by a temporary debris torus whose accretion can provide a sudden release of gravitational energy, sufficient to power a burst. An important point is that the overall energetics from these various progenitors do not differ by more than about one order of magnitude. The duration of the burst in this model is related to the fall-back time of matter to form an accretion torus around the BH. For further details see [68].
A tangible proof of such a catastrophic origin comes from the optical afterglow light curve of the bursts: for some long GRBs a so-called red supernova (SN) bump has been identified; for example, in GRB041006, it is shown in Figure 1.7.

This can be taken as a clear signature of a GRB-SN association. In particular, all the cases up to now involved Ib or Ic SN type, that is core collapse supernovae: they are massive stars ($4M_\odot < M < 20-30M_\odot$), for which nuclear processes are able to burn elements heavier than carbon and oxygen, so that exothermic nuclear reactions can proceed all the way from H to ^{56}Fe, which is the most stable element in nature; indeed, no element heavier than ^{56}Fe can be generated by fusion of lighter elements through exothermic reactions. It should be noted that while iron is formed in the core, neutrinos are produced through the reaction

$$^{56}Ni \longrightarrow {}^{56}Fe + 2e^+ + 2\nu_e$$

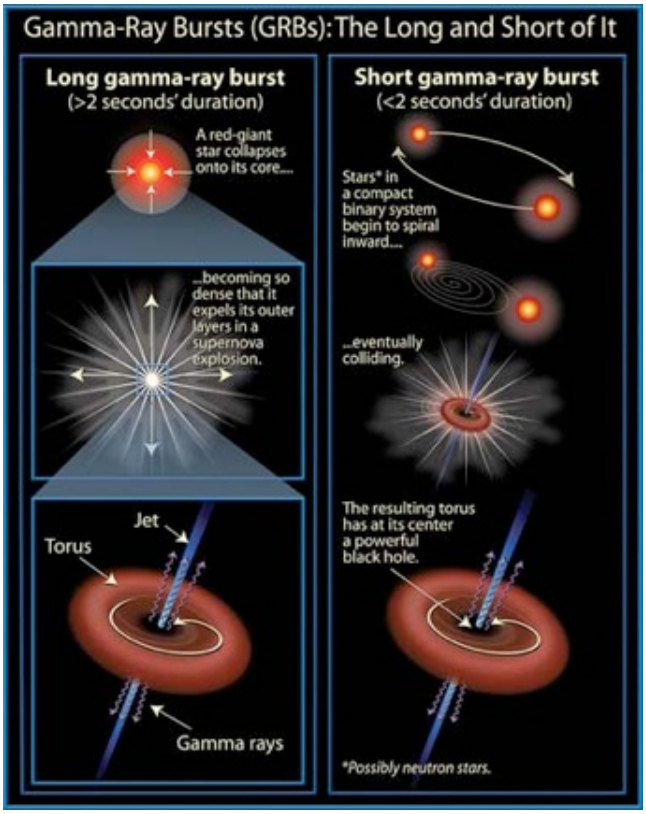

Figure 1.6. This graphic illustrates the different sources and processes that result in long and short GRBs. The left panel shows the collapse of a giant star that is thought to lead to a long GRB. The right panel shows the in-spiral and coalescence of two neutron stars, which is thought to result in a short GRB. (Credit: NASA).

In addition, as the core density increases, the inverse β-decay process, through which electrons are captured by protons forming neutrons and neutrinos

$$e^- + p \longrightarrow n + \nu_e$$

becomes efficient and nuclei richer of neutrons than ^{56}Fe can form, like ^{118}Kr. Since neutrinos interact with matter very weakly, they diffuse from the core to the surface and leave the star, subtracting energy from the core. At the same time, the iron photo-disintegration process

$$\gamma + {}^{56}Fe \longrightarrow 13^4He + 4n$$

which is an endothermic process, subtracts further energy to the core. Thus, all these processes tend to destabilize the stellar core, so that when the core mass becomes bigger than the Chandrasekhar limit, the internal pressure gradient becomes smaller than the gravitational attraction and the core collapses reaching, in a fraction of a second, densities typical of atomic nuclei, $\sim 10^{14}$ g/cm^3. The core is now composed mainly of neutrons and reacts to a further compression producing a violent shock wave that ejects, in a spectacular explosion, most of the material external to the core in the outer space. This phenomenon is called supernova explosion: the luminosity of the star suddenly increases to values of the order of $\sim 10^9 L_\odot$, where $L_\odot \sim 10^{33}$ erg/s is the Sun luminosity, and it is in this phase that elements heavier than ^{56}Fe are created. The remnant of this explosion is a nebula, in the middle of which sits what remains of the core, i.e. a neutron star. For further details about stellar evolution, see [46].
As also Figure 1.7 shows, the GRB trigger is generally recorded previously than the SN spectrum.

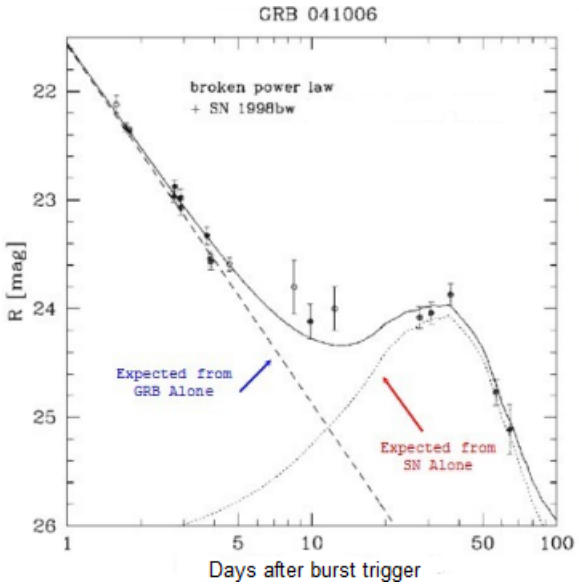

Figure 1.7. The SN bump in the light curve of GRB041006.

1.5 Fermi acceleration in GRBs: UHECRs from GRB fireball

It has been shown in Section 1.2.2 that the expected spectrum is not thermal. It is in the form of a power law: actually, the GRBs spectra are fitted through a series of observational relations:

1. Power law (PL):
$$\frac{dN}{dE} \propto E^{\alpha} \tag{1.1}$$

2. Smoothly broken power law (SBPL):
$$\frac{dN}{dE} \propto \begin{cases} E^{\alpha} & E < E_{\gamma} \\ E^{\beta} & E \geq E_{\gamma} \end{cases} \tag{1.2}$$

3. Cut-off power law (CPL):
$$\frac{dN}{dE} \propto E^{\alpha} e^{-E/E_{\gamma}} \tag{1.3}$$

4. Band:
$$\frac{dN}{dE} \propto \begin{cases} E^{\alpha} e^{-E/E_{\gamma}} & E < (\alpha - \beta)E_{\gamma} \\ E^{\beta} & E \geq (\alpha - \beta)E_{\gamma} \end{cases} \tag{1.4}$$

where the last function has been properly defined for GRBs spectra.
The power law functional form is clearly associated with the acceleration mechanism, known as *I order Fermi mechanism* or *shock acceleration*: this process takes place when a blast wave, produced during an extremely energetic astrophysical event, propagates in a space region where some plasma is present. It is deeply described in [45]. The clearest example of such a situation is when a shock wave propagates through the interstellar medium ahead of the supersonic shell of a supernova remnant. A flux of high energy particles is assumed to be present both in front of and behind the shock front. The particles are assumed to be propagating at speeds close to that of light and so the velocity of the shock is very much less than those of the high energy particles. The high energy particles scarcely notice the shock at all since its thickness is normally very much smaller than their gyroradius. Because of scattering by streaming instabilities or turbulent motions on either side of the shock wave,

when particles pass though the shock in either direction, they are scattered so that their velocity distribution rapidly becomes isotropic in the frame of reference of the moving fluid on either side of the shock. Figure 1.8 illustrates the situation in the laboratory frame, that is the interstellar medium where the wave propagates at velocity V_s. Matter velocity u behind the wave is related to the wave velocity by hydrodynamic's laws: if the wave is supersonic, then

$$u = \frac{3}{4} V_s$$

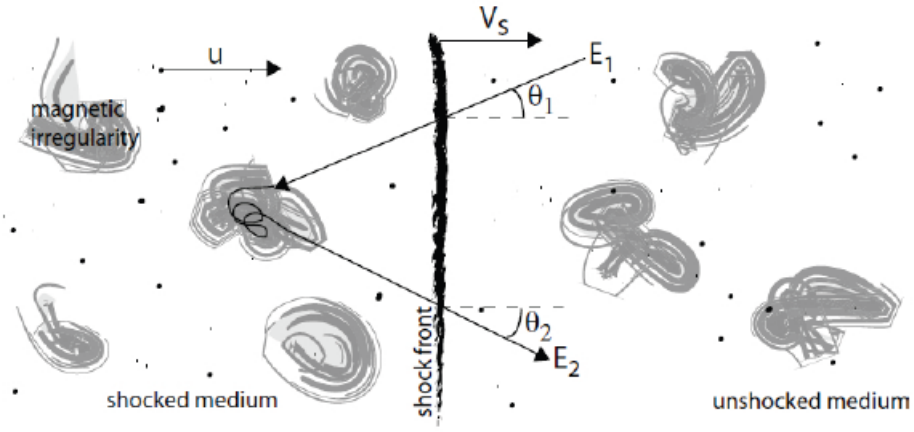

Figure 1.8. A schematic picture of the shock acceleration mechanism. (Figure from [74]).

When a relativistic particle of energy E_1 crosses the wavefront from the unshocked medium to the shocked one with an angle θ_1, its energy, in the shocked frame is $E_1' = \Gamma E_1(1 + \frac{u}{c}\cos\theta_1)$, where $\Gamma = (1 - \frac{u^2}{c^2})^{-\frac{1}{2}}$. During the elastic scattering this energy remains unchanged.
When the particle enters again in the unshocked medium, with an angle θ_2', its energy becomes $E_2 = \Gamma^2 E_1(1+\frac{u}{c}\cos\theta_1)(1+\frac{u}{c}\cos\theta_2')$. For isotropic fluxes, the mean values of $cos\theta_1$ and $\cos\theta_2'$ for particles crossing the wavefront are $\langle cos\theta_1\rangle = \langle\cos\theta_2'\rangle = 2/3$. The increment in energy ϵ is

$$\epsilon = \left\langle \frac{\Delta E}{E} \right\rangle = \frac{E_2 - E_1}{E_1} = \frac{4}{3}\frac{u}{c} = \frac{V_s}{c}$$

where terms of second order in u/c have been left out. In this way, every time the particle crosses the shock wave, on average its energy increases for a constant factor.
Particles are taken outside the shock region together with the shocked material with velocity $V_s/4$. The number of particles escaping the source per unit time and surface is therefore $\rho V_s/4$, where ρ is the particles' density of the region. The flux of particles that come back to the unshocked region can be found projecting an isotropic flux on the wavefront plane, obtaining $\rho c/4$. So, the probability that a particle goes to the shocked region is $P_{\rm esc} = V_s/c$. Combining a constant increasing of energy with a constant probability to escape, we get a power law spectrum:

$$\frac{dN}{dE} \propto E^{-\gamma} \propto E^{\frac{\ln(1-P_{\rm esc})}{1+\epsilon}-1} \tag{1.5}$$

The values of $P_{\rm esc}$ and ϵ found above determine a spectral index $\gamma = 2$, even if detailer calculations indicate values between 2.1 and 2.5 (see [65]).

In the fireball model, the observed radiation is produced, both during the GRB and the afterglow, by synchrotron emission of shock accelerated electrons. In the region where electrons are accelerated, protons are also expected to be shock accelerated. Protons' acceleration

to energies greater than 10^{20} eV would be responsible for the production of ultra high energy cosmic rays (UHECRs), that are CRs of energy greater than 10^{18} eV. This could be possible, provided that the wind bulk Lorentz factor is large enough ($\Gamma > 100$) and that the magnetic field is close to equipartition between protons and electrons. For further details, see [88].

Indeed, the observed CRs differential spectrum can be model through a broken power law, for energies between 10^{11} eV and 10^{20} eV:

$$\phi(E) = C \begin{cases} E^{-2.7} & E < E_1, E > E_2 \\ E^{-3.1} & E_1 \leq E \leq E_2 \end{cases} \tag{1.6}$$

where $E_1 = 10^{15.5}$ eV is called the "knee", in correspondence to astrophysical contributions (like magnetic confinement inside the source) able to modify the spectral slope, and $E_2 = 10^{18.8}$ eV is the "ankle", where a contribution of extra-galactic origin is expected. The differential flux is illustrated in Figure 1.9.

The spectral index measured for the energy spectrum of CRs is slightly different from the

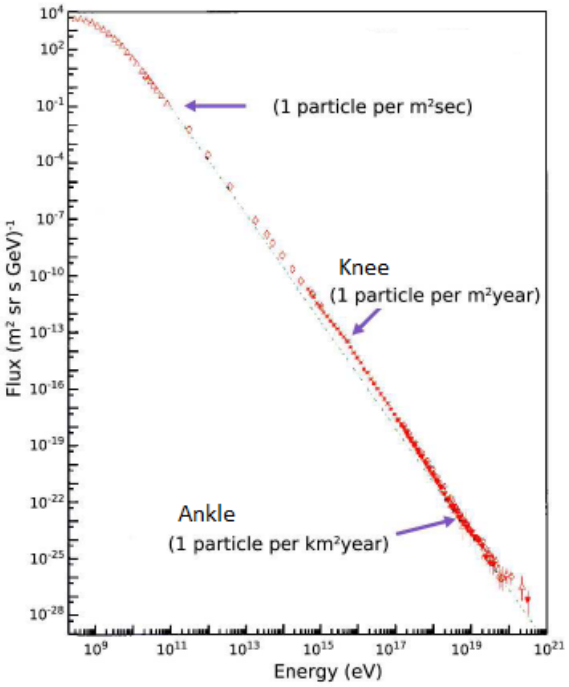

Figure 1.9. CRs energy spectrum observed on Earth.

expected $\gamma = 2$, according to the I order Fermi acceleration mechanism. This can be understood considering the confinement time of CRs in the magnetic field of our Galaxy, that is clearly a function of energy because of the dependence of the escape length on it.
CRs energy spectrum has a lower limit, corresponding to $E \sim 10^9$ eV, due to the difficulties faced from charged particles with a typical energy of 1 GeV of entering the Solar System, where a diffuse plasma emitted by the Sun during high energy flaring episodes is present.
It is difficult to establish if this spectrum also possesses an upper limit, because of the even reduced number of particles with increasing energy. Measurements of the spectrum in the region of UHECRs would be really important because the presence of such high energy particles have to be justified with some mechanism able to produce them. This search is also important to eventually unveil the "Greisen Zatsepin Kuz'min effect" (briefly called GZK), that is a huge reduction of primary CRs flux above $\sim 10^{20}$ eV due to their interaction with the CMB (see [52] and [90]). The exact threshold energy depends on the composition of primary CRs, being lower for lighter nuclei. Some efforts have been done in this direction,

with the Pierre Auger Observatory, the Agasa Telescope Array and the HI-RES experiment, but contradictory results have come out: they are presented in Figure 1.10. While Agasa Telescope Array doesn't see a flux reduction at energies higher than 10^{20} eV, HI-RES and Pierre Auger do, therefore a clear answer is still to be found.

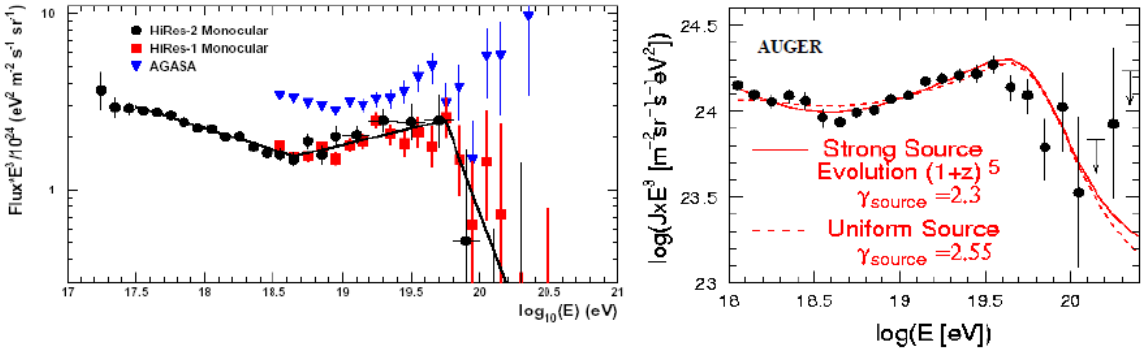

Figure 1.10. UHECRs energy spectrum: on the left the contradictory results between HI-RES, that sees a reduction in the high energy proton flux, and AGASA Telescope Array, that doesn't see it, are shown. On the right side Pierre Auger Observatory's results are presented, confirming the HI-RES results; two fits to this spectrum, assuming no evolution of the UHECR sources and a redshift-dependent evolution, are also reported. (For further details see [78]).

Two broad classes of models have been proposed to explain the origin of UHECRs: **"top-down"** scenarios, which attribute UHECRs to decay of fossil Grand Unification defects, and **"bottom-up"** scenarios, which assume that UHECRs are accelerated in astrophysical sources. One of the most prominent candidate sources for bottom-up scenarios are GRBs (other two being AGN and cluster shocks): the persuasiveness of this scenario is largely based on two coincidences, namely

- the required condition to accelerate proton to GZK energies is similar to the requirement for generating the prompt observed γ-rays in GRB;
- the observed UHECRs energy injection rate into the Universe ($\sim 3 \times 10^{44}$ erg Mpc^{-3} yr^{-1}) is similar to the local GRB γ-ray energy injection rate.

Further research have to be carried on to disentagle between the two scenarios (top-down and bottom-up) and to reveal whether a GZK effect indeed exists. Within the bottom-up scenario, the directional information may either prove or significantly constrain the alternative AGN scenario and may eventually shed light on whether GRBs are really sources of UHECRs.

1.6 Models for neutrinos emission

Waxman & Bahcall ([86]) were the first to calculate the expected neutrino flux in coincidence with the electromagnetic GRB in the framework of the standard fireball internal shock model, using averaged burst parameters as measured by the BATSE instrument on-board the CGRO. Their calculation was based on the assumption of Fermi accelerated protons in the relativistic ejecta of the burst interacting with the associated photon field to produce pions via the Δ^+ resonance. Protons are assumed to follow a power law like distribution from the Fermi acceleration, while the photon field corresponds to the measured electromagnetic spectra at Earth; for simplicity reasons, the authors based their first calculations on a broken power law spectrum with typical photon indices $\alpha = -1$, $\beta = -2$ and a transition at the break energy $E_\gamma = 1$ MeV.

The photo-hadronic interaction via the Δ^+ resonance produce charged and neutral pions, where the subsequent decay of the charged pions and muons gives rise to a high energy neutrino signal accompanying the electromagnetic emission:

$$p+\gamma \xrightarrow{\Delta^+} \begin{cases} p+\pi^0 \\ n+\pi^+ \end{cases} \longrightarrow \begin{array}{l} \pi^0 \longrightarrow \gamma+\gamma \\ n \longrightarrow p+e^-+\overline{\nu}_e \\ \pi^+ \longrightarrow \mu^+ + \nu_\mu \\ \mu^+ \longrightarrow e^+ + \nu_e + \overline{\nu}_\mu \end{array} \tag{1.7}$$

The cross section of the resonant process is $\sigma_{p\gamma} = 5 \times 10^{-28}$ cm^2.
From Equation 1.7, it is possible to illustrate the production of cosmic ray protons (ignoring for the moment that the composition of cosmic rays may be heavier at high energies). First of all, some of the protons injected into the interaction volume may escape, leading to cosmic ray production. However, even if the protons are magnetically confined, the neutrons, which are electrically neutral, can easily escape if the source is optically thin to neutron escape.
Within this picture, the shape of the neutrino flux is basically determined by the proton and photon field distributions, with a steepening of the neutrino spectrum introduced by the photon spectral break. The authors emphasize that the secondary charged pions would be subject to synchrotron losses in the ambient magnetic field similarly to the electrons, such that high energy pions efficiently loose energy before they can decay. This introduces a second steepening of the neutrino energy distribution. Waxman & Bahcall normalized the neutrino spectrum assuming that GRBs are the unique sources of the cosmic ray flux between 10^{10} GeV and 10^{12} GeV and that CRs flux is composed entirely of protons. Their prediction is referred to as the standard Waxman-Bahcall GRB neutrino flux and was for instance used to set limits on the coincident neutrino flux from GRBs with the BAIKAL (see [41]) and AMANDA (see [19]) experiments.
Guetta et al. (see [53]) modified the model of Waxman and Bahcall to derive individual neutrino fluxes for the bursts, one for each neutrino family and for each weak charge. In addition to accounting for the particular parameters of each GRB, the authors introduced a per-burst normalization of the neutrino prediction based on the respectively measured photon fluence. The prompt neutrino spectrum (see [4], Appendix A) is thus given by a double broken power law:

$$F_\nu(E_\nu) = \frac{dN(E_\nu)}{dE_\nu} = f_\nu \begin{cases} \left(\frac{E_1}{\mathrm{GeV}}\right)^{\alpha_\nu} \left(\frac{E_\nu}{\mathrm{GeV}}\right)^{-\alpha_\nu} & E_\nu < E_1 \\ \left(\frac{E_1}{\mathrm{GeV}}\right)^{\beta_\nu} \left(\frac{E_\nu}{\mathrm{GeV}}\right)^{-\beta_\nu} & E_1 \leq E_\nu < E_2 \\ \left(\frac{E_1}{\mathrm{GeV}}\right)^{\beta_\nu} \left(\frac{E_2}{\mathrm{GeV}}\right)^{\gamma_\nu-\beta_\nu} \left(\frac{E_\nu}{\mathrm{GeV}}\right)^{-\gamma_\nu} & E_\nu \geq E_2 \end{cases} \tag{1.8}$$

where neutrino indices are related to photon indices through the following relations:

$$\alpha_\nu = 3+\beta \quad \beta_\nu = 3+\alpha \quad \gamma_\nu = \beta_\nu + 2$$

and the break energies are:

$$E_1 = 5 \times 10^5 \mathrm{GeV} \Big(\frac{1}{1+\mathrm{z}}\Big)^2 \Big(\frac{\Gamma}{10^{2.5}}\Big)^2 \Big(\frac{\mathrm{MeV}}{E_\gamma}\Big)$$

$$E_2 = 10^7 \mathrm{GeV} \frac{1}{1+\mathrm{z}} \sqrt{\frac{\mathrm{e}_E}{\mathrm{e}_B}} \Big(\frac{\Gamma}{10^{2.5}}\Big)^4 \Big(\frac{t_{\mathrm{var}}}{0.01\mathrm{s}}\Big) \sqrt{\frac{10^{52}\mathrm{erg/s}}{L_\gamma^{\mathrm{iso}}}}$$

The first break is introduced by the steepening of the photon spectrum at E_γ and is thus due to effective synchrotron cooling of the electrons in the magnetic field. The same mechanism leads to energy losses of the secondary muons resulting in another steepening of the neutrino flux at

E_2, which therefore also depends on the fraction of the total jet in electrons e_E and in magnetic field e_B. The dimensionless parameter e_E measures the fraction of the internal energy e which goes into random motions of the electrons $e_E = U_e/e$, while e_B is the ratio between the magnetic field energy density and the total thermal energy, $e_B = U_B/e = B^2/(8\pi e)$. The jet Lorentz boost factor Γ and the assumed isotropic luminosity $L_\gamma^{\rm iso}$ (in case of no collimation of the outflow) as well as the variability time scale $t_{\rm var}$ also influence the energy breaks. The term (1 + z) accounts for the cosmological redshift z of the GRB.
The normalization depends on the strength of the photon flux as well as on the total fraction of the energy transferred from protons to pions. On average, 20% of the proton energy is transferred to the pion in each interaction ([53] and [86]), so that $\langle x_{p\to\pi}\rangle = 0.2$. In total, $1-(1-\langle x_{p\to\pi}\rangle)^{\Delta R/\lambda_{p\gamma}}$ of the energy is converted, where ΔR is the size of the shock region and $\lambda_{p\gamma}$ is the mean free path of a proton for photo-meson interactions. Their ratio is given by

$$\frac{\Delta R}{\lambda_{p\gamma}} = \Big(\frac{L_\gamma^{\rm iso}}{10^{52}{\rm erg/s}}\Big)\Big(\frac{10^{2.5}}{\Gamma}\Big)^4\Big(\frac{0.01{\rm s}}{t_{\rm var}}\Big)\Big(\frac{\rm MeV}{E_\gamma}\Big) \tag{1.9}$$

This yields the neutrino spectrum normalization of

$$\int_0^\infty dE_\nu F_\nu(E_\nu) = \frac{1}{8}\frac{1}{e_E}(1-(1-\langle x_{p\to\pi}\rangle)^{\Delta R/\lambda_{p\gamma}})\int_{E_{\rm min}}^{E_{\rm max}} dE_\gamma F_\gamma(E_\gamma) \tag{1.10}$$

where the gamma fluence F_γ is measured by the burst alert satellite and $f_P = 1/e_E$ is called baryonic loading. The factor 1/8 takes into account that charged and neutral pions are produced with roughly equal probabilities and that each neutrino carries 1/4 of the pion energy (pion energy is assumed to be equally distributed between the four final leptons).
The intrinsic parameters of the emission regions like the boost factor, the energy partitions in the jet and the variability time scales cannot reliably be determined and are usually set to default values, as shown later in Table 3.2.
In principle, different break energies are predicted for muon neutrinos and antineutrinos, since the first are produced in pion decay, while the latter are produced in muon decay (see [53], Equation A10 and A11, Equation 2.1), therefore different lifetimes of decaying particles account for different break energies (muon lives 100 times more than pion). This yields three breaks in the combined $\nu_\mu + \overline{\nu}_\mu$ spectrum. In previous ANTARES analyses ([11] and [79]) this effect has been accounted for. Other searches with the RICE and ANITA experiments made use of the simplified predictions. Last IceCube searches also account for it (see [7]).
However, more recent calculations for instance by Hümmer et al. (see [57]) demonstrated that the neutrino flux predictions from Guetta (see [53]) are reduced by one order of magnitude when taking into account the full photon distribution, the full width of the Δ^+ resonance, the energy losses of secondary particles and the energy dependence of the proton mean free path in the source. Furthermore, the group developed numerical calculations of GRB neutrino spectra based on the Monte Carlo algorithm SOPHIA (see [69]) to simulate the underlying particle physics. Their "Neutrinos from Cosmic Accelerators" code (NeuCosmA) is described and discussed in detail in [58], [32], [33] and [89]. In Figure 1.11 a comparison between the analytical Guetta model and the numerical NeuCosmA model is presented.

NeuCosmA accounts for the full proton-photon cross section and includes not only the interaction via the Δ^+ resonance (Equation 1.7), but also the production of kaons leading to a high-energy component in the ν_μ flux via:

$$\begin{aligned} p+\gamma \longrightarrow & K^+ + \Lambda/\Sigma \\ & K^+ \longrightarrow \mu^+ + \nu_\mu \end{aligned} \tag{1.11}$$

In addition, the authors emphasize that simultaneously produced multiple pions dominate the photo-hadronic cross section above ~ 1 GeV. The decay of the negatively charged pions

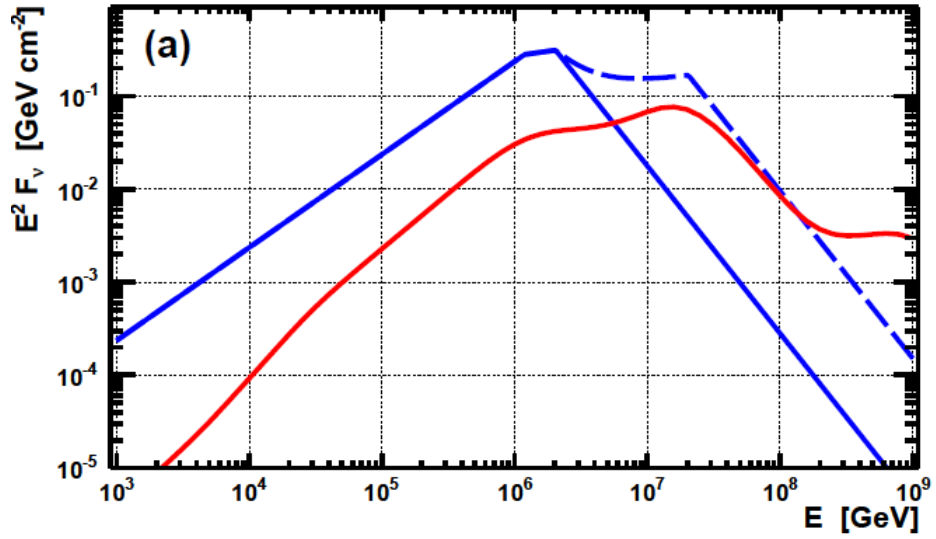

Figure 1.11. Predicted neutrino spectra E^2F_ν versus neutrino energy from $\nu_\mu + \overline{\nu}_\mu$ for one of the most ever intense GRB, GRB110918. The analytical model by Guetta et al. (blue) is shown with a simple treatment (blue solid) and accounting for different break energies of ν_μ and $\overline{\nu}_\mu$ (blue dashed). The numerical NeuCosmA prediction is presented in red. (Figure from [80]).

also contributes to the expected neutrino flux via:

$$\begin{aligned} \pi^- &\longrightarrow \mu^- + \overline{\nu}_\mu \\ \mu^- &\longrightarrow e^- + \overline{\nu}_e + \nu_\mu \end{aligned} \tag{1.12}$$

The interaction products and their energy losses are treated individually and the mixing of neutrino flavors on their way to Earth is included. No new assumptions on the sources are introduced, but known particle physics governing the photo-hadronic interactions are applied in greater detail within the fireball model. A published search from ANTARES (see [79]) had already employed the second-generation numerical calculations: ANTARES results for a search from 2007 to 2011 with 296 GRBs were of non-observation. IceCube also employed second generation numerical code in its latest analysis (see [1] for the more recent results): its search from 2008 to 2012 with 506 GRBs founded a low-significance coincidence of a neutrino event with one of the burst, consistent with the expectation from atmospheric background. More observations are therefore needed in order to constrain the fireball model.

NOTE: Neutrino's flux calculations are insensitive to the beaming effect caused by a narrow opening angle of the jet as all formulae contain the isotropic luminosity in conjunction with a 4π shell geometry, i.e. effectively use luminosity per steradian.

1.7 Gravitational waves

The γ-rays and the afterglows of GRB are thought to be produced at distances from the central engine where the plasma has become optically thin, R $\geq 10^{13}$ cm, which is much larger than the Schwarzschild radius of a stellar mass black hole or neutron star ($R_S = \frac{2GM}{c^2} \sim 3$ Km for $M = M_\odot$). Hence we have only very indirect information about the inner parts of the central engine where the energy is generated. However, in any stellar progenitor model of GRB one expects that gravitational waves should be emitted from the immediate neighbourhood of the central engine and their observation should give valuable information about its identity. Therefore, it is of interest to study the gravitational wave emission from GRB associated with specific progenitors. Another reason for doing this is that the present and

foreseeable sensitivity of gravitational wave detectors is such that for likely sources, including GRBs, the detections would be difficult and for this reason much effort has been devoted to the development of data analysis techniques that can reach deep into the detector noise. A coincidence between a gravitational wave signal and a γ-ray signal would greatly enhance the statistical significance of the detection of the gravitational wave signal. It is therefore of interest to examine the gravitational wave signals expected from various specific GRB progenitors that have been proposed and, based on current astrophysical models, to consider the range of rates and strains expected in each case, for comparison with the nowadays sensitivity.
Regardless of whether they are associated with GRBs, binary compact object mergers (NS-NS, NS-BH, BH-BH, BH-WD, BH-Helium star etc.) and stellar core-collapses have been studied as potential gravitational wave (GW) sources.
A binary coalescence process can be divided into three phases: in-spiral, merger and ring-down. The GW frequencies of various phases cover the $10 - 10^3$ Hz band, which is relevant for the Laser Interferometer Gravitational-wave Observatory (LIGO), constituted by two detectors both located in USA (see [64]), and other related detectors such as Virgo, located in Italy (see [85]). Because of the faint nature of the typical GW strain, only nearby sources (e.g. within $\sim$ 200 Mpc for NS-NS and NS-BH mergers) have strong enough signals to be detectable by the Advanced LIGO and Virgo, the next generation of ground-based interferometers that will soon start data-taking. When event rates are taken into account, estimates indicate that after one-year operation of the Advanced LIGO and Virgo, one event for the in-spiral chirp signal of NS-NS or NS-BH merger would be detected. Other binary merger scenarios such as BH-WD and BH-Helium star mergers are unlikely to be detectable due to the low estimates obtained for the maximum non-axisymmetrical perturbations; moreover, they are unfavoured sources of GRBs.
A time-integrated GW luminosity of the order of a solar rest mass ($\sim 10^{54}$ erg) is predicted from merging NS-NS and NS-BH models, while the luminosity from collapsar models is more model-dependent, but expected to be lower. If some fraction of GRBs are produced by Double Neutron Stars (DNS) or NS-BH mergers, the gravitational wave chirp signal of the in-spiral phase should be detectable by the Advanced LIGO and Virgo within one year, associated with the GRB electromagnetic signal. The most promising GW-GRB candidates in terms of detections per year are DNS and BH-NS mergers, based on the assumed mean distance in the formation rate. For further details, consult [68].

Gravitational wave burst searches are underway with LIGO and Virgo. Another interferometer is under construction: the Evolved Laser Interferometer Space Antenna (eLISA), a second generation GW detector that will be deployed in the space, where the noise is strongly reduced. In Figure 1.12 the current GW detectors are shown, while in Figure 1.13 and 1.14 the sensitivity plots for the Advanced LIGO/Virgo and eLISA are reported.

Figure 1.12. Gravitational wave detectors in the world. (Figure from [46]).

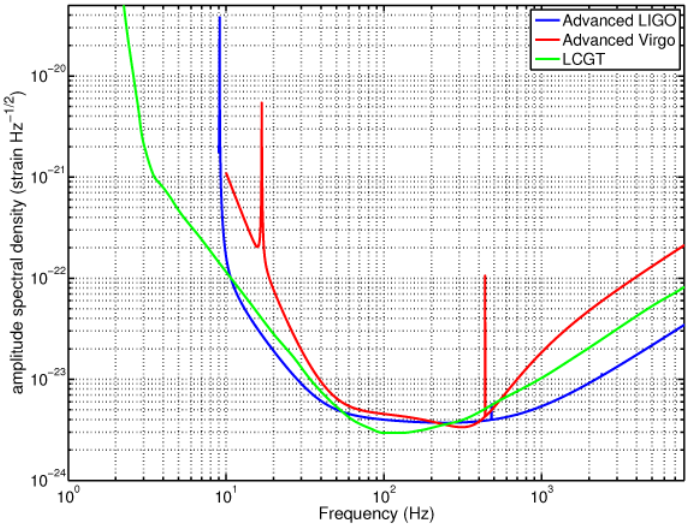

Figure 1.13. Sensitivity plot of the Advanced LIGO and Virgo interferometers. (Figure from [46]).

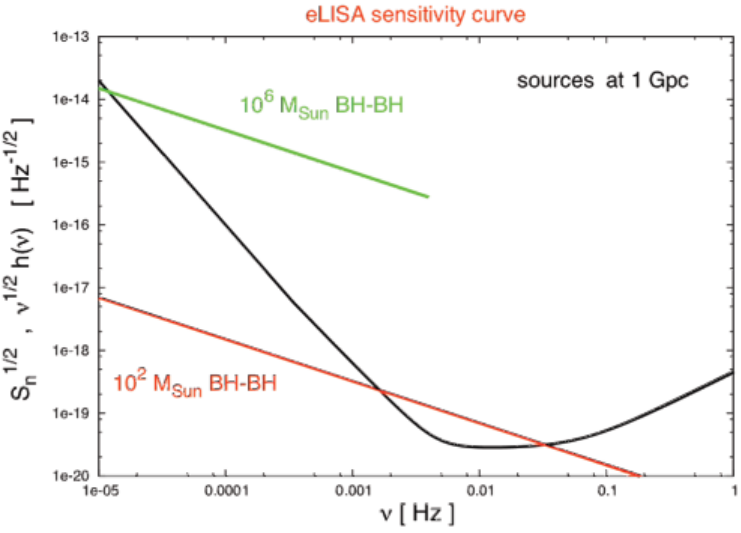

Figure 1.14. Sensitivity plot of eLISA, the next generation interferometer. (Figure from [46]).

Chapter 2

The ANTARES Neutrino Telescope

Astronomy with neutrinos implies the presence of a detector, which we call telescope, in the extended sense of the word, that is an instrument to watch far away in space (then also in time).
Neutrino is a particle whose most important characteristics are:

1. no electric charge (so it doesn't interact through electro-magnetic force);
2. a little mass (so it scarcely interacts gravitationally);
3. weakly interacting.

The last property is a great opportunity for discoveries in astrophysics and astronomy as well as a giant obstacle for neutrinos detection. In addition, to make things more difficult, neutrino flux predictions compute a decreasing number of events as energy increases, as is shown in Figure 2.1. Therefore, neutrinos are very hard to detect and high-energy cosmic neutrinos are even harder.

The strategy to catch neutrinos consists in collecting a signature of the passage of charged particles produced during their interaction: this implies that neutrinos should interact in the proximity of the detector or inside the detector volume. Therefore, the first requirement a cosmic neutrino detector should fulfil is to be huge, in order to intercept the faint flux of neutrino events at high energies. Moreover, it has to be massive, since a large amount of target nucleons are necessary to produce a neutrino interaction, because of the small neutrino-nucleon cross section. These two considerations drive to the conclusion that a natural target has to be employed, as oceanic water (or Antarctic ice), since no human-made laboratory could ever be large enough to host such an apparatus. Secondly, if a neutrino interaction has occurred, the telescope should be able to identify the products of the interaction. As it will be accounted for in Section 2.1, a neutrino-nucleon interaction can result in hadrons and leptons. Detection techniques differ since they concentrate in discovering signatures of different secondary products of neutrino interactions. In all cases, however, the signal revealing the presence of secondary particles has to be transmitted through the detector volume, in order to be collected and recorded: light, in case of optical Cherenkov telescopes, or sound in case of the acoustic technique (or radio signals, when considering the radio detection in ice). The water volume thus operates as the medium for signal transmission.

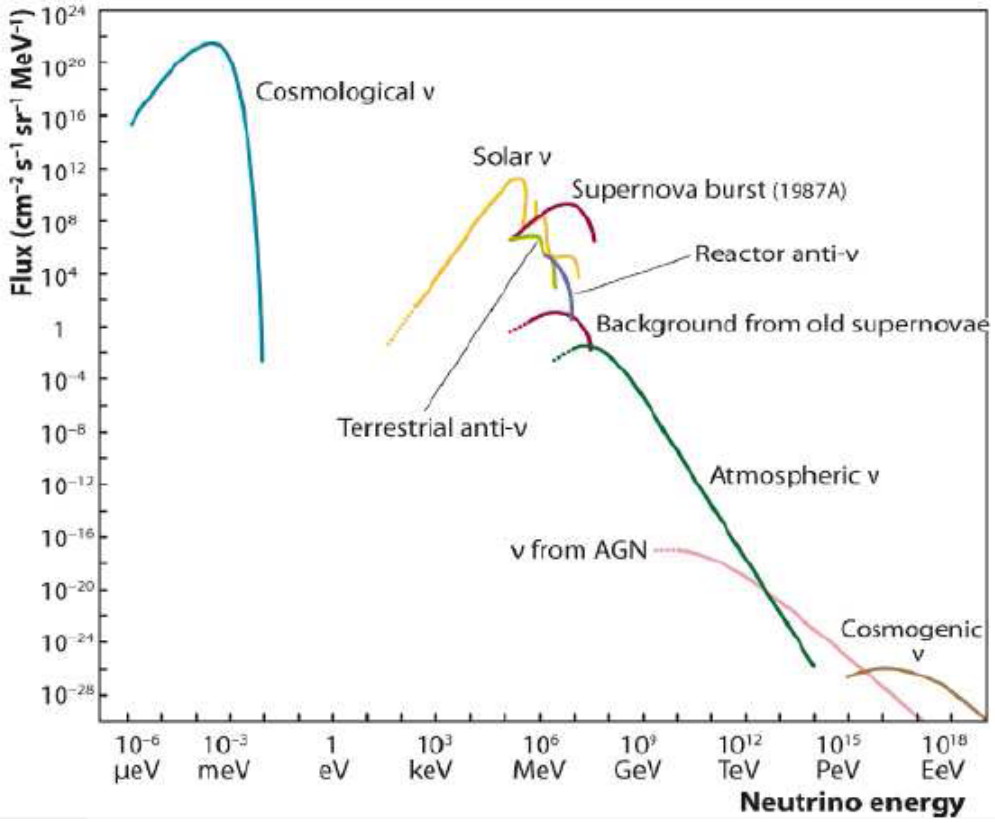

Figure 2.1. Neutrino flux predictions for different neutrinos sources: cosmological neutrinos represent the residual background from Big Bang (Cosmic Neutrino Background or CNB), solar neutrinos are from nuclear reactions inside the Sun; then, neutrinos from SN1987, terrestrial antineutrinos from the decay of radioactive elements, reactor antineutrinos, atmospheric neutrinos, AGN neutrinos and cosmogenic neutrinos from the decay of topological defects according to top-down models.

2.1 Neutrino physics and interaction

In the framework of the Standard Model, neutrinos weakly interact with nucleons by deep inelastic scattering, through charged current (CC) and neutral current (NC) processes:

$$\text{CC: } \nu_l\,(\overline{\nu}_l) + N \longrightarrow l^-\,(l^+) + X \tag{2.1}$$

$$\text{NC: } \nu_l\,(\overline{\nu}_l) + N \longrightarrow \nu_l\,(\overline{\nu}_l) + X \tag{2.2}$$

where l indicates the leptonic flavor ($l = e, \mu, \tau$), N the target nucleon, X the hadronic cascade originating in the interaction. Almost 80% of the initial neutrino energy stays in the leptonic channel. Figure 2.2 shows different kinds of neutrino interaction, while Figure 2.3 displays cross-sections for νN interactions at high energies.

2.2 Neutrino detection strategy

The ANTARES underwater neutrino telescope is primarily designed for detecting highly relativistic muons from CC interactions of cosmic muon neutrinos with matter in or close-by to the detector. The passage of these muons through the seawater induces the emission of Cherenkov light, that is then detected by a three dimensional array of photomultiplier tubes (PMTs). This process takes its name after the Russian scientist P.A. Cherenkov, who first described it: he received the Nobel Prize in Physics in 1958, "for the discovery and the interpretation of the Cherenkov effect" (see [72]). Instead, the first proposal to employ the

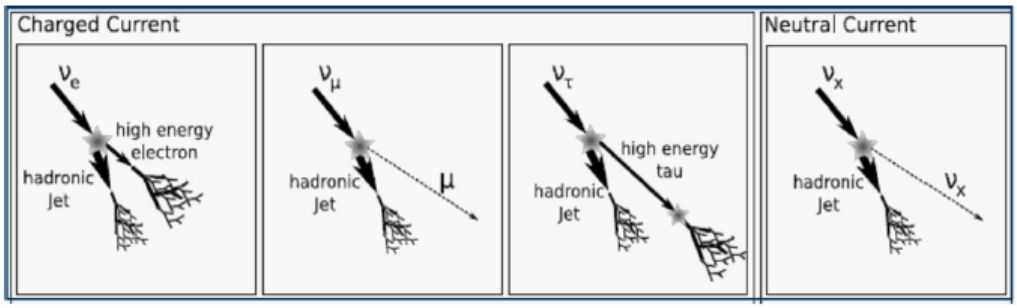

Figure 2.2. Different kinds of neutrino interactions: CC interaction produces a charged diffuse lepton and a hadronic shower. If ν_e is interacting the produced electron generates an electromagnetic shower, if ν_μ is interacting a muon track is produced because the muon is penetrating, if ν_τ is interacting the τ decays and generates a new ν_τ. NC interaction just produces an undetectable diffuse neutrino and a hadronic shower.

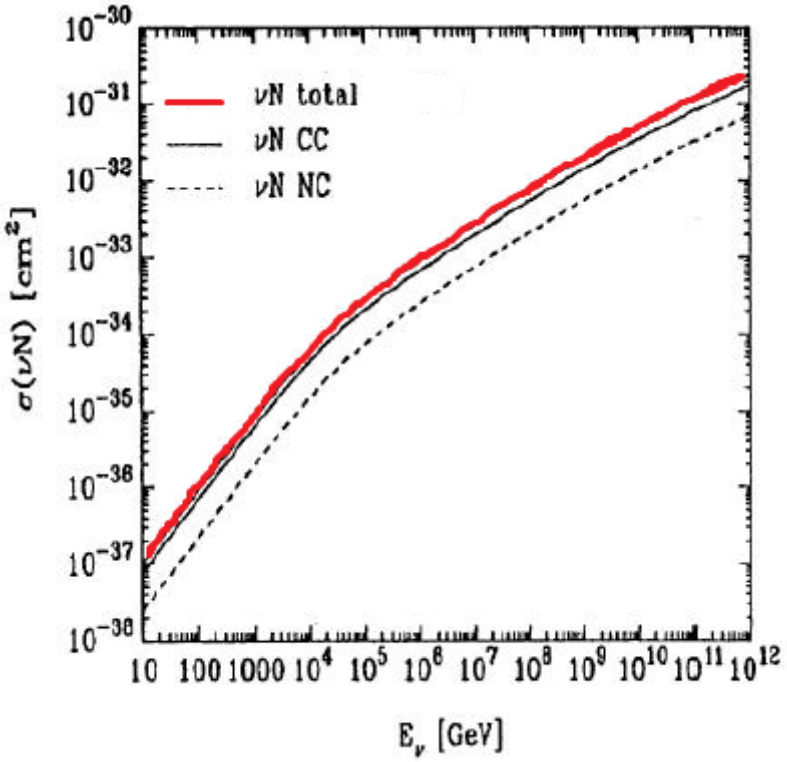

Figure 2.3. High energy neutrino-nucleon cross section. (Figure from [48]).

Cherenkov technique for neutrino detection in submarine environment dates back to the '60s, by Markov and Zheleznykh (see [66].)
Using the time and position information of the detected photons, the muon trajectory is reconstructed, from which the original neutrino direction can be inferred. The optical Cherenkov telescopes constitute the present generation detectors for high-energy neutrinos in ice and water: an artistic view of the detection technique is represented in Figure 2.4.

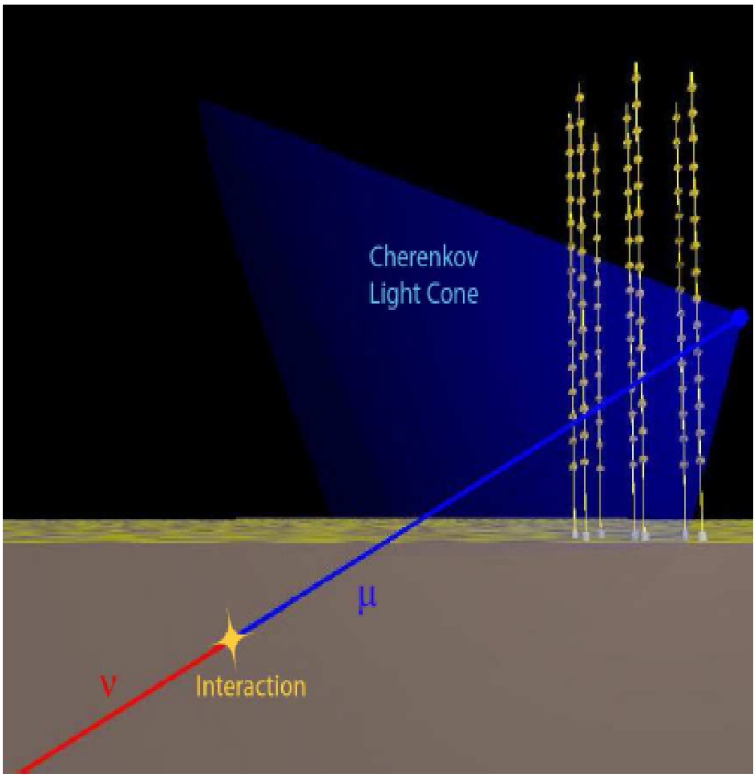

Figure 2.4. Detection principle of high energy muon neutrinos in an underwater neutrino telescope. The incoming neutrino interacts with the material around the detector to create a muon. The muon induces the emission of Cherenkov light in the sea water which is then detected by a matrix of light sensors. The original spectrum of light emitted from the muon is attenuated in the water such that the dominant wavelength range detected is between 350 and 500 nm.

Cherenkov radiation is produced when a charged particle (which for the ANTARES "golden" channel is the secondary muon produced during a CC ν_μ interaction) moves in a transparent medium, of refractive index n, with a velocity greater then light velocity in the medium (c/n). This radiation is emitted from the medium itself, due to polarization and depolarization effects of atoms in the medium because of a relativistic charge passing by. These charge motions around each point touched by the particle (the muon) generate a series of spherical waves, whose envelope constitutes a conic wavefront: the cone axis is coincident with the particle track and its aperture is definite, as shown in Figure 2.5. The "Cherenkov angle" θ_C is indeed fixed by the medium refractive index and satisfies the following relation:

$$\cos\theta_C = \frac{1}{\beta n}$$

For ultrarelativistic particles ($\beta \sim 1$) in water ($n_{water} = 1.333$), the Cherenkov angle is $\theta_C \sim 41°$. The number of photons per unit length x induced by a relativistic unitary charge

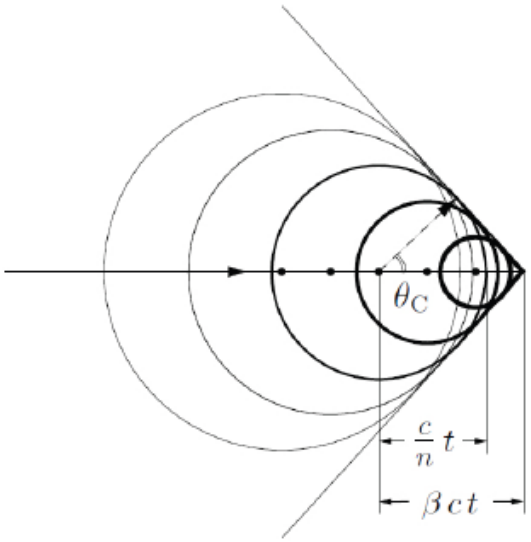

Figure 2.5. Geometry of the Cherenkov radiation emission. The Cherenkov angle is in evidence.

is

$$\frac{d^2N_\gamma}{dxd\lambda} = \frac{2\pi\alpha}{\lambda^2}\Big(1 - \frac{1}{\beta^2 n^2(\lambda)}\Big)$$

where α is the fine structure constant and λ is the photons' wavelength. For further details see [40].
Optical frequencies are the more interesting to reveal neutrinos with energy between 100 GeV and 10 PeV: for wavelengths in [300;700] nm, that is for a wide transmitting length in a natural medium as water or ice (water transmitting length reaches 60 m at wavelengths of 415 nm), the number of Cherenkov photons per unit length is:

$$\frac{dN_\gamma}{dx} \sim 200\text{cm}^{-1}$$

The background in a neutrino telescope is mainly made of atmospheric muons and neutrinos (as Figures 2.6 and 2.7 show), produced by pions and kaons decay, where pions and kaons come from the interaction of primary CRs with the nuclei of Earth atmosphere.
Atmospheric muons have enough energy to traverse the whole atmosphere and many kilometres in water so that they can reach the neutrino telescope through the water or ice deepness in which it is placed. Muons flux depends on the quantity of matter traversed and can be estimated considering the energy ionisation losses, dE/dx: muons reaching the detector are essentially down-going, that is coming from above the detector's horizon. So this background can be reduced selecting just up-going tracks, as is shown in Figure 2.8. Atmospheric neutrinos background is, instead, unavoidable: the difference between atmospheric and astrophysical neutrinos can be found only looking at their energy spectra. Indeed atmospheric neutrinos have a harder spectrum than cosmic neutrinos, therefore at high energies the astrophysical contribution should exceed the atmospheric one. It has been shown in Figure 2.3 that νN cross section σ increases with energy. The transmission probability P_{Earth} through Earth is defined as:

$$P_{\text{Earth}}(E_\nu) = \exp\Big[-N_A\sigma_\nu(E_\nu)\int \rho(\theta, l)\, dl\Big] \tag{2.3}$$

where N_A is the Avogadro number, $\rho(\theta, l)$ is the Earth profile density as a function of the neutrino direction θ and of the length made inside the Earth l.

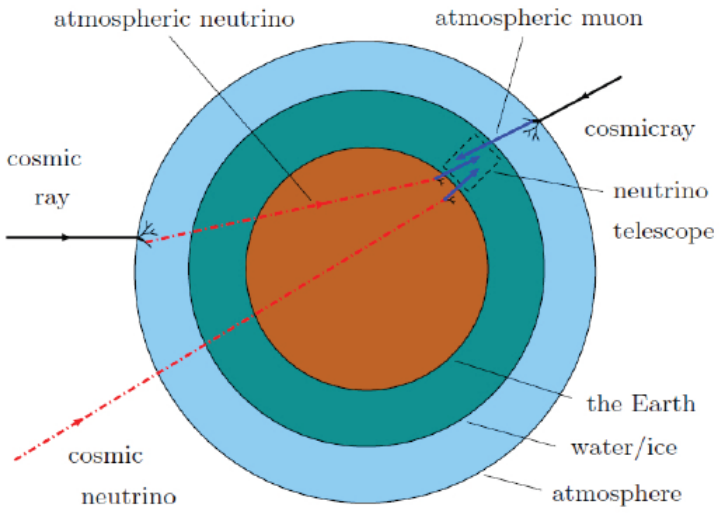

Figure 2.6. Picture showing the deepness reached in the Earth by atmospheric muons and neutrinos versus cosmic neutrinos.

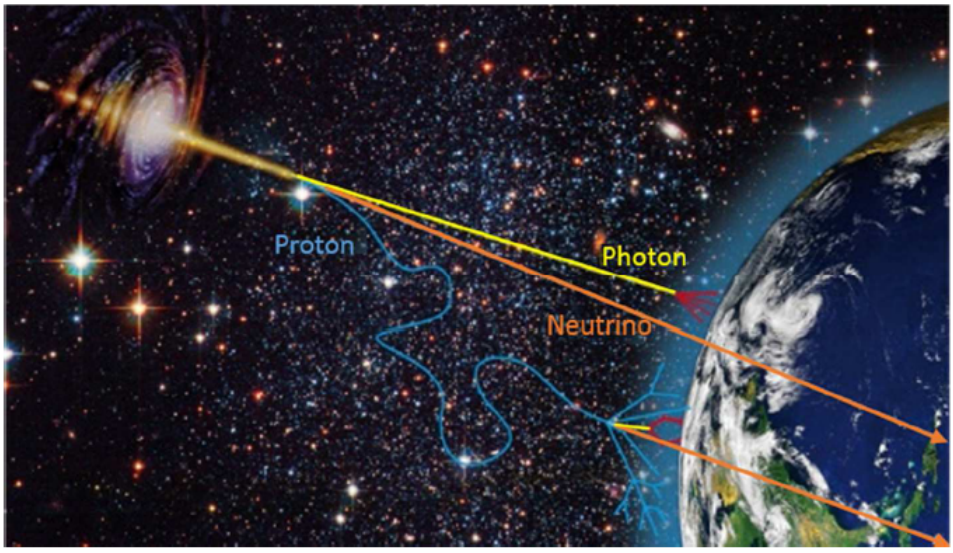

Figure 2.7. Picture showing the two different origin of neutrinos detected on Earth: atmospheric and astrophysical neutrinos.

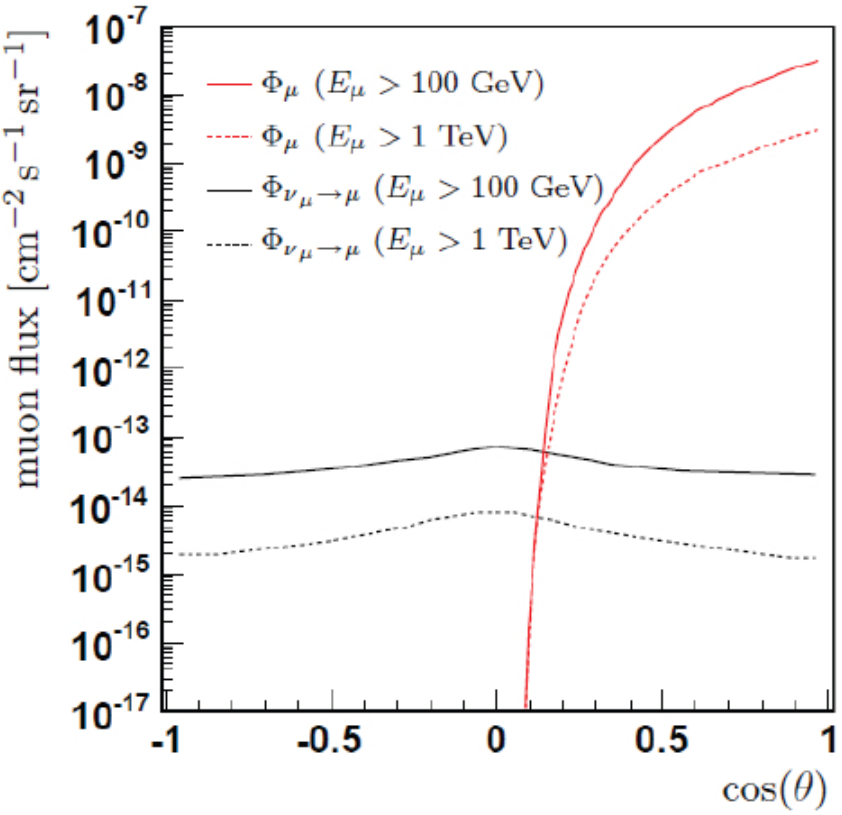

Figure 2.8. Flux from atmospheric muons (in red) and from muons induced by atmospheric neutrinos (in black) at 2.1 km water equivalent (w.e.) versus the cosine of the muon zenith angle. Atmospheric muons are down-going. Atmospheric neutrinos flux increases in the horizontal direction, because in this longer region pions and kaons have a greater probability to decay.

At energies E>10 PeV the Earth becomes opaque to up-going neutrinos: it is possible to observe them only if they come from above the horizon (down-going). To reduce the contamination from atmospheric muons, the signal to look for is an extremely energetic track quite horizontal.

2.3 Detector layout

The ANTARES Collaboration was formed in 1996 with the goal to construct and operate a neutrino telescope in the Mediterranean Sea. The Collaboration consists of physicists, engineers and sea scientists from 29 institutes and 7 European countries (see Figure 2.9). The first ANTARES line was deployed in spring of 2006 and the telescope was completed in May 2008 with the deployment of the last line.
ANTARES is the greatest neutrino telescope in the Northern hemisphere: it is placed 40 km off the coast of Toulon (France), 2475 m deep in the water. In Figure 2.10 it is possible to see its geographical position.
Pioneering experiments, of which ANTARES represents the result of technological improvement, are DUMAND (see [54]) and BAIKAL (see [41]), in the same way as IceCube is with respect to AMANDA (see [19]).

Now, I will describe the elements constituting the detector, from the smallest to the biggest. The basilar unit is the Optical Module (OM), whose picture can be seen in Figure 2.11: it is made of a glass sphere, 43 cm in diameter and 15 mm in thickness, able to resist to a pressure as high as 700 bar. Inside this sphere there is a Hamamatsu R7081-20 photomultiplier tube

Figure 2.9. The location of the institutes in the ANTARES Collaboration.

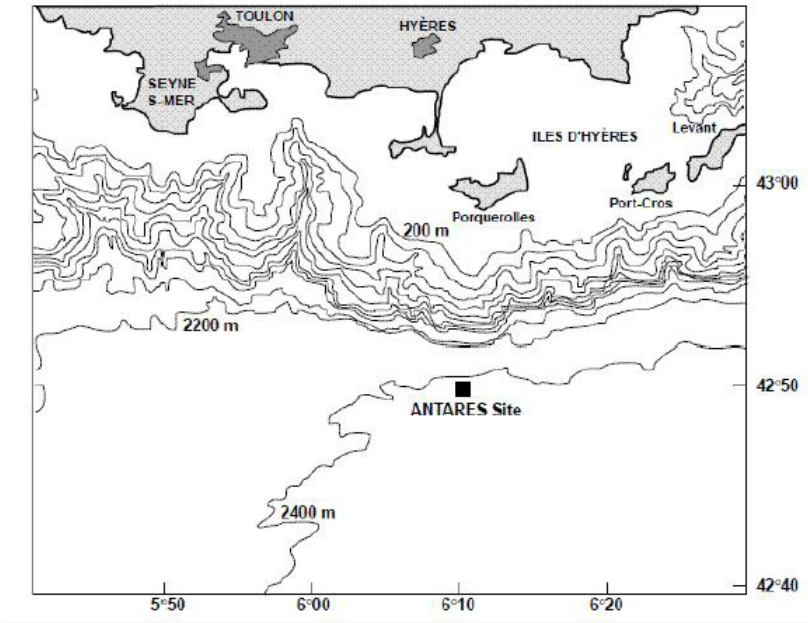

Figure 2.10. ANTARES geographical position, in terrestral latitude (y-axis) and longitude (x-axis): its coordinates are 42° 48'N, 6° 10'E

(PMT) and the electronics for its working and for signal transmission. Light attenuation from the sphere, whose refraction index is $n_{sph} = 1.47$, is less then 5% for wavelengths $\lambda > 350$ nm. To minimize light losses and also to achieve a better coupling between the sphere and the PMT photo-cathode an optical gel is used: its attenuation length is 60 cm, its refraction index is $n_{gel} = 1.40$ in correspondence of the blue wavelength ($\lambda \sim 470$nm) so that $n_{water} < n_{gel} < n_{sph}$.

The Earth magnetic field in ANTARES site is about 46 μT and has non negligible effects on photo-tube efficiency, because of the bending influence on photo-electrons. In order to avoid a dependency of PMTs signal on their orientation with respect to the Earth magnetic field, a high permittivity μ-metal cage is inserted so that the OM is magnetically shielded. The shielding is more efficient with a widther grid; at the same time a decreasing in light collec-

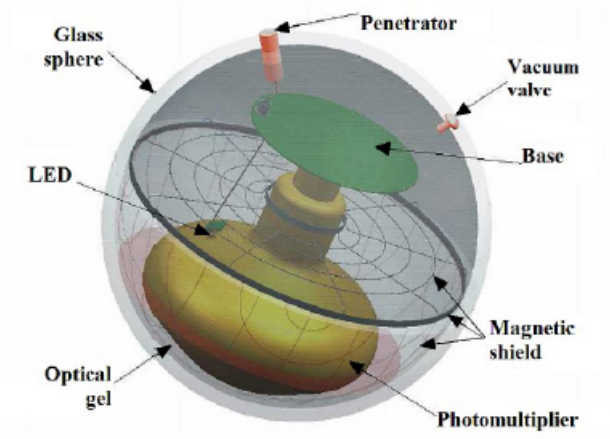

Figure 2.11. A schematic picture of an ANTARES Optical Module.

tion has to be accounted for because of the grid. The compromise chosen by the ANTARES Collaboration consists of a grid width of 681 mm, with less than 4% of the photo-cathode surface covered and a shielding from the magnetic field of a factor of three.
Hamamatsu R7081-20 PMT contains 14 amplification steps and a nominal gain of 5 $\times 10^7$ at about 1750 V. The PMT is responsive to photons in [300;600] nm. Its peak quantum efficiency is 23% at wavelengths in [350;450] nm, as shown in Figure 2.20: this range corresponds to the blue part of the visible spectrum, where also the water transparency is maximum. Charge resolution on a single photo-electron is about 40% and the Transit Time Spread (TTS) is about 1.5 ns (full width at half maximum). The dark count rate at the 0.25 photo-electron level is about 2 kHz. The high voltage is supplied by a Cockroft-Walton DC/DC converter (12/1750 V), located on an electronic card at the base of the PMT. This card also contains a Light Emitting Diode (LED) calibration system. The sphere surface, behind the PMT, is black painted and contains a penetrator that allows the linkage for data transmission and the delivery of high voltage.

OMs are grouped in storeys or floors of three OMs each, connected through an electro-mechanical cable. The three OMs are geometrically placed at the vertex of an equilateral triangle, perpendicular to a titanium structure called Optical Module Frame (OMF): it houses also offshore electronics and processors. Because the detector is optimised in search for up-going neutrinos, the three OMs point toward the bottom of the sea, at 45° with respect to the vertical, as is shown in Figure 2.12.

Considering the high angular acceptance (±70° from the PMT axis), the proposed placement allows to reveal light from the Southern Hemisphere with high efficiency, but also from directions not too much above the horizon. In the Southern Hemisphere there's a superposition in the angular acceptance of the three OMs, allowing to realize the trigger of an event thanks to coincidences. The relative position of the OMs is given in real time by a system of acoustic placement, that will be described later on.
Each storey contains a Local Control Module (LCM) with the electronics for the control and the acquisition of OMs data, positioned inside a titanium cylinder. A storey can contain also other instruments for measurements of the environmental properties and for calibrations, positioned on the OMF, as a LED (called Optical Beacon) or an acoustic hydrophone for neutrinos acoustic detection.
The distance between two adjacent floors is 14.5 m and the first storey of each line is located 100 m from the bottom of the sea, to leave enough space to allow for the development of

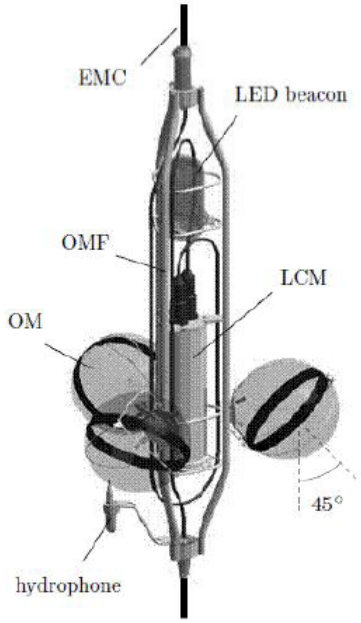

Figure 2.12. A schematic picture of an ANTARES storey.

the Cherenkov cone from up-going particles. The inter-line spacing varies between 65-70 m. Five floors linked constitute a sector, that is an individual unit in terms of power and data transmission. In each sector one of the five LCM is a Master LCM (MLCM) and its role is to handle data distribution between all LCMs in the sector. Five sectors together constitute a detector "string" or "line". A Dense Wavelength Division Multiplexer (DWDM) multiplexes the data signal from the five sectors onto one pair of optical fibres. Each string (see Figure 2.13) is fixed to the sea bottom through a dead weight and the Bottom String Socket (BSS) that, a part from act as an anchor, allows the electric connection. On the opposite site, a buoy maintains the string as vertical as possible and is also helpful in the eventual recovery operations.

The BSS contains the String Control Module (SCM), the String Power Module (SPM), some calibration instruments and a system of acoustic diffusion to recover the entire instrumented line. The SPM contains electronics for the supply of the five sectors of the line. The SCM contains electronics for the slow control.

The main part of the string is the Electro-Mechanical Cable (EMC): it allows the optical and electrical connection of the different elements with the transmission network. The ECM has to be either resistant, in order to sustain the pull to which the string is subject and assure its stability, and flexible, in order to permit the integration of various configurations, like manipulations, immersion and recovery. The EMC is about 480 m long and is composed by three smaller cables, each of which contains inside itself seven optical fibres, for a total of twenty-one optical fibres that transmit data collected from the OMs and from nine electrical copper cables, upholster of an insulating material, needed to supply power to different electronic components. Blank spaces inside the cable are occupied by silicone elements, to assure a greater stability of electrical and optical cables. The two external layers of the cable are made of aramid fibre (inside) and polyurethane (outside): in this way the cable is naturally protected, especially in the positioning and recovery phases.

The whole detector is made of 12 instrumented lines, in an octagonal configuration, and of a specific Instrumentation Line (IL), as is shown in Figures 2.14 and 2.15: the IL and the sector on the top of the twelfth are equipped with hydrophones and with instruments to monitor some environmental parameters.

Each BSS is connected to the Junction Box (JB): the JB allows the connection between the

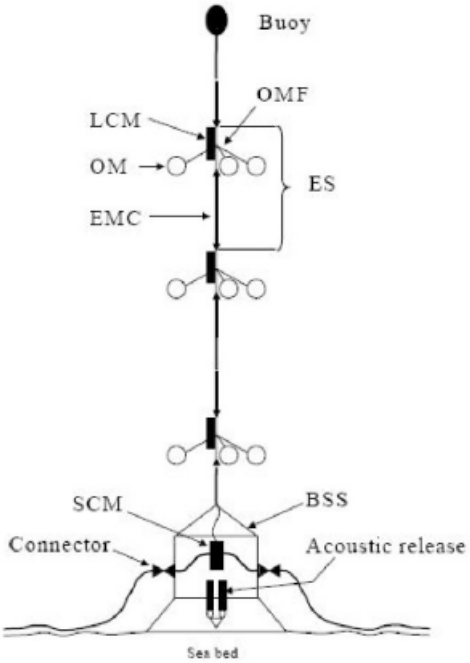

Figure 2.13. A scheme of an ANTARES string.

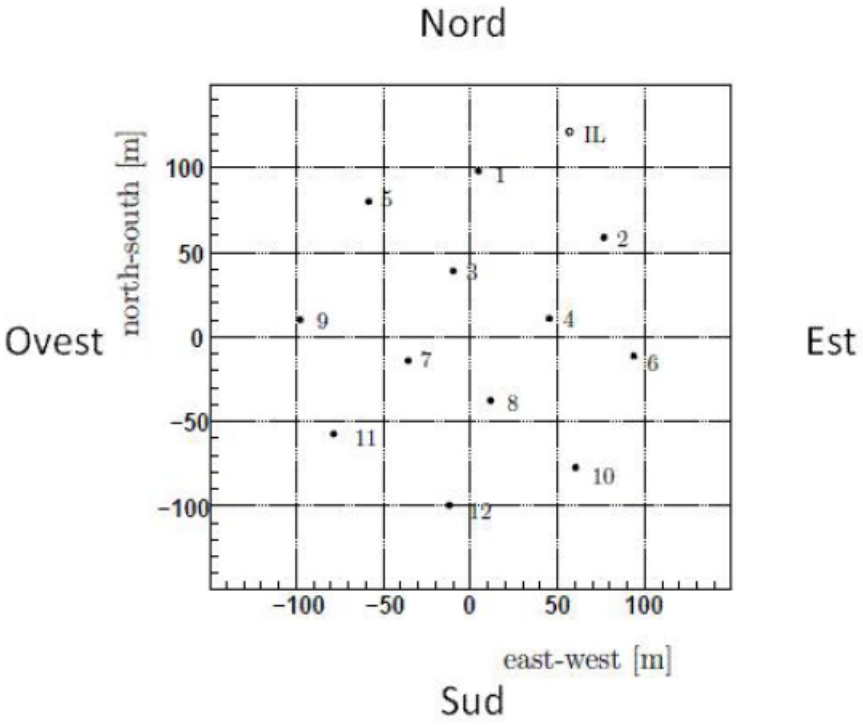

Figure 2.14. ANTARES detector top view: each point represents a string. The detector is composed of 12 strings and of an Instrumented Line.

detector and the shore station (at La Seyne sur Mer, France) where the ANTARES control room is located and data filtering is applied. Filtered data are copied and stored remotely at a computer centre in Lyon once a day. This shore connection is made through a 40 km long electro-optical cable, called Main Electro-Optical Cable (MEOC), and some interconnecting link cables (ILC).
Resuming, the ANTARES detector has 885 PMTs: indeed

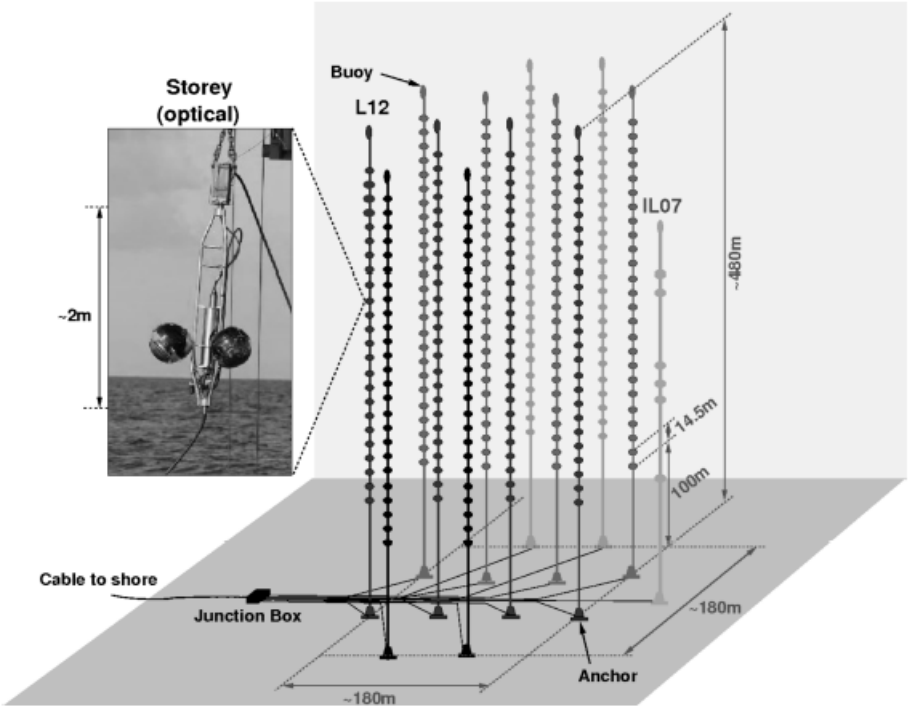

Figure 2.15. A schematic picture of the ANTARES detector.

(12 lines $\times$5 sectors/line $\times$5 floors/sector $\times$3 OMs/floor) - (5 floors$_{12th}$ $\times$3 OMs/floor) = 885
The instrumented volume is 1.1 $\times 10^7$ m^3.

2.3.1 The site

During the Research & Development phase of the experiment, extensive measurements were carried out in order to determine environmental and water optical properties (see [15]), that are extremely important parameters for particles' reconstruction algorithms.

Water optical properties

The performance of the detector depends on the optical properties of sea water, since light propagation in a medium is affected by absorption and scattering. Absorption reduces the amount of light that reaches the OMs, while scattering affects the path of the photons and their arrival time on the OMs. Both these phenomena are really important in the construction of an underwater telescope, since the light absorption defines the maximum distance between OMs to search for time coincidences of Cherenkov photons, while light scattering reduces the detector angular resolution.
Absorption and scattering reduce the intensity of light as

$$I(x,\lambda) = I_0(\lambda) e^{x/\lambda_{\rm abs}(\lambda)} e^{x/\lambda_s^{\rm eff}(\lambda)}$$

where x is the optical path travelled by light, $\lambda_{\rm abs}$ is the absorption length, defined as the distance after which a fraction 1/e of photon survives to the absorption, and $\lambda_{\rm s}^{\rm eff}$ is the effective scattering length. Since scattering depends not only on the scattering length $\lambda_{\rm s}$, defined as the distance after which a fraction 1/e of photon is not scattered, but also on the scattering angle θ_s of a single process, this parameter can be summarized as

$$\lambda_{\rm s}^{\rm eff} = \frac{\lambda_{\rm s}}{1 - \langle \cos\theta_{\rm s} \rangle}$$

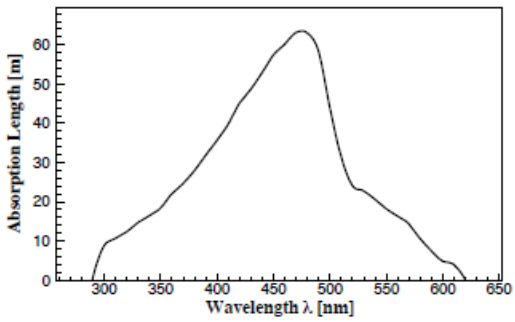

(a) Water absorption length as a function of the wavelength.

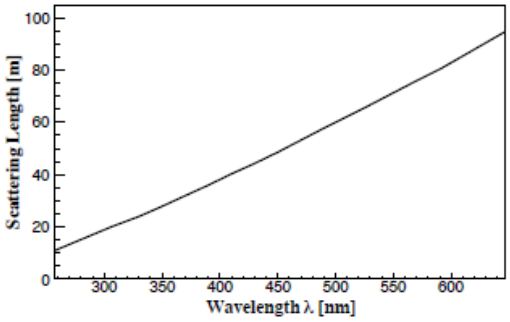

(b) Water scattering length as a function of the wavelength.

Figure 2.16. Water absorption and scattering lenghts.

Table 2.1. Light propagation parameters in Mediterranean water and South Pole ice.

	Mediterranean water $\lambda = 473(375)$ nm	South Pole ice $\lambda = 400$ nm
$\lambda_{\rm abs}$	$60 \pm 10\,(26 \pm 3)$ m	110 m
$\lambda_{\rm s}^{\rm eff}$	$270 \pm 30\,(120 \pm 10)$ m	20 m

where $\langle \cos\theta_{\rm s} \rangle$ is the medium cosine of the diffusion angle. The absorption and scattering lengths as a function of the photon wavelength are shown in Figure 2.16. Values for absorption and effective scattering lengths in the Mediterranean waters and in the South Pole ice are shown in Table 2.1.

Optical background

There are two background contributions to photon detection in sea water. The first one is the decay of the radioactive potassium isotope ^{40}K, according to

$$^{40}K \longrightarrow {}^{40}Ca + e^- + \overline{\nu}_e \text{ (BR=80.3\%)} \tag{2.4}$$

$$^{40}K + e^- \longrightarrow {}^{40}Ar + \nu_e + \gamma \text{ (BR=10.7\%)} \tag{2.5}$$

The emitted electron of Equation 2.4 can have an energy up to 1.33 MeV: therefore, a large fraction of the electrons so emitted is above the Cherenkov threshold for light production. At the same time, the photon emitted in the electron capture process of Equation 2.5 has an energy of 1460 keV: it can lead to Compton scattering producing electrons above the Cherenkov threshold.
Light pulses due to ^{40}K decay have a pulse height of the order of one photo-electron and are uncorrelated on a ns time scale, so they are typically rejected thanks to a trigger algorithm; eventually they can produce many photons in 1 ns so that a single PMT reaches the voltage threshold or coincidences on closer PMTs are generated.
The second optical background contribution comes from natural luminescence, called "bioluminescence", produced by various organisms whose intensity strictly depends on the deepness in sea water. Bioluminescence can give rise to optical background up to several orders of magnitude above the ^{40}K contribution: these bursts last for seconds.
In Figure 2.17 the typical counting rate on a PMT, i.e. hit frequency, as a function of time is illustrated. Two quantities describe this rate: the *baseline*, that is the continuous background component, and the *burst fraction*, that is the fraction of time during which the instantaneous background rate exceeds the baseline rate by at least 20%. Baseline rate is due to ^{40}K decay

and has a typical rate in the range [60;100] kHz; peak of biological activity can increase this rate up to some MHz.

After monitoring deep sea currents, it was found that the baseline component is correlated

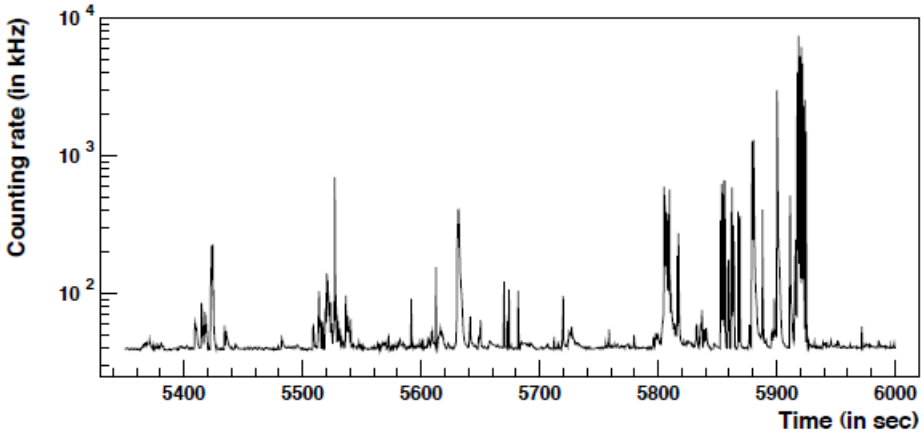

Figure 2.17. Typical ANTARES photomultiplier tube counting rate as a function of time. The almost flat background indicates the presence of potassium decay light while the bursts correspond to bioluminescence activity.

neither with the sea current nor with the burst frequency. However, long-term variations of the baseline were observed. Instead, strong correlation between bioluminescence and sea current velocity has been observed.

Sedimentation and biofouling

The optical modules are exposed to particle sedimentation and biofouling. This can adversely affect light transmission through the glass sphere of the optical module. Extensive in situ measurements have been performed in order to study this effect (see [18]). The average loss of light transmission is small, estimated to be only around 2% at the equator of the sphere housing the photomultiplier tube. Additionally it exhibits a tendency to saturate with time. Even though the sedimentation rate at the site can be quite high, these sediments are washed away by the sea currents, as shown in Figure 2.18, where light transmission as a function of time is illustrated.

2.3.2 Data acquisition

The role of the Data AcQuisition (DAQ) system of ANTARES is to convert the analogue signal recorded by the PM tubes into a digital format that can be used for physics analysis. This includes preparing the detector for data taking, converting the analogical PMT signal and transporting, filtering and storing the data. In addition, the run settings are archived. The DAQ system is a large network of processors, both on-shore and off-shore. The off-shore processors, integrated in custom made electronics, are connected to the on-shore processors (standard PC's) by the electro-optical cable on the sea bed. A schematic view of the data acquisition system is shown in Figure 2.19; for further details see [16].

Signal digitalization

A photon hitting the photo-cathode of a PMT can produce an electrical signal on the anode. The probability of an electron emission induced by a photon is given by the quantum efficiency (QE) of the PMT and is a function of the incident photon wavelength. The wavelength

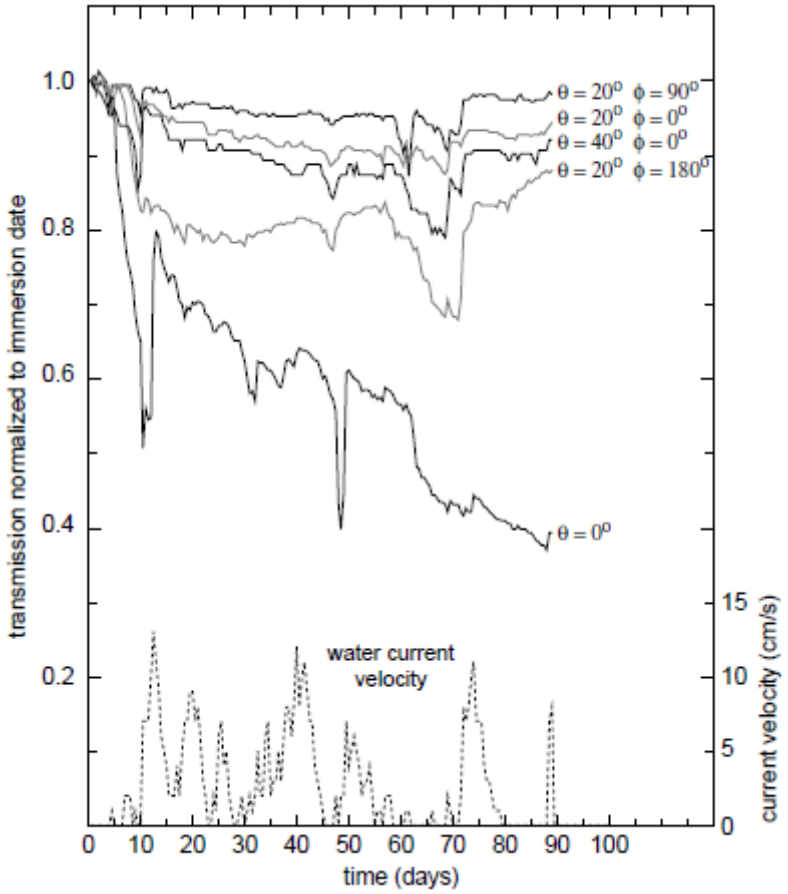

Figure 2.18. Light transmission as a function of time for vertically mounted spheres. The transmission is normalized to the transmission at the immersion date. The angles indicate the zenith θ and azimuth ϕ angles of the photo-diode. The θ=0 curve corresponds to the top of the sphere where the effect of sedimentation is largest. The increase in light transmission after a period of decreasing transmission is correlated with the sea current velocity indicating that sediments are washed away during high current velocity times. (Figure from [18]).

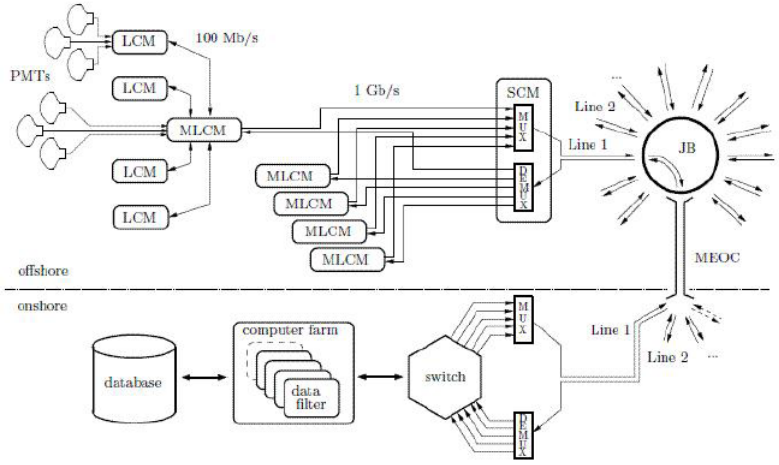

Figure 2.19. Flux diagram of data for a single string of the ANTARES detector.

dependence of the QE is shown in Figure 2.20.

If the signal amplitude exceeds a certain voltage threshold, the signal is read-out and digitized by a specific integrated circuit, the Analogue Ring Sampler (ARS). The threshold

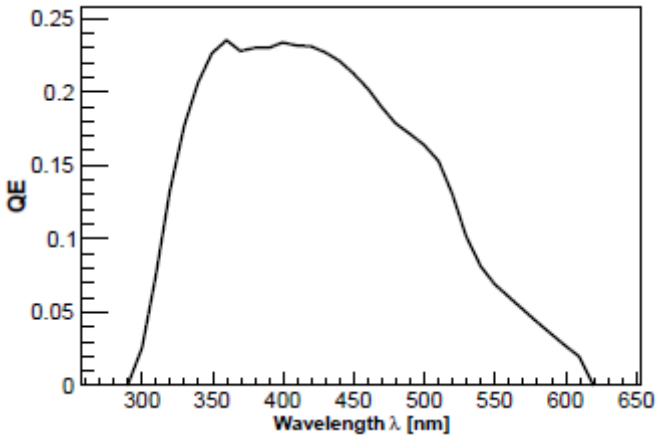

Figure 2.20. PMT quantum efficiency as a function of the incident light wavelength without taking into account the glass and gel surrounding the tube. The efficiency of the PMT peaks around 350 nm to 450 nm. The glass and gel of the optical module affect the light transmission in the lower end of the wavelength range, lowering the efficiency.

is set to a fraction of the mean amplitude of the signal generated by one photo-electron: it is typically set to 0.3 photo-electrons to suppress the PMT's dark current, although this can vary among different PMTs.
The ARS can distinguish between single photo-electron pulses (SPE) and more complex waveforms. The criteria used to discriminate the two classes are based on the amplitude of the signal, the time above threshold or the occurrence of multiple peaks within the time gate. Only charge and time information is recorded for SPE events. In cases of large or double pulses, the ARS can sample the PMT's signal continuously with a tunable sampling frequency of 150 MHz up to 1 GHz, holding the analog information on 128 switched capacitors. For physics data taking only SPE hits are used. A local clock is used by the ARS chips for the determination of the arrival time of the hit. The time resolution of the system is better than 0.4 ns. The charge of the analogical signal is integrated and digitized by the ARS over a certain period of time using two 8-bit Analogue to Digital Converters (ADC). The integration gate is typically set to 40 ns. After this period, the ARSs exhibit a dead time of around 200 ns. Each PMT is read by two ARSs operating in a token-ring scheme to minimize the effect of the dead time. The combined charge and time information is called a Level 0 (L0) hit. All 6 ARS chips in an LCM are read out by a Field Programmable Gate Array (FPGA) that arranges the hits produced in a time window into a dataframe and stores it in a 64MB Synchronous Dynamic Random Access Memory (SDRAM). The complete set of dataframes from all ARSs that correspond to the same time window is called a TimeSlice. A 20MHz clock is used to provide a common time for all ARSs. It is synchronized to the GPS time with an accuracy of 100 μs. Through the optical fiber network, all local clocks on the different storeys are synchronized with the master clock.

Data transmission

Each off-shore CPU runs two programs controlling the data transmission: **DaqHarness** handles the transfer of dataframes from the SDRAM to the control room, while **SCHarness** handles the transfer of calibration and monitoring data (slow-control data). Transmission Control Protocol and Internet Protocol (TCP/IP) are used for communication between the CPUs and for data transport. The LCMs in a sector are connected to the MLCM in the same sector using an optical bidirectional 100Mb/s link. These links are merged using the Ethernet switch of the MLCM into a single Gb/s Ethernet link. Each string is connected with an electro-optical cable to the junction box which in turn is connected to the shore station

with the 40 km long electro-optical cable. The data are transported using dense wavelength division multiplexing technique (DWDM). Each sector and each string use a unique pair of wavelengths to transmit data along a single optical fibre to shore. The **ControlHost** package is used for data transfer and communication among the processes in the DAQ system.

Data filtering and storage

All data, after the off-shore digitization, are transported to shore without any further selection. The total data output of the detector in periods of low bioluminescence (60-100 KHz per PMT) is 0.3-0.5 GB/s. Since most of it is optical background it has to be filtered appropriately. Trigger algorithms are applied to identify signals from particles traversing the detector by searching for space-time correlations in the data. Such physics events selected by the **DataFilter** program, are subsequently written to disk with the program **DataWriter**. The DataFilter looks for a set of correlated hits in the full detector in a window of about 4 μs. If an event is found, all hits during this time window are stored. If ANTARES receives external GRB alerts all detector activity is recorded for a few minutes. Data filtering is examined in more detail in the following section.

2.3.3 Triggers

As was previously stated, the majority of the stored data is optical background due to potassium decays and bioluminescence. This overwhelming background can be reduced by a factor of 10^4 on the first filtering (triggering) stage (see [38]). Such a reduction is achieved by searching for hits within 20 ns in different PMTs of the same storey or single hits with an amplitude higher than 3 photo-electrons. Hits satisfying these criteria are called L1 hits. All other hits are called L0. This kind of selection is based on the assumption that background hits should be uncorrelated and signal hits correlated. Two recorded hits on two different PMTs are considered causally related if they satisfy the following relation

$$|\Delta t| \leq \frac{n}{c} d$$

where Δt is the time difference between hits, d is the distance between the PMTs and $v_g = n/c$ is the group velocity of light in water. In this time window an additional ± 20 ns is included to allow for uncertainties in the hit positions, time and light scattering. Hits satisfying this condition constitute a cluster.
If this cluster is large enough (typically 5 L1 hits) it is stored as a physics event. Physics events contain L1 hits that fired the trigger as well as all L0 hits in $\pm 2.2\,\mu$s from the first and last L1 hit. The reason for this is that this is the time it takes for a relativistic muon to travel approximately 650 m, i.e. traverse the detector.
In addition to this first level selection, a second trigger level (e.g. 3N or T3 triggers) can be applied. This includes a scan over a certain number of directions searching for coincidences compatible with the Cherenkov light emission hypothesis. Additional clusters can be formed by L1 hits. An example of this are the T2 and T3 trigger: a T2 cluster is defined as two L1 hits in adjacent floors and a T3 cluster is defined as two L1 hits in adjacent floors or next-to-adjacent floors. The time windows are 100 ns and 200 ns, respectively. T3 triggers accepts more background hits, increasing the sensitivity in the low energy region with the drawback of triggering on additional events that will be reconstructed badly, i.e. it exhibits a higher efficiency at the expense of lower purity. Multiple T-hits within the maximum event time are required to reduce the background further. This trigger clusterization is shown in Figure 2.21. For further details see [23].

At the moment, according to the scope of the analysis, six different trigger configurations are used:

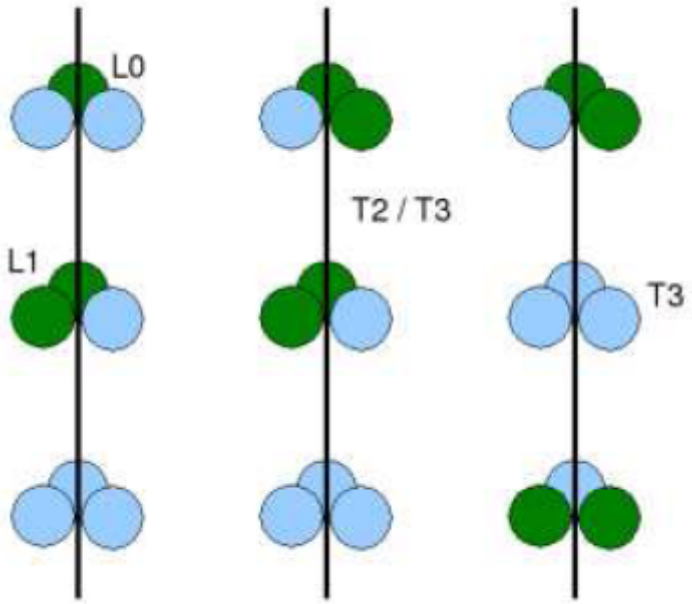

Figure 2.21. Schematic view of the ANTARES trigger system. Each floor consists of three PMTs represented by spheres. The hits are represented by dark colored spheres. The left plot has one L0 and one L1 hit. The middle plot has two L1 hits which make together a T2 or T3 hit. The right plot has two L1 hits making a T3 hit.

- 3N or 3D_SCAN: requires at least 5 L1 in a time window of 2.2 μs;
- T3 (2T3): requires at least 1 (2) T3;
- GC: requires 1 L0 and 4 L1 in the Galactic Centre direction, in order to maximize the detection efficiency of neutrinos coming from there;
- Minimum Bias: no filter are applied to check for data quality (registration of 4 ms every second);
- K40: requires 2 L0 on two OMs of the same storey in a time window of 50 ns (used for the in situ calibration);
- Transit Sources Trigger (TST): is activated when a satellite, as *Fermi* or *Swift*, sends an advice. In this case 2 minutes of data are stored without any filtering.

Triggers are daily monitored: their rates can be seen in Figure 2.22.

2.3.4 Detector calibration

The precision of track and energy reconstruction is strongly dependent on the precision of time, position and charge measurements. In this section, the calibration systems used in ANTARES are discussed: in particular time, charge and position calibration. For further details see [73].

Time calibration

The time calibration in ANTARES is performed using pulses from LED and laser devices. A timing resolution on the recorded PMT signals of 1 ns is required to ensure the reliability of track and energy reconstruction. The internal clock calibration system measures the time

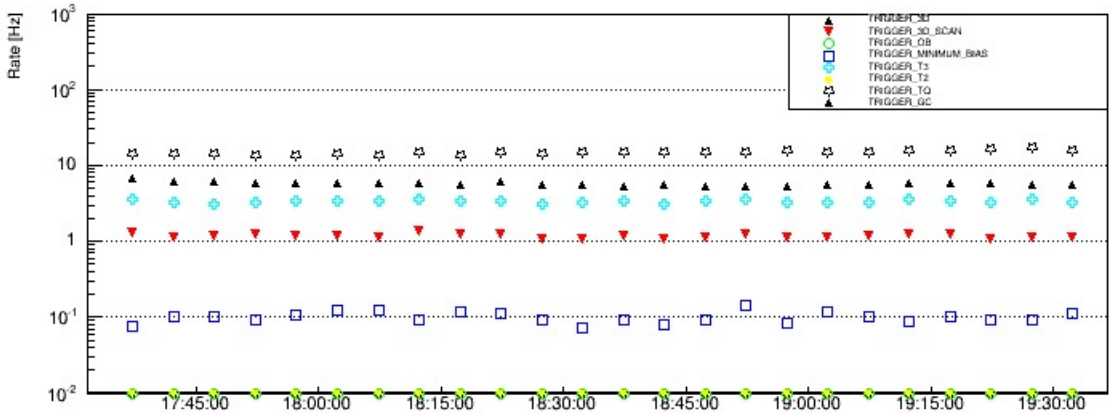

Figure 2.22. ANTARES trigger rates: black triangle is Galactic Centre and 3D trigger, red triangle is 3D_SCAN, green circle is DB trigger, blue square is minimum bias, light blue cross is T3, yellow is T2, star is TQ.

offsets of each storey. It consists of the master clock on-shore and a bi-directional optical communication system connected to all LCMs. The relative offset of each local clock can be measured by using a calibration signal sent by the master clock and echoed back. The clock system assigns an absolute event time with a GPS master clock synchronization accuracy of 100 μs. The optical beacon system is used to calibrate the relative offsets between the PMTs. Four blue (472 nm) LED beacons on storeys 2, 9, 15 and 21 of each detector line and two green (592 nm) laser beacons on the BSS of L7 and L8 are used for this purpose. The LED beacons are used for intra-line calibration purposes while the laser beacon, being much more powerful and able to illuminate all the lines, is used for inter-line calibration. An initial set of time offsets is determined in the laboratory prior to deployment. After deployment, these values may change due to different factors such as temperature changes or stresses in the cables. Using the optical beacon system they are monitored periodically and readjusted as necessary. A second calibration system consisting of a blue (470 nm) LED inside each OM is used to measure time offsets between the PMT photo-cathode and the read-out electronics. Internal LED and optical beacon measurements reveal less than 0.5 ns contribution of the electronics to the photon arrival time resolution. Thus, time resolution is dominated by the transit time spread of the PMTs (which is about 1.5 ns), by light scattering and by chromatic dispersion, which depends on the distance travelled by the photon. The calibration system just described provides a relative time calibration better than 1 ns.

Charge calibration

The integrated charge of the PMT signal has to be converted into the number of photo-electrons that created the pulse. The relation between the signal amplitude and the number of photo-electrons is given by the transfer function of the Amplitude-to-Voltage Converter (AVC). This function is important for the measurement of the amplitude in the PMT pulse, as well as for the correction of the time slewing of the PMT signal i.e. the influence of the pulse amplitude and the pulse rise time on the threshold-crossing time, illustrated in Figure 2.23. The first step in charge calibration is performed on the test bench where the AVC transfer function is determined. In order to do this, a pulse generator sends a direct signal to a pair of ARS operating in a token-ring scheme. The pulse has a triangular shape with 4 ns rise time and 14 ns fall time. The transfer function and the dynamic range of the ADCs exhibit a linear behaviour and can be parametrized by the slope and intercept of the function. In addition to the test bench calibration, regular in situ calibration runs have to be performed. These runs are used to determine the pedestal value of the AVC channel, namely the offset AVC_{0pe} value corresponding to zero photo-electrons, and the single photo-electron peak which is studied

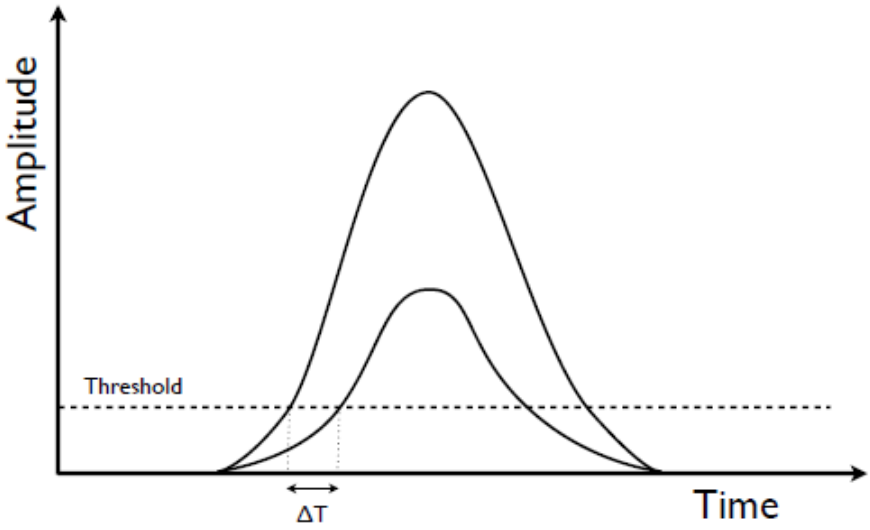

Figure 2.23. Illustration of the time slewing effect: differences in pulse shape and/or amplitude affect the threshold crossing time.

by looking at minimum bias events, since light from potassium decays and bioluminescence produce in their majority single photons on the photo-cathode level. The charge spectrum, ignoring contributions from the second and higher photo-electron peaks, can be described as

$$f(x) = Ae^{-a(x-x_{th})} + Be^{-\frac{(x-x_1)^2}{2\sigma^2}}$$

where the first term corresponds to the contribution of the dark current, while the second term describes the single photo-electron peak as a gaussian with mean x_1 and standard deviation σ. Measuring the pedestal and single photo-electron peak values, the transfer function can be determined.
Charge measurements in AVC channels appear to be affected by time measurements in the TVC channel. This is known as the "cross-talk effect" and can be attributed to a cross-talk of the capacitors inside the ARS pipeline. Plotting AVC against TVC values, as shown in Figure 2.24, makes it possible to determine the correction to be applied. After applying this correction most of the hits in a minimum bias event have a charge of one photo-electron.

Due to the spread of the PMT gain, the photo-electron peak is described by a gaussian function with mean AVC_{1pe}. If the parameters of the gaussian distribution for one photo-electron are μ_1 and σ_1, then for the coincidence of N photo-electrons the parameters of the gaussian distribution are $\mu_N = N\mu_1$ and $\sigma_N^2 = N\sigma_1^2$; then the transfer function is

$$Q[p.e.] = f(AVC) = \frac{AVC - AVC_{0pe}}{AVC_{1pe} - AVC_{0pe}}$$

where AVC is the corrected AVC value taking into account the cross-talk effect.
Light from potassium decay is also used to monitor how the detector response evolves with time. A gain drop of the PMTs is observed and is attributed to the aging of the photo-tube. The charge pedestal value is almost constant in time, while the photo-electron peak drops by around 0.02 photo-electrons per month. The systematic error on charge calibration is estimated at around 30%.

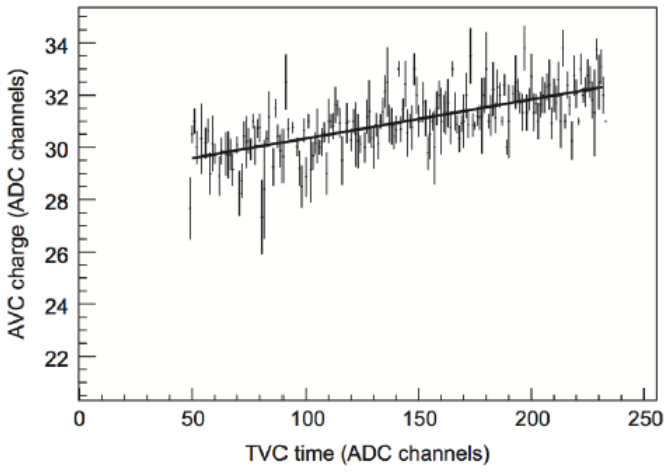

Figure 2.24. Illustration of the cross-talk affecting the charge measurement channel.

Position calibration

Due to the flexible nature of the lines, water currents can displace the position of the optical modules, especially on top storeys. As with timing and charge information, knowledge of the position of the optical modules is of high importance for a precise event reconstruction. For this purpose a High Frequency Long BaseLine (HFLBL) acoustic system is used to monitor the positions of five hydrophones along each line. The hydrophones are mounted on storeys 1, 8, 14, 20 and 25. A transmitter-receiver system is installed at the anchor of each line and some additional autonomous transponders are used. The emitters send high frequency acoustic signals in the 40-60 kHz range and the distances are obtained by measurements of the travel times of the acoustic waves. The distances are used to triangulate the position of each receiver with respect to the emitters on the sea floor. Furthermore, a system of compasses and tiltmetres is used to measure the orientation and inclination of each storey. The shape of each line is reconstructed by performing a global χ^2-fit based on a model of the mechanical behaviour of the line under the influence of the sea currents. The relative positions of each OM are calculated from this fit using the known geometry of each storey. In order to determine these positions as accurately as possible, knowledge of the water current flow and the sound velocity in sea water is used: Acoustic Doppler Current Profilers (ADCP) measure the water current flow, Conductivity-Temperature-Depth (CTD) sensors monitor the temperature and salinity of the water and sound velocimetres monitor the sound velocity in sea water. The relative positions of all the optical modules is monitored with an accuracy better than 20 cm. The movement of a line under the effect of sea currents is illustrated in Figure 2.25. The absolute positioning of each anchored detector component is calculated with an accuracy of about 1 m by acoustic triangulation from a surface ship equipped with differential GPS.

2.3.5 Detector history and status

During the period between 1996 and 1999 several site campaigns were performed, aiming to evaluate quantities such as the water refraction index, scattering and absorption lengths as well as background rates. A 350 m line with seven photomultipliers was deployed at a depth of 1200 m from the end of 1999 until June 2000. Tests of acoustic positioning as well as the first atmospheric muon data measurements were performed. The MEOC was installed in October of 2001. In December 2002, the junction box and a prototype sector-line (PSL) were deployed: it contained one LED beacon, a sound velocimetre, a pressure sensor,

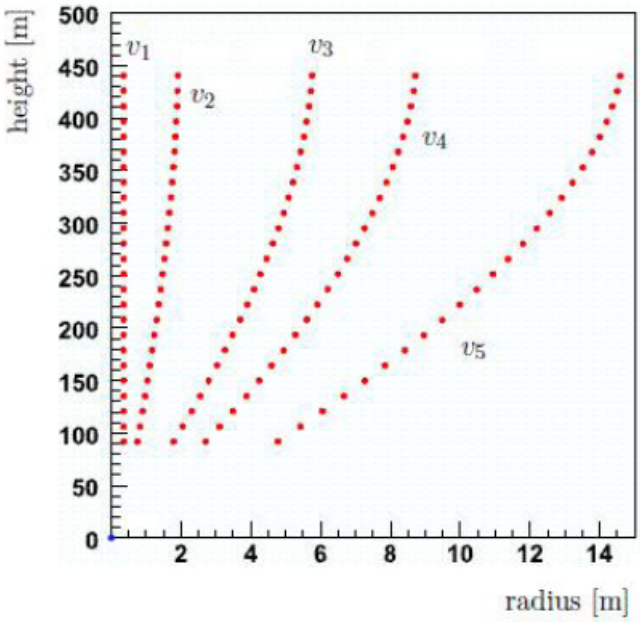

Figure 2.25. Reconstruction of an instrumented line under the effect of sea currents of different intensities: v1 = 0.01 cm/s; v2 = 7 cm/s; v3 = 12.6 cm/s; v4 = 16 cm/s; v5 = 20 cm/s.

hydrophones and an acoustic transceiver. A mini instrumentation line (MIL), containing time calibration, positioning and monitoring devices, was deployed in February 2003. During the next month, the prototype and the mini instrumentation line were connected to the junction box, where they stayed for the next couple of months. In March 2005, a mechanical test line (Line 0), containing all the mechanical elements of a full string but without the electronics, was built and deployed along with an improved mini instrumentation line (MILOM). The test line was recovered after two months. The first ANTARES complete line (Line 1) was deployed in February 2006 and in March of the same year it was connected and data taking started. In July 2006, Line 2 was deployed, becoming operational from September 2006. In January 2007, Lines 3,4 and 5 were connected, making ANTARES the most sensitive neutrino telescope in the Northern hemisphere. By the end of 2007, Lines 6 to 10 were connected, effectively doubling the size of ANTARES. The last two lines were connected in May 2008, thereby completing the construction of the ANTARES telescope. On June 24th 2008, the cable providing power to the junction box broke down, interrupting the detector's power supply. A sea operation took place on the 6th of September: the cable was repaired and data taking resumed normally. During the following years several lines have been non-operational and actions had to be taken for their recovery and redeployment.
The detector is in its last year of data-taking: ANTARES will be dismissed in 2016, leaving space for the future generation neutrino telescope: KM3NeT. It will be described in Chapter 6.

2.4 Event generation and reconstruction

As every experiment in Particle Physics, events are simulated at the calculator, both for signal and background: to simulate means to take into account all the relevant processes inside the detector as well as the detector's response. The present section shows the several stages of a simulation concerning events crossing the ANTARES environment: the Monte Carlo (MC) physics generators and the event reconstruction chain are illustrated. Then,

detector's performances are shown.

2.4.1 Monte Carlo physics generator

The interaction processes of primary particles with the atmosphere generate secondary charged particles. These particles are propagated throughout the detection media, until they reach the detector's sensitive volume. Afterwards, the emission, propagation and detection of Cherenkov light released by these particles crossing the detector are simulated. Finally, the transformation of photo-electrons into OM hits (i.e., the information of charge and arrival times) is performed.
Different codes are used depending on the particles to be simulated. Cosmic and atmospheric neutrinos and their interaction with the Earth are generated with GENerator of High-Energy Neutrino (GENHEN, v7r1 this thesis). Atmospheric muons are first simulated in the atmosphere by CORSIKA or MUPAGE (MUon GEnerator from PArametric formulas) and then propagated in sea water with MUSIC (MUon SImulation Code). The Cherenkov light released by the particles and by hadronic and electromagnetic showers are simulated through the KM3 package (v5r1 this thesis), that now incorporates the old GEASIM package for hadronic showers. Because the simulation has to account for variations in detector's and environmental conditions, it is performed Run By Run (RBR): TriggerEfficiency and Calibration codes (v3 this thesis) are then used for this purpose.
These codes work as described in the following:

- **GENHEN** (see [21]): it generates a flux of neutrino events in the proximity of the detector, that have a chance of producing a detectable signal. Neutrino events are generated isotropically inside a large cylinder around the detector. The size of this cylinder is determined in such a way that all neutrinos that are able to produce a detectable signal inside the detector will be simulated (for track-like events it is based on the maximum range that a muon can travel). A particle can be detected if it reaches the *can*, defined as the area surrounding the ANTARES instrumented volume extending typically up to 2-3 light attenuation lengths away;

- **MUPAGE** (see [34]): it simulates the atmospheric muon background, relying on the parametrization of the muon flux as a function of the muon energy and of the angular distribution on the surface of the can;

- **MUSIC** (see [20]): it simulates the propagation of the muon from the neutrino interaction vertex to the can. The energy losses of the muon as well as the changes on its direction due to multiple Coulomb scattering are included in the simulation;

- **KM3** (see [22]): it simulates all particles propagation inside the can and the light that reaches the optical modules. Since the tracking of every single photon emitted is computationally very inefficient, a set of tables is constructed: for muons, absorption and light scattering is taken into account, for particles other than muons only the attenuation of light is considered, while photon scattering is not simulated. The average photon yields produced for different distances, positions and orientations of the OMs with respect to the track or shower's axis direction are stored. The number and times of hits on the optical modules are then sampled from these tables. The effect of the OM angular acceptance and efficiency are included in this step;

- **TriggerEfficiency** (see [39]): it performs the simulation of the electronics response such as the charge integration and the dead time. In this step, optical background hits are added and the online triggers used in real data are simulated. Optical background hits are generated according to a Poisson distribution based on real measured rates in

order to reproduce the specific run's data taking conditions (RBR). The trigger logics that were used during the corresponding data run are finally applied.

2.4.2 Event topology

As was shown in Section 2.1, the result of neutrino interaction can be either a muon track or an electromagnetic/hadronic shower: even if the result is a track, muon energy losses generate showers, especially through Brehemsstralung and pair production. The first process consists in radiation emitted when a muon decelerates due to electromagnetic interactions with atoms from the medium; the second is the production, in presence of an atom, of an electron-positron pair.
In line of principle, ANTARES is able to identify all the three neutrinos family interacting via CC or NC. In this paragraph it will be described how these interactions are detected:

- ν_e: CC interactions produce electromagnetic and hadronic showers, whose longitudinal dimensions are some meters, considering that the radiation length ($\sim$ 36 cm) and the hadrons interaction length ($\sim$ 83 cm) in water are both less than 1 m. Because ANTARES is equipped with OMs on floors separated by about 15 m, these interactions appear to be point-like, reducing the angular resolution for these events. Above 100 GeV, if the interaction is inside the detector volume, the energy is completely released inside, allowing a good energy resolution. Because of the reduced spatial dimension, the background for these events is constituted by NC interactions of all neutrinos (ν_e, ν_μ, ν_τ);

- ν_μ: CC interactions produce a charged lepton, μ, and a localized hadronic shower. Neutrino energy is estimated from muon energy: in the channel $\nu_\mu + d \longrightarrow \mu^- + u$ we have $E_\mu \simeq \frac{1}{2}E_{\nu_\mu}$, while in $\overline{\nu}_\mu + u \longrightarrow \mu^+ + d$ we have $E_\mu \simeq \frac{2}{3}E_{\overline{\nu}_\mu}$. Muon energy is determined through its range if E_μ<100 GeV, because muon propagates less than 500 m in water so that its path is inside the detector; if instead E_μ>1 TeV muon energy is estimated using the energy loss per unit path (dE/dx). Further information on neutrino energy can be achieved if interaction (and consequently the hadronic shower) is inside the detector volume. This is the master channel for ANTARES;

- ν_τ: CC interactions produce a charged lepton, τ, and a hadronic shower. The τ can decay in the following channels:

$$\tau^- \longrightarrow \begin{cases} \mu^-\overline{\nu}_\mu\nu_\tau \\ e^-\overline{\nu}_e\nu_\tau \\ \pi^-\nu_\tau \\ \pi^-\pi^0\nu_\tau \\ \pi^-2\pi^0\nu_\tau \\ \pi^-3\pi^0\nu_\tau \\ \pi^-\pi^-\pi^+\nu_\tau \\ \pi^-\pi^+\pi^-\pi^0\nu_\tau \end{cases} \tag{2.6}$$

τ's decay length is $l = ct \sim 50(E_\tau/\text{PeV})$ m, so it can travel from a few meters to a few kilometres, according to its energy. Depending on whether the primary and decay showers are inside or outside the detector, the event topology will be different. The most striking signature is called "double bang", where both showers connected by a track are visible within the detector: it consists of shower+track+shower. Below 100 TeV, it is not possible to distinguish neutrino interaction vertex from τ decay vertex: so, the spatial distribution of the electronic and semi-leptonic channel are very similar to that of ν_e CC and NC interaction. Muonic channel (BR $\sim$ 17.4%) is instead well visible, but similar to ν_μ CC.

- NC channel gives the same signature for all neutrino flavors and part of the energy is unobserved with the outgoing neutrino.

The shower development is topologically different from the track's one: it is not possible to reconstruct each cascade's particle that has been generated in the interaction. Moreover, as the shower develops in matter (at about the speed of light) energy is almost instantaneously deposited along the shower axis, producing a fast local heating of the medium and a density variation. The perturbation manifests as a bipolar pressure pulse (compression-thermal expansion-rarefaction), propagating in the medium at the speed of sound: this signal is at the base of the technique known as *neutrino acoustic detection*, that in ANTARES is carried on through the Autonomous Module for Acoustic DEtection Under the Sea (AMADEUS) project.
What especially has to be carefully accounted for is the fact that light from showers is not emitted under a fixed angle, as for tracks: the Cherenkov cone is distorted and the angular distribution of shower light emission

$$\frac{d^2P_*}{d\cos\theta d\phi} = c\exp[b(\cos\theta - \cos\theta_C)^\alpha]$$

needs to be taken into account. The values of the three parameters are $a = 0.35$, $b = -5.4$ and $c = (2\pi \times 0.06667)^{-1}$. The probability distribution of the angle of emission is shown in Figure 2.26: it is strongly peaked around the Cherenkov angle, indicating that the majority of the particles in the shower are directed parallel to the direction of the initial particle. The fact that for energies greater than 1 GeV the angular distribution is flat is due to the fact that multi-GeV particles rapidly split up into many secondary sub-GeV particles, with a negligible amount of Cherenkov light being emitted before this split-up has occurred. For

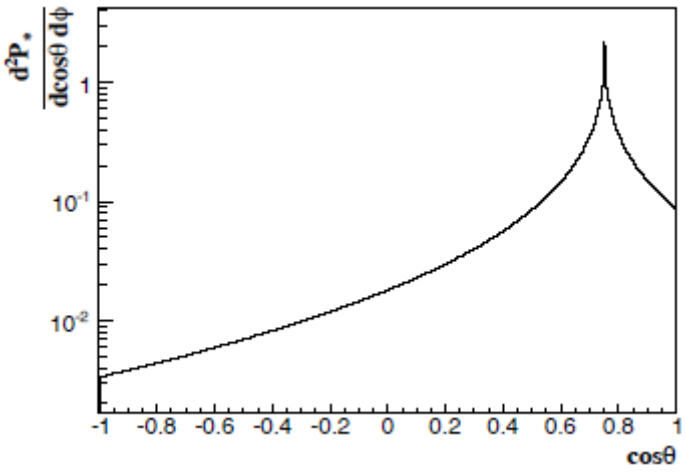

Figure 2.26. Angular distribution of light emitted by an electromagnetic shower.

further details on showers development and propagation, see [76].

This analysis is intended to detect neutrino signatures from track events; in order to take into account showers reconstructed as track events, also showers are simulated. Even if the phenomenology of showers and tracks is different, as can be seen in Figure 2.27, an event is always reconstructed through a track algorithm and a shower algorithm: then, according to the quality of the reconstruction, the event is classified as shower or as track. The ANTARES track reconstruction algorithms are presented in the next section.

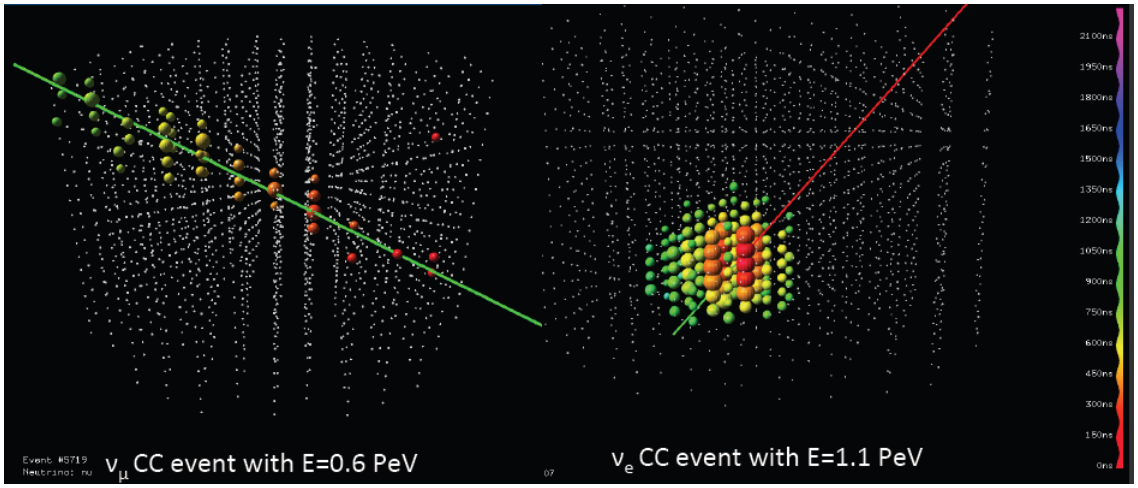

Figure 2.27. On the left, a high-energy MC track event; on the right, a high-energy MC shower event. Time information is color-coded.

2.4.3 Muon track reconstruction

Muon track can be approximated with a straight line if its energy is greater than 50 GeV: in this condition, its velocity can also be assumed to be equal to the vacuum light velocity. Having fixed a reference system (x,y,z), a muon track is completely determined once it is known the point $\vec{p} = (x_0,y_0,z_0)$ where the muon is at a time t_0 and the track cosine directors

$$\hat{d} = (\sin\theta\cos\phi, \sin\theta\sin\phi, \cos\theta)$$

with θ the zenith angle and ϕ the azimuth angle, as shown in Figure 2.28.
If $\vec{q_i}$=(x_i,y_i,z_i) is the position of the i-th PMT, the time of arrival of the photon on it is

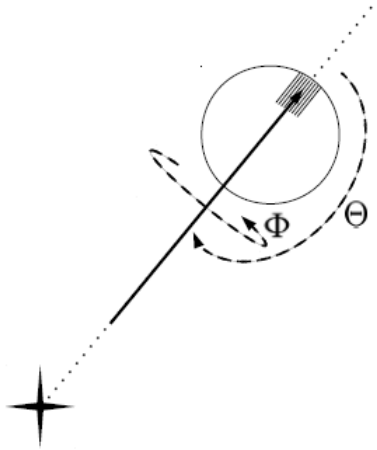

Figure 2.28. ANTARES zenith and azimuth definition.

$$t_i^{PMT} = t_0 + t_1 + t_2 \tag{2.7}$$

Referring to Figure 2.29, if O is the starting point of the track, $t_1 = |\vec{OA}|/c$ is the time in which muon reaches the emission point of Cherenkov light and $t_2 = |\vec{AB}|\, n/c$ is the propagation time of the photon from the emission point to the i-th PMT position.
Defining

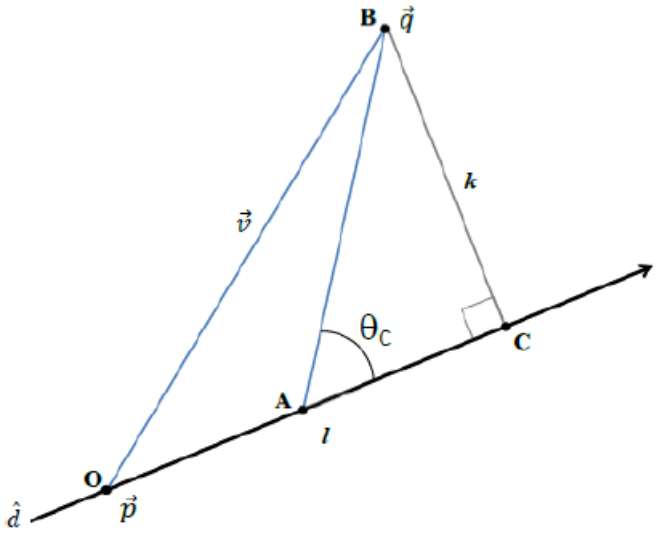

Figure 2.29. Picture of a muon track reconstruction: the arrow is the muon track, while θ_C is the Cherenkov emission angle.

$$\begin{aligned} \vec{v} &= \vec{q} - \vec{p} = \vec{OB} \\ |\vec{l}| &= \vec{q} \cdot \hat{d} = |\vec{OC}| \\ \vec{k} &= \sqrt{|\vec{OB}|^2 - |\vec{OC}|^2} \end{aligned} \tag{2.8}$$

the expected arrival time of the photon on the i-th PMT is

$$t_i = t_0 + \frac{1}{c}(l - \frac{k}{\tan\theta_C}) + \frac{1}{v_g}\frac{k}{\sin\theta_C} \tag{2.9}$$

For each quintuple (x_0,y_0,z_0,θ,ϕ), Equation 2.9 allows to determine the arrival time.
The ANTARES Collaboration has implemented two algorithms for track reconstruction: BBFit and AAFit.

BBFit
This is a fast algorithm based on the minimization of a function of the five parameters (x_0,y_0,z_0,θ,ϕ): the function is the Root Mean Square of the hits time residuals between theoretical and measured hits, as collected on the OMs. The minimizations allows the determination of the best set of track parameters.
The algorithm reconstructs with high efficiency the muon's direction: its angular resolution is of the order of one degree. The χ^2 function is shown in Figure 2.30, both for data and Monte Carlo simulated events.

AAFit
This is a better resolution algorithm, especially for high-energy up-going tracks. It is the one used in this analysis and in all searches of point-like sources. It consists of a recursive algorithm finalized to the maximization of the likelihood defined as the probability density function of the observed hits time residuals, as a function of the track parameters.
The AAfit reconstruction algorithm runs along six defined steps:

1. Pre-selection of hits: the interest is focused to reject as much amount of optical background hits as possible by using a predefined selection algorithm;

2. Linear pre-fit: it is a first linear fit independent of the starting point, it only uses a sub-sample of the pre-selected hits picked up from local coincidences (combination of 2

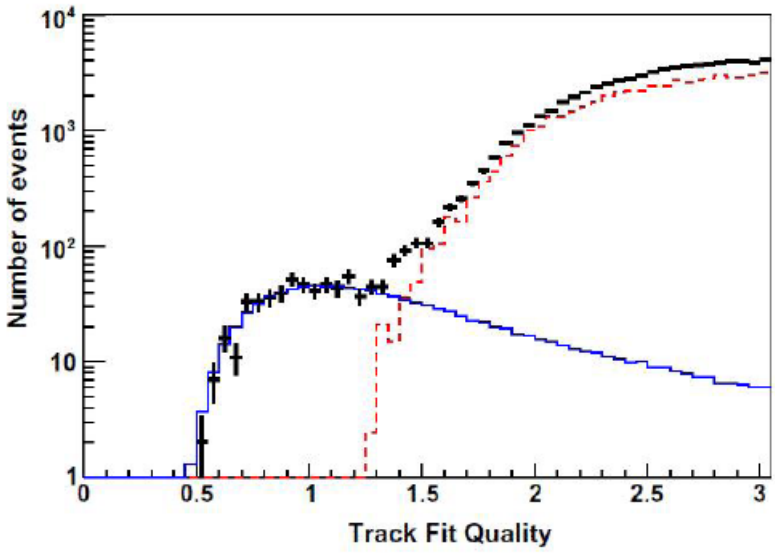

Figure 2.30. BBFit: χ^2 distribution for up-going tracks. Black are data, red are MC atmospheric down-going muons, blue are MC atmospheric neutrinos.

or more hits on one floor in 25 ns) and from hits with amplitudes typically larger than 3.0 photo-electrons;

3. M-estimator fit: the fit in this step uses the hits which are at distance shorter than 100 m to the initial fitted track and fall on a ±150 ns window with respect to the expected time calculated with the parameters of the linear pre-fit. This stage guarantees hits selection with amplitudes larger than 2.3 photo-electrons;

4. Maximum likelihood fit with the original Probability Density Function (PDF): here a maximum likelihood fit is done considering time residual from the main fit;

5. Repetition of steps 3 and 4 with different starting points: the steps 3 and 4 are re-done (9 times) since it improves the efficiency of the algorithm with different starting points concerning the linear pre-fit;

6. Maximum likelihood fit with improved PDF: the best result obtained in the previous step is used as new starting point for a maximum likelihood fit with an improved PDF. In this case, hits are selected with time residual in the [-250, 250] ns interval with amplitudes larger than 2.5 photo-electrons or found in local coincidences. The improved PDF is extracted from Monte Carlo simulations and includes the time residual, the incident angle, the photon path length and the background rate. Afterwards, it is maximized by using a maximum likelihood function $\mathcal{L}$ which includes the hits with small time residual with respect to the original PDF. For further details see [76].

The quality of reconstruction Λ can be estimated as the logarithm of the likelihood function $\mathcal{L}$ normalized to the track degrees of freedom $N_{\rm dof} = \mathrm{N_{hits}} - 5$:

$$\Lambda = \frac{log\mathcal{L}}{\mathrm{N_{dof}}} + 0.1(\mathrm{N_{comp}} - 1) \tag{2.10}$$

where $\mathrm{N_{comp}}$ represents the number of starting points (number of compatible solutions), result of the track estimation, compatible with the preferred result (i.e., which give the same track direction within 1°). The $\mathrm{N_{comp}}$ is also an indicator for rejection of mis-reconstructed tracks: for badly reconstructed events $\mathrm{N_{comp}} = 1$ in average, and can reach values up to 9 for well

reconstructed events (meaning that all of the starting points have resulted in the same track). Another important parameter that can be calculated through this algorithm is the angular uncertainty β on the reconstructed muon track: it is directly related to the uncertainties on azimuth and zenith through:

$$\beta = \sqrt{\sigma_\phi^2 \sin^2 \theta_{REC} + \sigma_\theta^2} \tag{2.11}$$

In Figure 2.31 the quality parameter Λ is shown for tracks reconstructed with AAFit as up-going with β<1°, both for data and simulated events. The lower panel displays the good data/MC agreement.

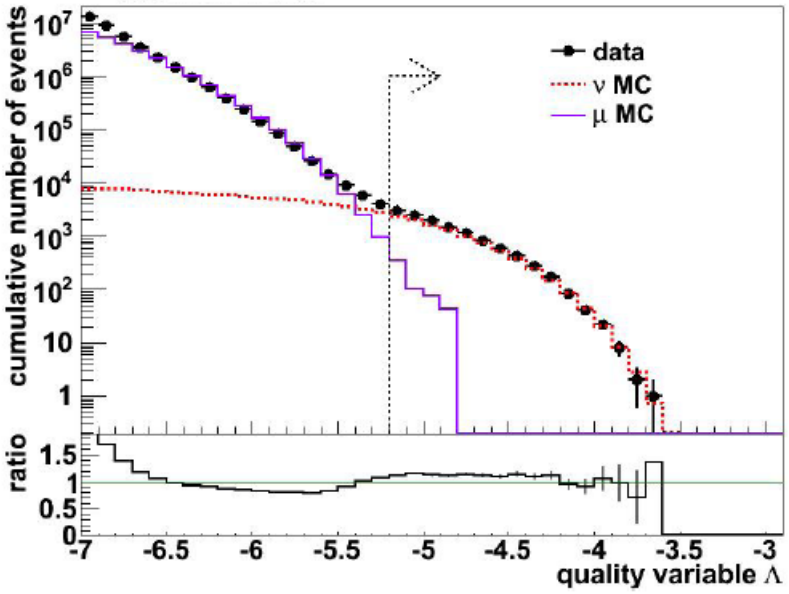

Figure 2.31. AAFit: Λ distribution for up-going tracks: red are MC atmospheric neutrinos, pink are MC atmospheric down-going muons, black are data. The arrow position indicates a cut on Λ in order to reduce the atmospheric contamination.

Event selection criteria based on Λ and β parameters can be used to improve the signal-to-noise ratio. To ensure solid directional reconstruction of the selected neutrino candidates, usual analyses require $\beta < 1°$. Additionally selecting simulated tracks with high reconstruction quality, most of the atmospheric muons that are falsely reconstructed as up-going are suppressed without significantly affecting the neutrino signal. The total background due to Cosmic Rays induced events can be therefore reduced up to factor 10^6 (see [10]).

2.5 Detector performances

The angular and energy resolution, summarized in the detector's effective area, are the most important parameters concerning the search for point sources of cosmic neutrinos. Therefore, a study of their magnitudes is necessary in order to determine the influence of physical processes and of the detector itself on the search.

2.5.1 Angular resolution

Angular uncertainty on neutrino direction is of huge importance in the neutrinos point-like sources search. Three main factor influence it:

1. emission angle of muon with respect to the incident neutrino;
2. muon deviation due to multiple scattering in water;
3. detector resolution on muon's track.

For the first two factors, the effect can be seen in Figure 2.32: the dependence of the average angle between the interacting neutrino and the reconstructed muon is described by the following empirical relation

$$\overline{\theta}_{\nu-\mu} = \frac{0.7^\circ}{(E_\nu/TeV)^{0.6}} \tag{2.12}$$

For $E = 1$ TeV, this angle is on average 0.7°; it decreases with increasing energy.
The detector resolution depends on the alignment between the different components, on the

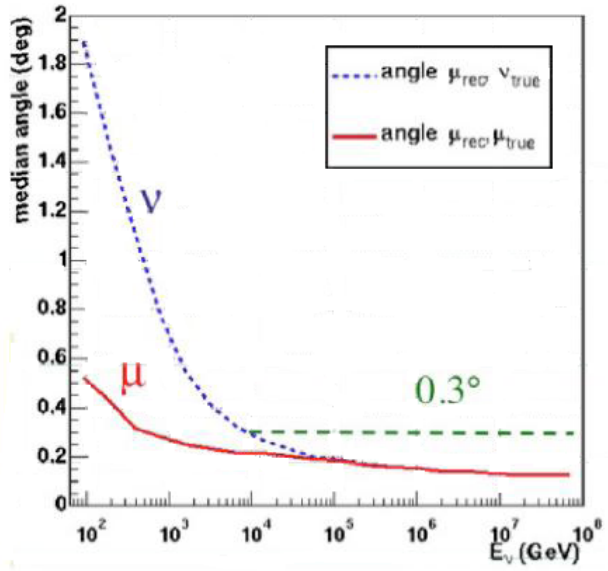

Figure 2.32. ANTARES angular resolution as a function of neutrino's energy: red solid line is the angle between the reconstructed muon and the MC generated muon, blue dotted line is the angle between the reconstructed muon and the incoming neutrino.

PMTs time resolution, on the global time of the read-out system and on the reconstruction quality of the muon tracks. In particular, the presence of Cherenkov radiation from secondary particles, propagating on different directions with respect to the muon's one, and of diffuse light tends to worsen the track reconstruction. MC simulations show that for E>10 TeV an angular resolution of 0.2° can be achieved, as Figure 2.32 shows.
Above 100 TeV, the angular resolution is completely dominated by detector's effects, that is uncertainty on track reconstruction, while below 10 TeV the kinematics of interaction dominates.

2.5.2 Energy resolution

Energy resolution is related to the energy fraction transferred to the muon, from muon energy losses outside the detector and from detector's experimental uncertainties. Different techniques for the energy estimation are required according to muon energy itself.
The most relevant energy-loss process for energies less than 1 TeV is ionization. When a muon scatters with atoms from the surrounding medium it transfers energy to atomic electrons. This process is described well by the Bethe-Bloch formula:

$$-\frac{dE}{dx} = \mathrm{Kz}^2 \frac{\mathrm{Z}}{\mathrm{A}} \frac{1}{\beta^2} \left[\frac{1}{2} \ln \frac{2\mathrm{m_e c}^2 \beta^2 \gamma^2 T_{\max}}{\mathrm{I}^2} - \beta^2 - \frac{\delta(\beta\gamma)}{2} \right] \tag{2.13}$$

where $K = 4\pi N_A r_e^2 m_e c^2$ is a constant, z is the charge of the incident particle, Z and A are respectively the atomic and mass number of the absorber, β is the velocity of the incident particle, γ is the Lorentz factor, I is the mean excitation potential of the atoms in the medium and $T_{\max}$ is the maximum kinetic energy which can be transferred to a free electron in a single collision. The potential I is related to the average orbital frequency of bound electron states in the atoms. The calculation of the mean excitation potential is a challenging task and its values for various absorption materials are deduced by energy-loss measurements. The value of I for water is 75 eV. The term δ corresponds to the density effect correction: it is included in order to take into account the effect of the polarization of the medium, induced by the passage of the charged particle, on the ionization energy loss. The mean energy-loss for positively charged muons in copper is shown in Figure 2.33.

The energy loss processes can be divided into continuous and stochastic. When the number of

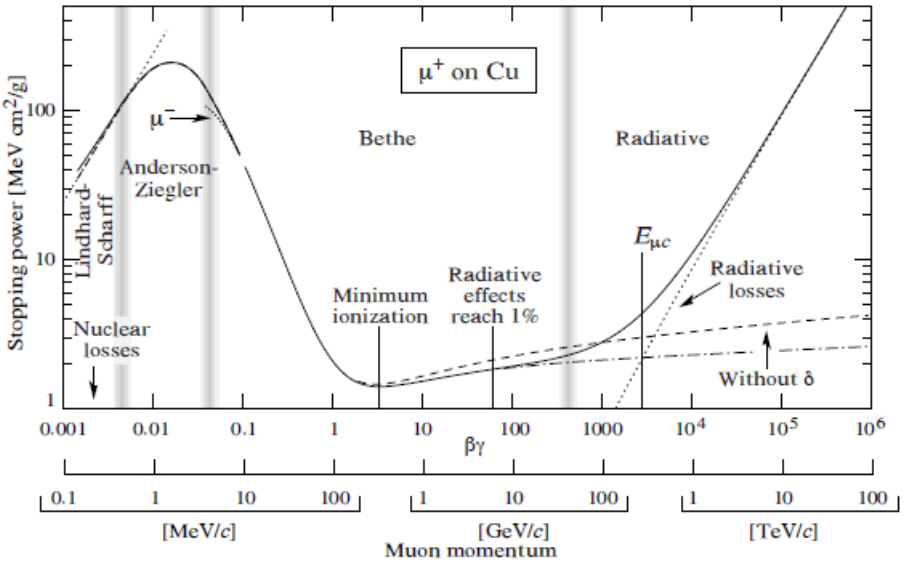

Figure 2.33. Stopping power for positively charged muons in copper. The Bethe-Bloch equation describes the central region of this figure, i.e. muon momenta from 5 MeV/c to 50 GeV/c.

discrete collisions over a macroscopic path length is very large and additionally each collision contributes a small fraction of the total energy loss, the process is considered continuous. On the other hand, stochastic processes occur rarely and a single instance can be responsible for a large fraction of the total energy loss leading to large energy loss fluctuations. Distinguishing between continuous and stochastic processes, the energy lost per unit length can be written as:

$$-\frac{dE}{dx} = a(E) + b(E)E$$

The first term is due to the ionization, a quasi continuous process, while the second term includes the contributions from stochastic processes. Between stochastic processes, the most important are Brehemsstralung and pair production, whose Feynmann diagrams are shown in Figure 2.34.

Below 100 GeV, muons are close to their minimum of ionization (thus are called Minimum Ionizing Particles or MIPs), that in water is dE/dx $\sim$ 2 MeV/cm, so range can be used to accurately measure the energy of fully contained events, that are events whose starting and ending point are measured inside the detector. Energy threshold for this method is about 10 GeV for vertical tracks, depending on the vertical distance between OMs groups, and 15 GeV for sloper tracks, depending on the horizontal distance between lines. Above 100 GeV,

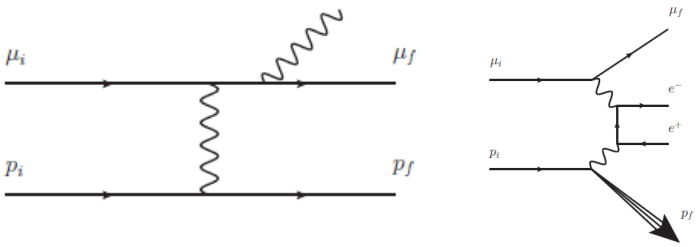

(a) Brehemsstralung Feynmann diagram.

(b) Pair production Feynmann diagram.

Figure 2.34. Feynmann diagrams of the most important energy loss mechanisms for high energy charged particles.

because of detector's dimensions, muon's range can be used to give just an estimation of the minimum energy.
For energies above 1 TeV, losses are dominated by stochastic processes, so that they become proportional to muon's energy. As Figure 2.35 shows, above 1 TeV muon's range increases logarithmically with energy. The challenge in reconstructing the muon energy lies in the fact

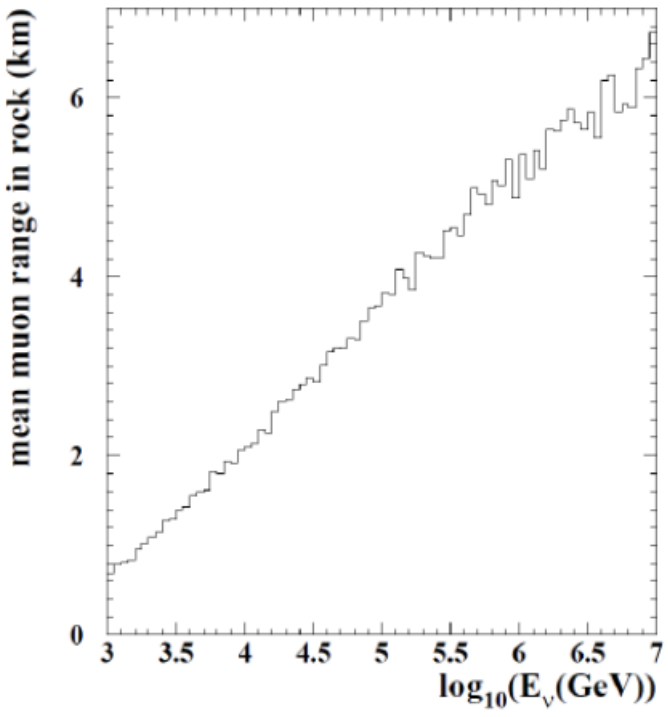

Figure 2.35. Muon range in standard rock as a function of the neutrino energy.

that for lower energies the light yield of the muon is almost constant, making it difficult to distinguish between e.g., a 100 GeV and a 500 GeV muon. In addition, light from potassium decay and bioluminescence contribute a significant amount of background light for such low energy events. For higher energies, the difficulty in reconstructing the muon energy arises from the stochastic nature of the energy-loss processes.
The ANTARES energy resolution is shown in Figure 2.36.

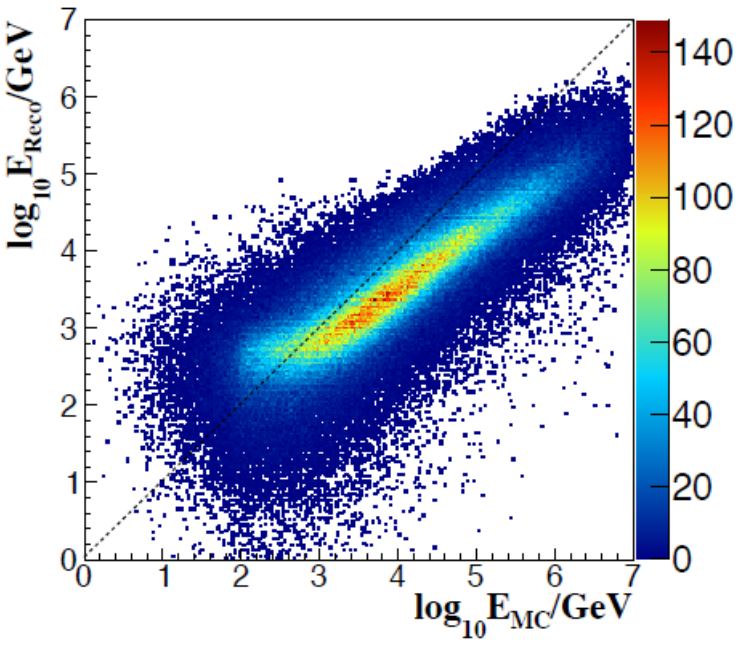

Figure 2.36. ANTARES energy resolution: on y-axis the logarithm of reconstructed energy, on x-axis the logarithm of true MC generated energy for an up-going muon neutrino sample. The dashed line is $E_{REC} = E_{MC}$.

2.5.3 Neutrino effective area

The instrument's efficiency to detect neutrinos of given energy and direction can be expressed in terms of the effective area A_{eff}. It can be considered the equivalent area of a 100% efficient detector and is defined as the ratio between the detected neutrino event rate R and the incident cosmic neutrino flux ϕ. The detection rate relates to the incoming neutrino flux at Earth as

$$R(E_\nu, \theta_\nu) = \phi(E_\nu) V_{\text{eff}}(E_\nu, \theta_\nu) \sigma(E_\nu) \rho N_A P_{\text{Earth}}(E_\nu, \theta_\nu)$$

where the detector's efficiency to detect the charged lepton is quantified by the effective volume V_{eff}, given by the ratio of the number of well-reconstructed signatures N_{sel} to the number of simulated neutrino interactions N_{gen} times the generation volume V_{gen}.
For a given neutrino energy E_ν with incident zenith angle θ_ν, the effective area is thus defined as:

$$A_{\text{eff}} = R(E_\nu, \theta_\nu)/\phi(E_\nu) = V_{\text{eff}}(E_\nu, \theta_\nu) \sigma(E_\nu) \rho N_A P_{\text{Earth}}(E_\nu, \theta_\nu)$$

To account for the probability that a neutrino interacts in the generated volume, each simulated event is weighted by the Earth transmission factor P_{Earth}, previously defined in Equation 2.3, and the probability for the interaction $\sigma(E_\nu)\rho N_A$. This is the so-called GENHEN's "generation weight" w_2, described in Equation A.1 of Appendix A: it also comprises the angular and energy phase space factors, I_θ and I_E, in which interactions have been simulated, and the generation volume V_{gen}.
Accordingly, the effective area can be calculated from the generation weight using Equation A.1:

$$A_{\text{eff}} = \frac{N_{\text{sel}}}{N_{\text{gen}}} w_2 \frac{1}{I_\theta} \frac{1}{I_E E^\gamma}$$

It is interesting to evaluate the effective area in certain declination bands, as it demonstrates the actual detection capability of the instrument for sources in different positions of the sky. Equivalently, the angular phase space factor I_θ, defined in Appendix A, transforms to account

for the number of simulated interactions in different declination bands. For an isotropic sky distribution, the angular phase space factor is given by the solid angle of the declination band $\Delta\delta$. I made use of the per-run Monte Carlo simulations corresponding to the data taken in 2013 (as described in Section 3.3) to derive the effective area. Since for each run an equal number of neutrino interactions N_{gen} had been generated, the different durations of the runs need to be accounted for by weighting each of them by its relative contribution to the total livetime of the data. Figure 2.37 shows the derived effective area for different declination bands, selecting up-going particle signatures (tracks and showers) reconstructed with AAFit, that fulfilled the reconstruction quality criteria $\Lambda > -5.5$ and $\beta < 1°$ and triggering the 3N or T3 flags. The rise with energy, a common feature of neutrino telescopes, is due not only to the increase of the neutrino-nucleon cross-section (Figure 2.3), but also to that of the muon range (in Figure 2.35), which can reach several kilometres at the highest energies. The ANTARES detector has best visibility for sources in the declination range of $-90°$ to $-45°$, while the other declination bands are less favourable.

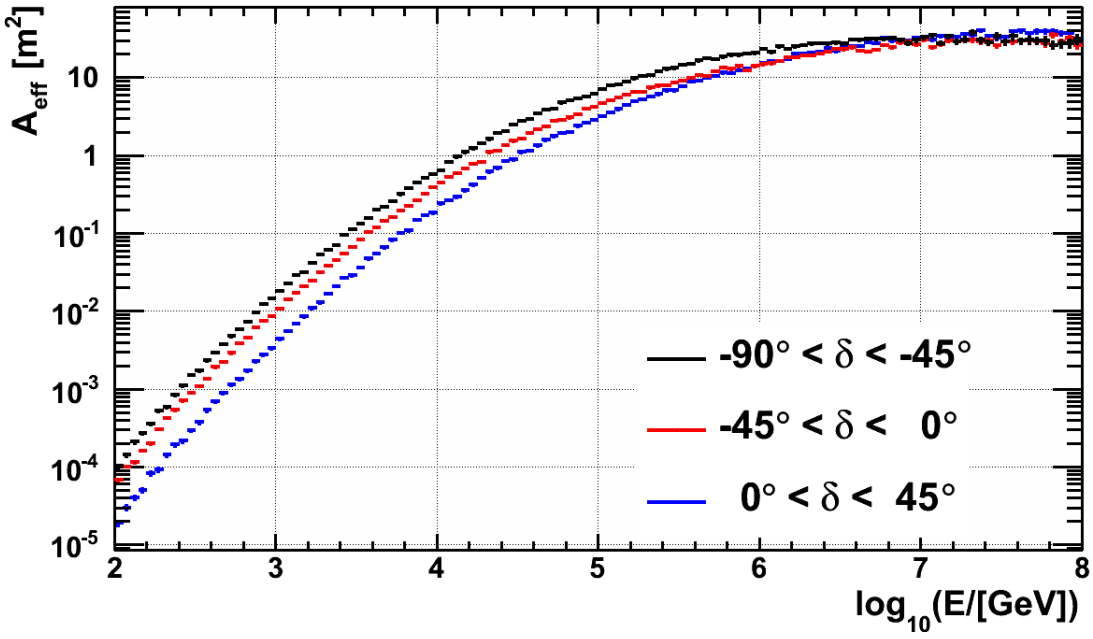

Figure 2.37. Time-averaged effective area of the ANTARES neutrino telescope as a function of energy for different declination bands δ with 2013 data. Typical triggers (3N or T3) and quality cuts ($\Lambda > -5.5$, $\beta < 1$ and $\theta > \pi/2$) are applied.

Chapter 3

Point-Like Sources Search

In this chapter I will present the search technique for prompt GRB neutrino emission. In particular the selection criteria for a bursts sample, occurred during 2012 and 2013 and collected from *Swift*, *Fermi* and *Konus-Wind* satellites, are illustrated: within this period, 120 bursts are candidate sources for a neutrino search in ANTARES. The entire sample of 120 GRBs is meant to be analysed in a future work, while in this thesis you'll find the described point-like search for the most promising GRB in the sample. Such source, called GRB130427A, results to be the most luminous since 1983. The analysis has been developed and then optimised for the fully numerical neutrino-emission model NeuCosmA (see Section 1.6). This chapter is structured as follows: in Section 3.1, the selection criteria from the whole sample are introduced; in Section 3.2, the general properties of the selected burst are described, as shown from different observatories. In Section 3.3, the set of ANTARES data in which signal and background have to be searched for is presented and in Section 3.4, an overview of the necessary statistical terms and tools that will be used through this work is given.

3.1 GRB selection

A reliable collection of GRB alert timings and positions in the sky is needed to define space and time windows to search for coincident neutrino signatures in the ANTARES data. In the following, I will present the consolidation of a GRB catalogue for the search and the simulation of expected neutrino fluxes from different tables provided by the *Swift*, *Fermi* and partly from *Konus-Wind* Collaborations. I will shortly describe the different catalogues, specifying how these are merged and how often burst parameters are taken from each of them. Finally, I will select the most intense burst from this catalogue for the final analysis.

3.1.1 GRB catalogues

Swift

The data sample of the *Swift* satellite[1] contains information from the three on-board instruments: the Burst Alert Telescope (BAT) for gamma rays, the X-Ray Telescope (XRT) for X-rays and the UltraViolet and Optic Telescope (UVOT) for UV and optical measurements, ordered with increasing position measurement accuracy Δ_{err}, from arcminutes to sub-arcseconds. BAT is a coded mask instrument, with a 2 sr field of view, whose spectral measurements are provided in the energy range from 15 to 150 keV; XRT is a Wolter I telescope, collecting X-Rays with a series of grating incidence concentric mirrors; the UVOT is a Ritchey-Chretien telescope with a filter wheel in seven wavelengths between 170 and 650 nm. Both XRT and UVOT have a common, but reduced, field of view with respect to BAT:

[1] *Swift*: `http://swift.gsfc.nasa.gov/docs/swift/archive/grb_table.html`

XRT sees a sky region of 24'×24', while UVOT sees 17'×17'. The instrument concept is such that BAT, having the wider field of view, as first detects the burst it sends an alert to XRT and UVOT, that in a time of about 90 s and 300 s respectively are re-positioned to watch the burst. Summing up the 2012 and 2013 periods of observations, the *Swift* table comprises 190 bursts.

Fermi
The FERMIGBRST catalogue[2] comprises information on bursts measured by the Glast Burst Monitor (GBM) instrument on-board *Fermi*. It is composed of 12 NaI and 2 BGO crystal scintillators, detecting photons in an energy range that goes from 10 keV to 1 MeV. The spectrum can be fitted with four different functions (in $\sim 13\%$ of cases no fit is given), whose functional forms are given in Equations 1.1, 1.3, 1.4 and 1.2: a single power-law (the best-fit model in $\sim 21\%$ of cases), a power-law with cut-off ($\sim 51\%$), a Band function ($\sim 9\%$) and a smoothly broken power-law ($\sim 6\%$). The large field of view of the instrument, which enables to detect around 1.5 bursts per day, comes at the expense of a rather poor angular resolution of the order of several degrees.
The other instrument on-board *Fermi* is the Large Area Telescope (LAT)[3]: it is a $e^+ e^-$ pair conversion telescope, made of a Si tracker ending in a calorimeter, with an Anti-Coincidence shield all around to assure that the incoming particle is a photon. It has a common but reduced field of view with respect to the GBM, around 2 sr, allowing a better resolution in the reconstruction of direction ($\sim$ 1 arcmin).
GBM and LAT catalogues comprise 452 GRBs, of which 57 are common with *Swift*.

Konus-Wind
Konus-Wind is a Russian spacecraft, whose primary goal is monitoring and studying the solar wind. For what concerns GRBs, an on-line *Konus-Wind* GRB catalogue in not available, so that information had to be manually taken from Gamma-ray bursts Coordinate Network (GCN) archive[4] only in case a burst or an information on it was missing in the previous catalogues: 6 more GRBs have been found. *Konus-Wind* spectra are in the energy range from 20 keV to 10 MeV.

3.1.2 Merged table

Tables from these three satellites are merged, so that a sample of 591 GRBs is obtained. When merging the Gamma-Ray Burst information, priorities are assigned to the values measured according to the following criteria:

- RA and DEC: right ascension and declination are chosen from the instrument with the smaller angular error, Δ_{err};
- F_γ: fluence is chosen from the satellite with wider spectral band;
- $E_{\rm min}$ and $E_{\rm max}$: minimum and maximum energies of the band in which fluence is measured follow the same selection of fluence; they are usually $E_{\rm min} = 0.015$ MeV and $E_{\rm max} = 0.150$ MeV for *Swift*, $E_{\rm min} = 0.01$ MeV and $E_{\rm max} = 1$ MeV for *Fermi*, $E_{\rm min} = 0.02$ MeV and $E_{\rm max} = 10$ MeV for *Konus-Wind*.
- α, β and E_γ: spectral parameters are chosen from the satellite with the wider spectral band, as the best fit model supplied;

[2] *Fermi* GBM: `http://heasarc.gsfc.nasa.gov/W3Browse/fermi/fermigbrst.html`
[3] *Fermi* LAT: `http://heasarc.gsfc.nasa.gov/W3Browse/fermi/fermilgrb.html`
[4] GCN: `http://gcn.gsfc.nasa.gov/gcn3_archive.html`

- T90: is the time in which 90% of the fluence is released and is assumed to be an estimation of the burst duration; it is chosen from the satellite with the wider spectral band;
- z: redshift is not measured by *Fermi* or *Konus-Wind*, only by *Swift* and ground-based detectors.

For the 591 GRBs, the usage of each catalogue as well as the priority assigned to each instrument are shown in Table 3.1. Because for a given GRB event some parameters could not be measured, default values have to be assumed: they are given in Table 3.2. There are reported the standard values to be assumed for the already presented α, β and E_γ, as well as values for other important parameters, such as the redshift z, the isotropic luminosity $L_{\rm iso}$, the variability time-scale $t_{\rm var}$, the Lorentz boost factor Γ, the fraction of jet energy in electrons e_E and in the magnetic field e_B, the baryonic loading f_P and the average fraction of proton energy transferred to a pion $\langle x_{p\to\pi}\rangle$. Last five quantities have always to be assumed: their default values are chosen according to the latest ANTARES GRBs analysis (see [79]). It is important to note that these input parameters might introduce uncertainties on the neutrino fluxes up to an order of magnitude.
Redshift default values are assigned to the bursts according to their duration: z=2.15 is assigned to long bursts and z=0.5 to short ones. This is related to statistical properties of the bursts: long GRBs are associated with the core-collapse of massive stars, so their host galaxies are star-forming regions, while short GRBs are associated with NS-NS merger, so they are found in early-type galaxies.
The isotropic luminosity $L_{\rm iso}$ is related to the duration T90 and to the total measured fluence in gamma-rays F_γ via the redshift z:

$$L_{\rm iso} = 4\pi d_L^2(z)\frac{F_\gamma}{T90} \tag{3.1}$$

where the luminosity distance d_L is a function of the redshift through the assumption of a cosmological model (ΛCDM in this thesis).
For what concerns the variability time scale $t_{\rm var}$, values can be found in [82], [50] and [51] for those GRBs whose light curves have been analysed. When it is not measured, default values are used: because short GRBs manifest an higher variability than long GRBs in their light curves, a $t_{\rm var} = 0.001$ s is assumed for them, while $t_{\rm var} = 0.01$ s is assumed for long GRBs. The variability time-scale is an important parameter: indeed, the very short variability of high energy photons coming from a cosmological source can carry key information about the structure of space-time, which can limit the possibility of having a breaking of the Lorentz Invariance as proposed by some theories ([17]).

From the resulting merged catalogue, some cuts have been applied, in order to assure that each burst was strongly constrained. For this reason, only GRBs satisfying the following conditions are considered:

1. T90 is measured;
2. spectrum is fitted (α is never assumed);
3. spectral fit is different from power law, since this kind of fit is typically the result of faint burst;
4. at least one quantity out of fluence and redshift is measured, in order to do not produce inconsistency with the assumed isotropic luminosity;
5. $\theta > \pi/2$, so that the burst is below ANTARES horizon;

Table 3.1. Usage of the *Swift*, *Fermi* and *Konus-Wind* catalogues for the 591 GRBs observed in the years 2012 and 2013. The numbers in square brackets give the assigned priority of each catalogue with respect to the parameters. Some parameters have not been measured from any instruments (last line), so that default values have to be assumed, except for T90.

Source	Position	Duration	Fluence	Spectrum	Redshift
Swift BAT	4%[4]	22%[3]	19%[3]	19%[3]	10%[1]
Swift XRT	16%[2]				
Swift UVOT	6%[1]				
Fermi GBM	68%[5]	76%[1]	77%[1]	69%[1]	
Fermi LAT	5%[3]				
Konus-Wind	1%[6]	1%[2]	4%[2]	4%[2]	
Missing		1%		8%	90%

Table 3.2. Standard GRB parameters, as described in the text: some values have always been assumed (Γ, $\langle x_{p\to\pi}\rangle$, f_P, e_E and e_B).

Default values	
$\alpha = -1$	$\beta = \alpha - 1$
$E_\gamma = 200$ keV	$F_\gamma = 10^{-5}$ erg/cm^2
$E_{\rm min}$=0.01 MeV	$E_{\rm max}$=10 MeV
$\Gamma = 316$	$\langle x_{p\to\pi}\rangle$=0.2
$f_P = 10$	$e_E = e_B = 0.1$
$z^{\rm LONG}$=2.15	$z^{\rm SHORT}$=0.5
$t_{\rm var}^{\rm LONG} = 0.01$ s	$t_{\rm var}^{\rm SHORT} = 0.001$ s
$L_{\rm iso}^{\rm LONG} = 10^{52}$ erg	$L_{\rm iso}^{\rm SHORT} = 10^{51}$ erg

6. the trigger time is in the validated ANTARES physics data to be analysed.

The sample of GRBs is composed of 120 candidate sources: they are listed in Table B.1 of Appendix B. Their distribution in the sky in equatorial coordinates with Aitoff projection is shown in Figure 3.1. The distributions of the selected parameters for the whole GRB sample (591 GRBs) and for the 120 selected sources are shown in Figure 3.2: the main features are

- the low energy photon spectral index α is distributed according to a gaussian, with mean value almost equal to -1;
- the high energy photon index β has a poorer distribution, because most of the sample is fitted with a cut-off power law, with a mean value nearly equal to -2;
- the break energy distribution peaks around 200 keV, that is the value used as standard, in case of missing measurement;
- the T90 distribution shows the two GRBs family (short and long), divided at 2 s;
- the photon fluence distribution extends from 10^{-8} to 10^{-3} erg/cm^2, with a mean value of about 10^{-5} erg/cm^2;
- the most far GRB of the sample is at z$\sim$6;
- the angular error distribution shows the different resolutions of *Swift*:UVOT, XRT, BAT and *Fermi*:GBM, LAT instruments.

As can be seen from the list in Table B.1 of Appendix B, the most promising source in terms of γ luminosity is GRB130427A (or 13042732 according to the *Fermi* Collaboration notation,

that is year, month, day and fraction of the day of the trigger time). For this reason, the goal of this thesis work is the search of neutrino events from GRB130427A; the rest of the sample will be analysed in a future work.

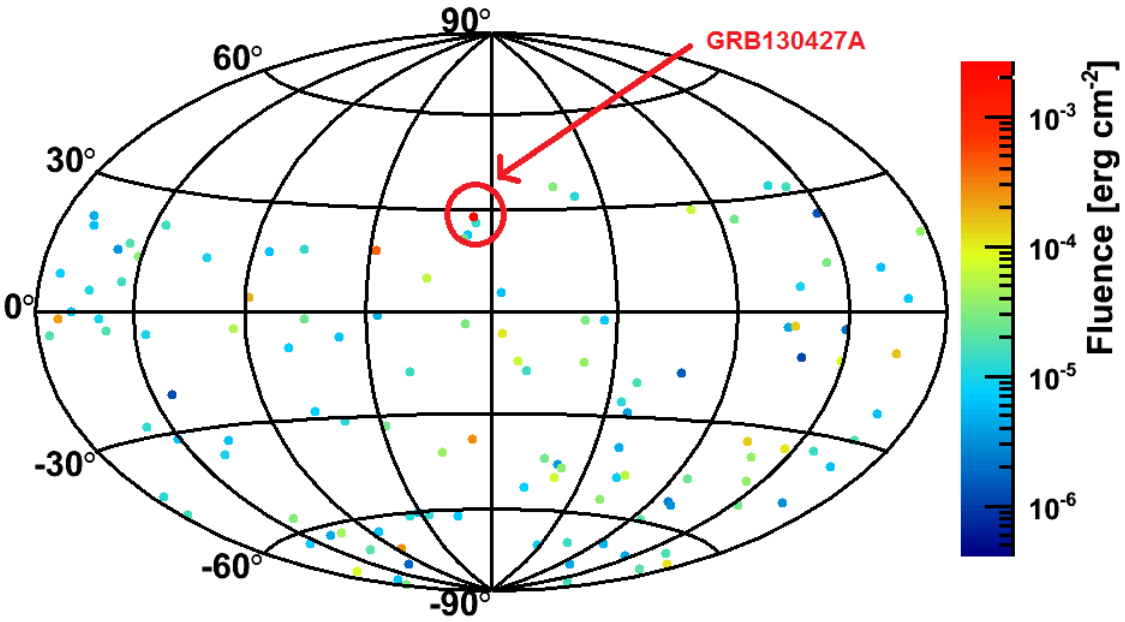

Figure 3.1. Distribution in the sky of the selected 120 sources: fluence is color-coded. Map is in equatorial coordinates RA and DEC, Aitoff projection. GRB130427A has coordinates RA=173.14°, DEC=27.71°.

3.2 GRB130427A: general properties

On April 27th, 2013 at 07:47:07 UT, one of the brightest gamma-ray bursts ever detected lighted up the high-energy sky. It could be observed by a record-setting number of satellites and ground-based telescopes[5]. With a measured photon fluence of the order of 10^{-3} erg/cm^2, GRB130427A turned out to be the strongest burst since 1983 (GRB830801B).
Numerous coincident and follow-up optical observations soon measured a redshift of only 0.34 (see [62]), which is exceptionally close for a Gamma-Ray Burst (see redshift distribution in Figure 3.2). Figure 3.3 shows the sky above 100 MeV as observed by the LAT instrument on-board the *Fermi* satellite at the trigger time and three hours before. GRB130427A significantly outshined the high energy sky with emission being visible for LAT almost the entire day. Two high-energy photons of a record-holding 95 GeV after 244 s and 32 GeV more than 9 hours after the onset of the prompt emission (see [91] and [9]) began to severely challenge prevailing models for the late GeV emission, yet might support scenarios of hadronic material within the ejecta. Such assumptions can only be tested beyond any doubt by the detection of simultaneously emitted neutrinos. Data of both operating neutrino telescopes IceCube and ANTARES could therefore hold valuable proof for the aforementioned models. However, the IceCube Collaboration had already announced the non-observation of any coincident neutrino signal in their data within ±1 day around the burst via the GCN network (see [29]). The ANTARES Collaboration performed a follow-up analysis during the prompt emission phase: no prominent high-energy signature or event multiplet was reported by the TAToO filters during ANTARES data acquisition (see [43]) within two days before and after the burst. ANTARES Collaboration already dedicated an off-line data analysis to this burst, taking

[5]see `http://gcn.gsfc.nasa.gov/other/130427A.gcn3` for GCN messages on GRB130427A

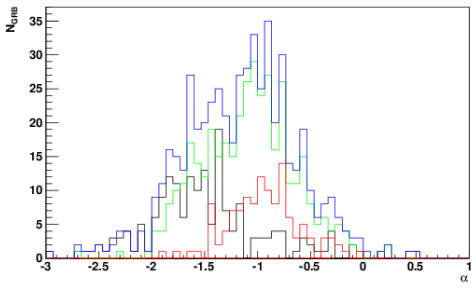

(a) First photon spectral index distribution.

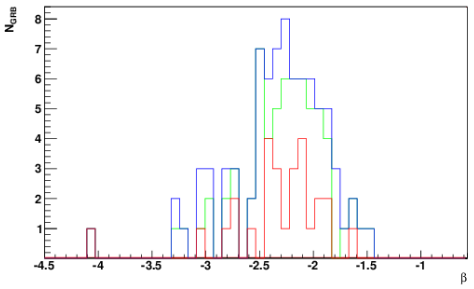

(b) Second photon spectral index distribution. *Swift* sample is missing because the only fit provided are PL and CPL.

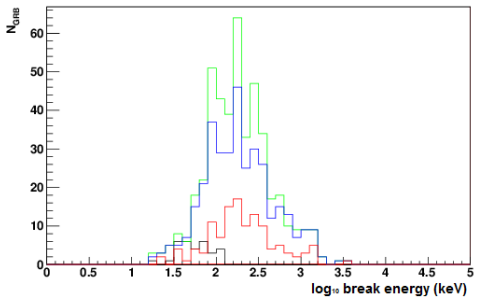

(c) Photon break energy distribution.

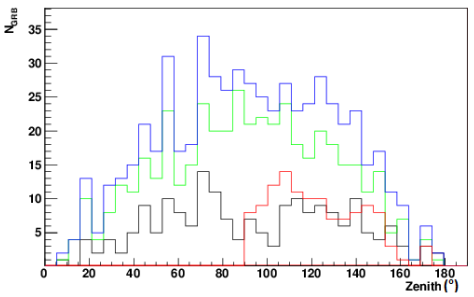

(d) Zenith distribution.

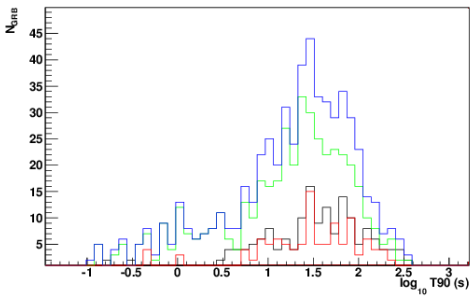

(e) Duration distribution.

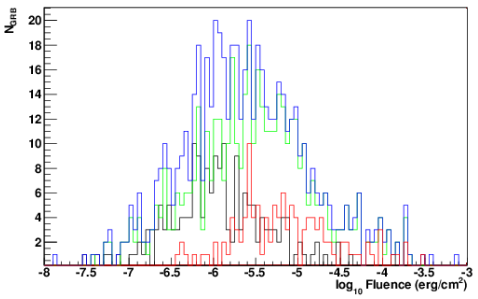

(f) Photon fluence distribution

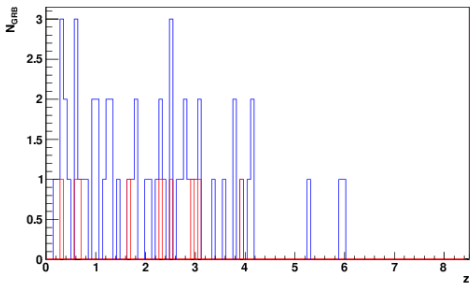

(g) Redshift distribution.

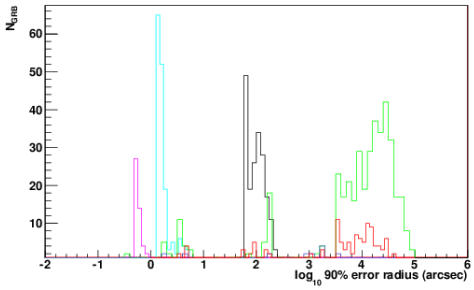

(h) Error box distribution: in black the *Swift*:BAT sample, in light blue the *Swift*:XRT sample, in pink the *Swift*:UVOT sample, in green the *Fermi*:GBM sample, in blue the *Fermi*:LAT sample, in red the selected sample (120 GRBs).

Figure 3.2. Distributions of α, β, E_γ, zenith, T90, F_γ, redshift and error box Δ_{err} in different catalogues. Colors convention is the following, where not otherwise written: in black the *Swift* sample (190 GRBs), in green the *Fermi* sample (452 GRBs), in blue the *Swift*+*Fermi*+*Konus-Wind* sample (591 GRBs), in red the selected sample (120 GRBs). Default values are not depicted here.

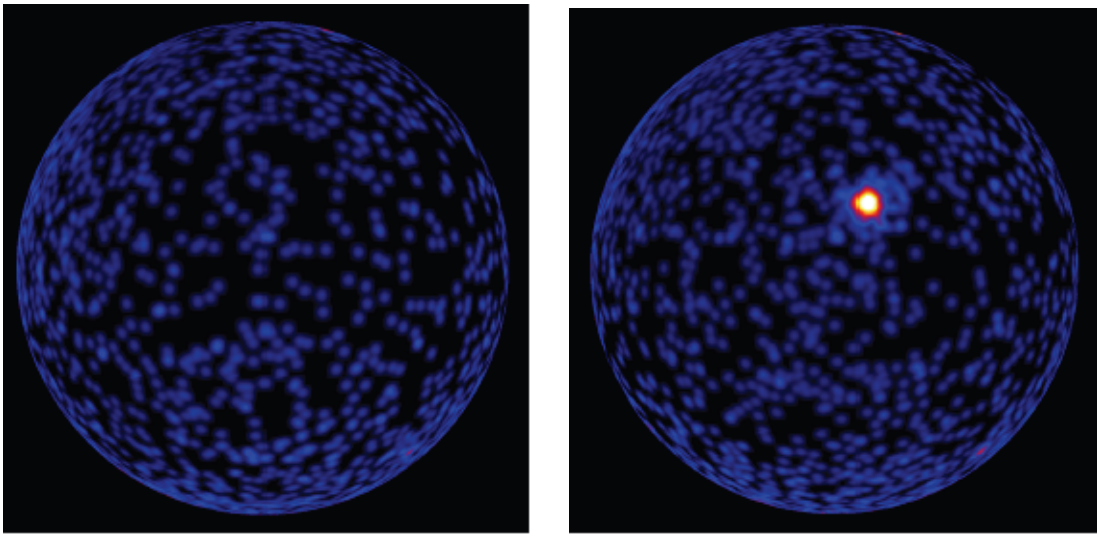

Figure 3.3. The sky as seen by *Fermi*:LAT three hours before the burst GRB130427A (left side) and when it occurred (right side), to give an impression of the burst's brightness with respect to the rest of the γ sky. (Credit: NASA/DOE/Fermi Collaboration).

into account the particular conditions at that time and optimizing data selection for the discovery of a neutrino signal as predicted by the numerical model NeuCosmA. Such analysis was using data from 2007 to 2011 to estimate the background contribution and default values for $t_{\rm var}$, Γ, f_P, e_E, e_E and $\langle x_{p\to\pi}\rangle$ to generate the expected NeuCosmA flux: no signal was found in coincidence with the γ emission (see [80]).
Since the last ANTARES analysis, the variability time of GRB130427A has been extracted from *Fermi* light curve, so that no assumption has to be made on it (the previous analysis assumed the default value $t_{\rm var} = 0.01$ s): it results to be $t_{\rm var} = 0.04 \pm 0.01$ s (see [82]). Therefore, the following analysis will assume the value of $t_{\rm var} = 0.04$ s. Moreover, this search is intended to optimise data selection in the light of a Time-Resolved search, which is expected to enhance the discovery potential of the assumed model.

DATA TAKING CONDITIONS
At the end of April 2013, the ANTARES detector was just resuming regular data taking after a six week period of unusual bioluminescent activity in the deep sea, in which the high voltage in the optical modules had been switched off. This security measure had been previously introduced to prevent the photo-multipliers from suffering high optical rates in the spring periods, when the background due to bioluminescence can exceed 500 kHz per PMT. The detector had been running in this state from March, 5 to April, 23 with only a few optical modules taking data with usual high voltage to monitor the deep-sea conditions continuously. In the first week after the optical modules had been turned on, the photo-multipliers were stabilizing slowly back to usual data taking. During this time, the threshold value for filtering highly charged photon pulses had been increased from 3 to 10 photo-electrons to limit the rate of accidental data triggering from background. Under these conditions, the telescope was recording data with a stable frequency of 3.6 Hz with a mean optical background rate of 127.8 kHz. Table 3.4 reports ANTARES data-taking conditions.

BURST PROPERTIES
The properties of GRB130427A needed for the definition of the coincident data search window and the simulation of its neutrino emission predicted by the NeuCosmA model were collected from the *Fermi*:GBM catalogue. I defined a search time window $T_{\rm search}$ as the time

Table 3.3. GRB130427A spectral parameters, as supplied by *Fermi*:GBM detector: BAND FIT is the functional form reported in Equation 1.4.

RA=173.14°	DEC=27.71°	$\Delta_{\rm err}$ = 4.68 arcsec
$T90$ = 138.24 s	$T_{\rm search}$=142.24 s	
$\alpha = -0.79$	$\beta = -3.06$	E_γ = 830 keV
BAND FIT		
$F_\gamma = 2.46\times10^{-3}$	$E_{\rm min}$=0.01 MeV	$E_{\rm max}$=1 MeV
$t_{\rm var}$ = 0.04 s		
z=0.34		

Table 3.4. ANTARES data taking conditions during GRB130427A trigger.

Run number	70515
Run UT start time (hh:mm:ss)	01:36:28
Run duration (hh:mm:ss)	12:01:59
High-charge threshold	10 photo-electrons
$\langle\mu\rangle$	127.8 kHz
m(μ)	66.6 kHz
$\mu_{\rm baseline}$	62.7 kHz
Setup	Line 1-12 Physics Trigger 3N+2T3+K40+TS0

T90 measured by *Fermi* with a ± 2 s margin around it, in order to account for satellite uncertainty on the time measurement (∼ 1 s), ANTARES DAQ uncertainty (∼ 0.4 s) and light propagation from the satellite to the detector (∼ 0.5 s). All parameters are summarized in Table 3.3. The flux of GRB130427A, as measured from several detectors, is shown in Figure 3.4: because it manifests a double-peak feature, a Time-Resolved analysis could really improve the neutrinos flux expectation from this burst. The whole analysis and its results will be presented in Chapter 5.

PROGENITOR ASSOCIATION

As presented in Section 1.4 the link between long GRBs and supernovae (SNe) stands for SN Ic, identified as core-collapse SN in whose spectrum hydrogen and helium lines are missing. This can be due to a huge stellar wind that pulls away the most external star's layers or to a mass transfer towards a companion, if the star founds to be in a binary system.
A detailed study of the connection between GRB130427A and the SN2013cq has been performed by the Hubble Space Telescope (HST) Collaboration [61]. HST observed the location of GRB130427A on 20 May 2013, 23 days after the initial burst detection, and in April 2014, almost a year after. First year observations are reported in Figure 3.5. Two observations are needed in order to obtain a host free spectrum: this is shown in the upper panel of Figure 3.6 both before and after subtraction of the afterglow and host light. Broad features, consistent with those seen in other high velocity SN Ic associated with GRBs, are visible in the spectrum. The absence of broad emission at Hα or He absorption rules out type II or Ib events respectively. The lower panel shows the similarity between SN2013cq and other SN/GRB pairs: a close match for the overall spectral shape and luminosity can be seen especially for SN1998bw. The similarity in appearance of these SNe is primarily due to the overall spectral shape, with a drop in luminosity of a factor of ∼ 3 over the 5000-7000 Å range. SN1998bw was associated with GRB980425, a burst six order of magnitude less energetic in γ-ray than GRB130427A. Therefore, the similar properties of the SNe and hosts over six orders of magnitude in GRB isotropic equivalent energy would appear to suggest that the energy of the GRB is not a strong function of environment or the mass of the progenitor star. It seems that, even though these associated SNe have similar masses and composition, they

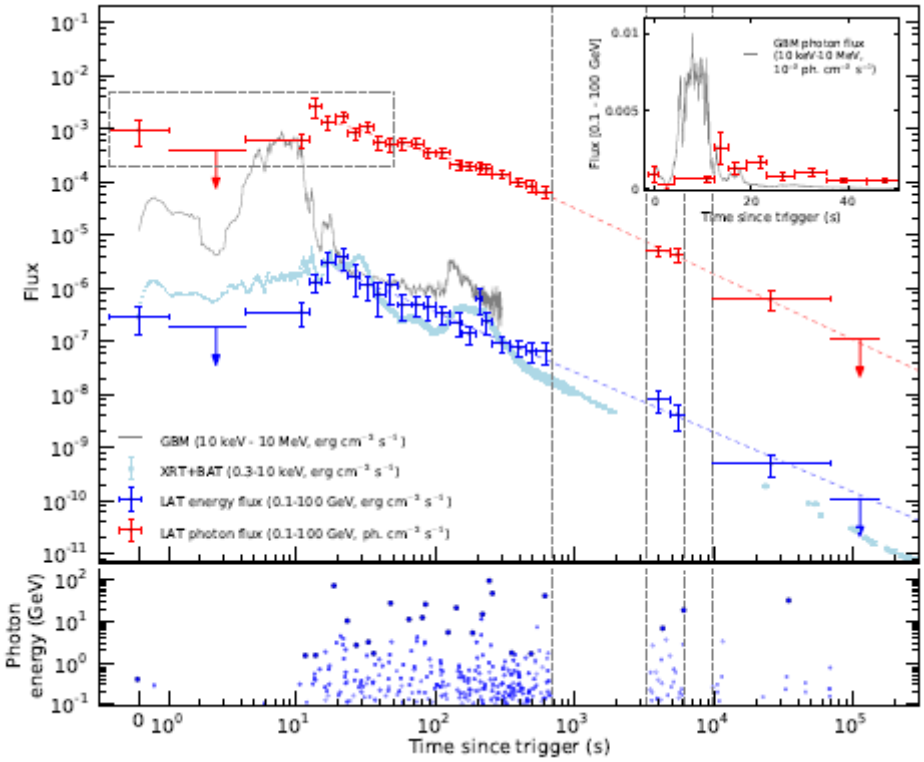

Figure 3.4. GRB130427A LAT temporally extended emission. TOP: LAT energy flux (blue) and photon flux (red) light curves. The photon flux light curve shows a significant break at a few hundred seconds (red dashed line), while the energy flux light curve is well described by a single power law (blue dashed line). The 10 keV to 10 MeV (GBM, gray) and 0.3 to 10 keV (XRT+BAT, light blue) energy flux light curves are overplotted. The inset shows an expanded view of the first 50 seconds with a linear axes, with the photon flux light curve from the GBM (in units of 10^{-2} ph cm^{-2} s^{-1}) plotted in gray for comparison. BOTTOM: Energies of all photons with probability >90% of being associated with the GRB. Filled circles correspond to the photon with the highest energy for each time interval. (Figure from [8]).

are responsible for two completely different luminosity functions of GRBs (see Figure 3.6).

For what concerns the host galaxy, HST observations show that GRB130427A lies at a spatial offset of 4.0 kpc (1 pc = 3.26 ly $\sim 3 \times 10^{16}$ m) at z = 0.34 from the centre of its host. The galaxy exhibits a bar-like structure with a weak spiral, making the host one of few to be classified as a spiral. Imaging also shows weak star formation close to the centre of the galaxy, but the most striking feature is a strong star forming region offset from the GRB position by 1.5 kpc. This region is the strongest region of star formation in the host galaxy. Because the weak spiral arm in the direction of the GRB also appears distorted, it may be that star formation has been triggered via a tidal interaction.

Finally, in the large field of view around GRB130427A several galaxies of similar magnitude are present, as Figure 3.5 shows: they might be part of a structure at the same redshift, even though they don't exhibit strong spectral lines.

3.3 Data set

Once the target source of the analysis has been identified, data have to be considered, both for a background estimation and the signal search. Indeed, data contain both background and signal events, therefore some selection criteria have to be implemented in order to discriminate among them. These criteria depend on the specific analysis: the following analysis aims to detect cosmic neutrinos from transient sources below ANTARES horizon. As will be

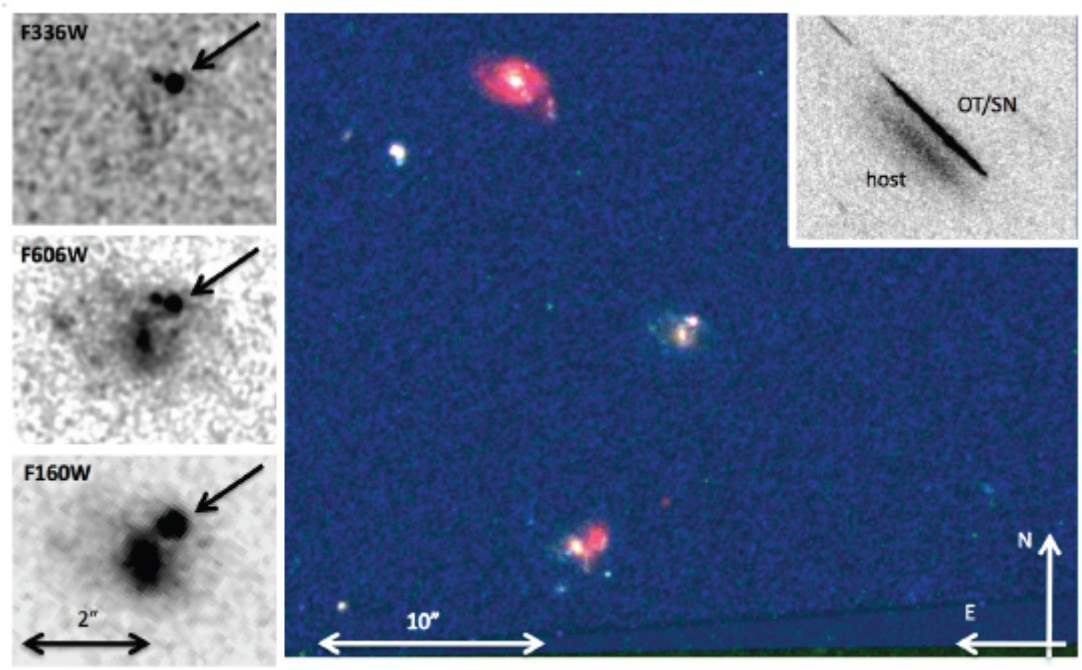

Figure 3.5. HST observations of GRB130427A. The left hand panel shows UV-optical and IR imaging (the UV data taken on 20 May 2013 and the optical/IR on 10 July 2013). The afterglow, indicated by an arrow, can be clearly seen offset 0.83" from the centre of its host galaxy. In the UV the host is weakly detected, with a strong star forming region seen to the east of the GRB location. The middle left image shows a disk galaxy with hints of a bar structure, along with some sign of distortion possibly due to on-going interaction. The large central panel shows a colour image from the three-band HST imaging. The host is at the centre, while other galaxies, possibly part of a structure at the same redshift are visible. The top right hand panel shows spectroscopy of the host galaxy. (Figure from [61]).

shown at the end of next chapter, the distinction between neutrinos from a point-like source and background neutrinos can only be achieved statistically. It is necessary to evaluate if the events accumulation around a certain position in the sky can be explained through a background fluctuation or if otherwise it can come from an "astrophysical neutrinos source". Given that we are looking for neutrinos coming from a specific direction in the space at a specific time, the detector angular resolution plays an important role: in fact, dealing with cosmological sources, a bad angular resolution implies no pointing capability at large distances.
Data selection starts with the selection of periods in which data have been collected: a data-taking period is called *run* and typically lasts from 3 to 12 hours. Because environmental and detector's conditions change with time, a run selection has to be applied in order to consider only time periods in which the detector is in a nominal state; then, also a selection on data themselves have to be applied, in order to identify the most reliable events. This thesis is based on ANTARES data collected during the entire solar year 2013 and already processed (run number from 68692 to 74348).

3.3.1 Run selection

A part from physics runs, during which the detector is in nominal data-taking conditions, ANTARES collects other data samples, in particular calibration runs, during which LEDs and hydrophones are used. Therefore, in order to analyse just physics runs, an initial selection has to be made.
Three main criteria have been applied:

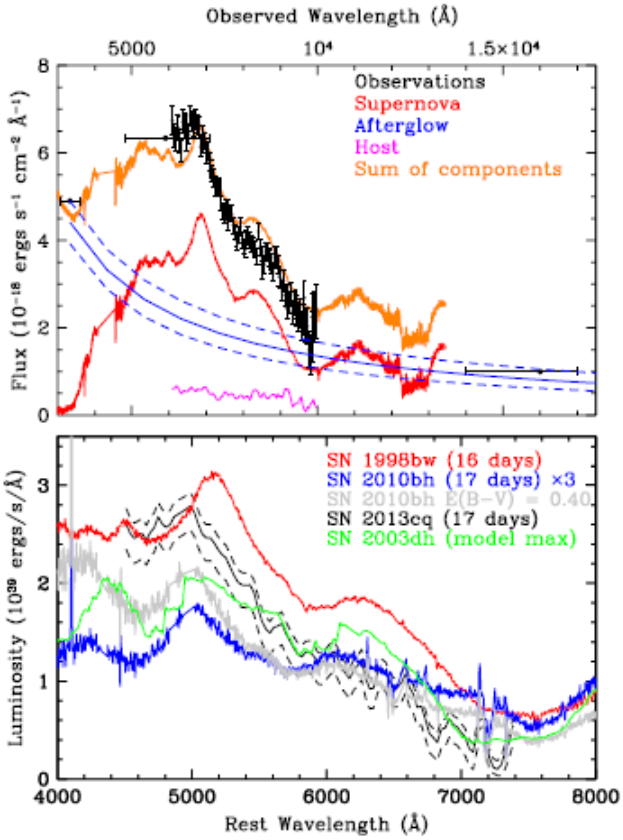

Figure 3.6. The spectral energy distribution of GRB130427A/SN2013cq as measured with HST. The top panel shows the data (black) along with the different components that may contribute as indicated. The host galaxy spectrum is based on HST extraction of the host directly under the GRB position and not on its global properties. The lower panel shows the SN spectrum after subtraction of the afterglow light, directly compared against spectra of other GRB/SNe pairs. The supernovae have been scaled as shown in the legend. (Figure from [61]).

- SCAN FLAG $\neq 1$: this variable is equal to 1 if the run is a calibration run, while it's different from 1 if the run is a physics run, thus this is to select just physics runs;
- NO SPARKING RUNS: these are runs containing events with an exceptionally high hit multiplicity, because some PMTs suffer a high voltage surge, so they are not considered reliable;
- QualityBasic[6] ≥ 1: this variable quantifies the information on the run quality, according to some properties, as the bioluminescence optical noise or the number of active PMTs, thus this cut allows to discard less favourable runs.

After this selections and after removing run 70515, 710 runs are left, corresponding to ~ 141 days of lifetime. This sample will be used for the background estimation, as will be presented in Section 4.1.

[6]QualityBasic (QB) can assume four values:

- QB=1: is the minimum request for a run to be used for analyses;
- QB=2: 80% of OMs active during the run;
- QB=3: Baseline$\leq$120 kHz + burst fraction ≤ 0.4;
- QB=4: Baseline$\leq$120 kHz + burst fraction ≤ 0.2.

3.3.2 Event selection

After selecting good quality physics runs, it is necessary to select also events in the chosen runs. This time, two kind of criteria can be identified: "pre-selection cuts" and "quality cuts". The first type contains cuts for a point source analysis, the second one, instead, contains optimised cuts for this specific analysis.

Pre-selection cuts
In a point source search, each event has to be associated with a muon track or a shower event, taking place in a clean environment: events are characterized by different triggers, as described in Section 2.3.3, able to select them according to physical and geometrical properties. For this analysis, only events with 3N or T3 triggers are selected.
As stated before, a good angular resolution is needed in point sources search: therefore, events has to be taken with $\beta < 1°$, for both tracks and showers reconstructed with AAFit. Finally, because point sources analyses are typically implemented for sources below ANTARES horizon, only up-going events have to be selected: this means to require $\theta > \pi/2$.

Quality cuts
Quality cuts depend on the specific analysis that is going to be performed: for example, in the search of high-energy neutrinos a cut can be done on the number of used hits or on the charge deposited in each PMTs, because these two parameters give an idea of the energy released inside the detector and consequently of the energy of the ultra-relativistic particle. This is not exactly the case of this analysis, since the expected neutrinos spectrum ranges over several order of magnitude. Anyway, a typical quality cut is the one applied on the aforementioned reconstruction parameter Λ (see Equation 2.10): the greater it is, the greater was the chosen likelihood. This analysis is exactly thought in order to find the optimal Λ cut, as will be described in Section 4.4.

3.4 General statistics

Data events in the ANTARES detector are assumed to occur independently of each other, so that the number of observed signatures n at a given mean rate μ follows a Poissonian distribution:

$$P(n|\mu) = e^{-\mu}\frac{\mu^n}{n!} \tag{3.2}$$

In hypothesis testing, usually a single measure is calculated from the attributes describing an observation: such a so-called test statistic quantifies the compatibility of the data with the background-only or background plus signal hypotheses. In the simplest case, this could be for instance the mere number of data events n that passed the selection criteria of a basic counting experiment (in a binned search) or any other value summarizing the measured data. A powerful test statistic is characterized by its capability to discriminate signal from pure background. The significance of a measurement is determined by its probability to originate from background only and is specified by the so-called p-value. It is derived from the probability to yield values of the test statistic Q at least as extreme as that observed if the background-only hypothesis (with rate μ_b) was true

$$p = P(Q \geq Q_{\text{meas}}|\mu_b) \tag{3.3}$$

The significance is then determined by the deviation of an observed Gaussian-like distributed variable from its mean value that corresponds to this p-value:

$$p = \left[\frac{1}{2}\right]\frac{2}{\sqrt{\pi}}\int_{\sigma/\sqrt{2}}^{\infty} e^{-x^2}\,dx = \left[\frac{1}{2}\right](1 - \text{erf}(\sigma/\sqrt{2})) \tag{3.4}$$

Table 3.5. Standard p-values for different significance levels.

two-sided	one-sided
3σ: $p_{3\sigma}$=(1-erf($3/\sqrt{2}$))=2.7 $\times 10^{-3}$	$p_{3\sigma} = \frac{1}{2}$(1-erf($3/\sqrt{2}$))=1.3 $\times 10^{-3}$
5σ: $p_{5\sigma}$=(1-erf($5/\sqrt{2}$))=5.7 $\times 10^{-7}$	$p_{5\sigma} = \frac{1}{2}$(1-erf($5/\sqrt{2}$))=2.8 $\times 10^{-7}$

where the factor [1/2] is used in the one-sided convention, in which only one of the sides of the Gaussian distribution is being considered. Standard p-values for 3σ and 5σ significance are shown in Table 3.5.

Following the ANTARES analysis policy, the two-sided convention will be employed throughout this work if not mentioned otherwise. For any significance level therefore, the threshold of a test statistic Q_{thres} can be derived: it corresponds to an excess of the measurement at that significance level. Upper limits can be set on the signal flux in cases where no significant excess can be identified: a 90% confidence-level upper limit can be placed, for instance, as that signal flux that would yield values of the test statistic as extreme as the measurement in 90% of all cases.

To derive the distributions of the test statistic in the background-only or signal hypothesis, usually a large number of pseudo-experiments are implemented that mimic a measurement's result. To infer threshold values at an aimed p-value, it is consequently necessary to generate more than 1/p pseudo-experiments to yield sufficient statistics.

Note that in the case of a simple counting experiment, the p-value is given by the probability to observe at least n_{obs} events from a Poissonian distribution with the mean background rate μ_b:

$$P(n \geq n_{\text{obs}}|\mu_b) \tag{3.5}$$

In case of a single observed event $n_{\text{obs}} = 1$, the previous formula reduces to

$$p = P(\geq 1|\mu_b) = 1 - P(0|\mu_b) = 1 - e^{-\mu_b} \tag{3.6}$$

Due to the Taylor expansion of the exponential function for $\mu_b \ll 1$

$$P(\geq 1|\mu_b) = 1 - P(0|\mu_b) = 1 - e^{-\mu_b} \sim 1 - 1 + \mu_b - \mu_b^2/2 - \cdots \sim \mu_b \tag{3.7}$$

Therefore, a suppression of the background rate μ_b to the level of a particular p-value ensures that a single event can be identified with the associated significance, i.e., $n_{\text{thres}} = 1$.

There are different ways to optimise an analysis, for example to guarantee best discovery performances or to place a preferably low upper limit on the true signal flux in case of non-observation. In the following, I will select the first option. The probability to detect a signal with rate μ_s is called statistical power or discovery potential (or MDP):

$$MDP = P(Q \geq Q_{\text{thres}}|\mu_b + \mu_s) \tag{3.8}$$

that reduces to

$$MDP = P(n \geq n_{\text{thres}}|\mu_b + \mu_s) \tag{3.9}$$

in the case of a counting search. It gives the probability to detect an excess at a predetermined significance level, i.e., to measure a test statistic above the critical threshold value Q_{thres}. The event selection should consequently maximize this discovery probability.
Details of the analysis are presented in the next chapter.

Chapter 4

High-Energy Neutrinos from GRB130427A

In this chapter I will focus the search for high-energy neutrinos on GRB130427A, describing the statistical analysis required by an un-binned search. It is based on the comparison between the Probability Density Function (PDF) of background and of signal events, in a research cone of amplitude equal to 10°: the cone amplitude is chosen in such a way that a significant part of the expected signal events is contained inside it (about 85%). Therefore, the amplitude of the cone is fixed and mainly includes track signatures, while the analysis is optimised for the quality cut on Λ, presented in Equation 2.10: this parameter represents the logarithm of the likelihood of the hits time residuals as a function of the track's parameters (muon's position and direction). Its typical value ranges between -12 and -4: the greater it is, the better is the agreement between the expected and the observed hit times of the track. Optimization is made maximizing the aforementioned (see Section 3.4) Model Discovery Potential (MDP).
In order to get the desired PDFs, a background estimation is presented in Section 4.1 and signal Monte Carlo simulations are described in Section 4.2. In Section 4.3, an extended maximum likelihood ratio is defined as test statistic; in the same section, pseudo-experiments are introduced. In Section 4.4, the optimisation technique, based on the maximization of the MDP, is explained in order to achieve the best Λ cut.

NOTE: According to the ANTARES policy, all the analysis is developed using blind data, that are the ANTARES data with scrambled time-position information: in this way, all the cuts are fixed before the unblinding. Only after the approval from the Collaboration, real data can be approached and a neutrino signal can be searched for.

4.1 Background estimation

Atmospheric neutrinos from below the local horizon constitute the main background component in the search for cosmic neutrinos, with a smaller contribution coming from falsely reconstructed down-going atmospheric muons. To estimate the expected number of background events μ_b in coincidence with the burst as realistically as possible, data were used. However, as the number of up-going events is very low ($\sim$ 4/day), long time periods are needed to yield sufficient statistics, which in turn requires averaging over different data-taking conditions (in particular because of seasonal variations of the optical background). To compensate for this effect, the average rate of reconstructed events in the GRB's direction $\langle n(\theta_{\mathrm{GRB}}, \phi_{\mathrm{GRB}})\rangle_{\text{all runs}}$ in local coordinates zenith θ and azimuth ϕ was first estimated, using data recorded during the entire period from January 1, 2013 to the end of 2013, excluding the burst's run 70515. The corresponding mean rate at the GRB's position was compared

to the mean of time-averaged rates within a 10° cone around this position. Between these two values the largest was chosen: it was the rate in the GRB's position. This established a conservative estimate, accounting for non-uniformity of the background in the vicinity of the GRB's position. The total number of events in local coordinates, elevation and azimuth, is shown in Figure 4.1 for a certain selection on the reconstruction quality, $\Lambda > -6$: it can be seen how most of the events are down-going. Moreover, the detector's geometry (12 strings) reflects the presence of some preferential directions.

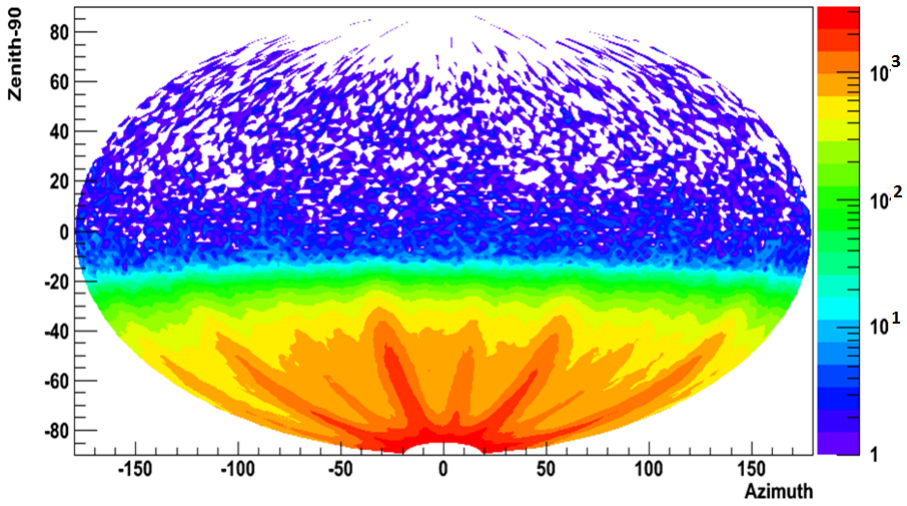

Figure 4.1. Distribution in local coordinates, elevation and azimuth, of all events of the processed 2013 runs ($\sim$ 141 days of livetime), used to evaluate the mean rate in the GRB's direction (see Equation 4.1). This plot is for quality parameters $\Lambda > -6.0$ and $\beta < 1°$.

This average has to be adjusted for variations of data-taking conditions during the period analysed: to take into account the efficiency variation of the detector due to different environmental conditions in time, the average rate has been scaled by a correction factor c_i for the particular data-taking run i (70515). This correction is called *instantaneous efficiency*: it is computed by the ratio between the number of events from all directions in the i run, n_i, and the duration of this run, t_i, times the ratio between the sum of all runs' duration, except the i run, and the sum of all events in these runs, $\sum t_j / \sum n_j$ (see Equation 4.1). To improve the background estimation for the considered run, the number of events n_i is replaced by the 90% C.L. upper limit assuming a Gaussian distribution, $[n_i]^{90\%}$. In this way, the expected number of background events in coincidence with the GRB's search-time window T_{search} has to be calculated via

$$\mu_b(\theta_{GRB}, \phi_{GRB}) = T_{search} \ \langle n(\theta_{GRB}, \phi_{GRB}) \rangle_{\text{all runs}} \ c_i \tag{4.1}$$

$$\text{with } c_i = \frac{[n_i]^{90\%}}{t_i} \frac{\sum t_j}{\sum n_j}$$

Such approach assumes that the total number of events, dominated mostly by down-going atmospheric muons, is proportional to the number of up-going events: in this way the huge quantity of down-going data can be used to estimate the background. This assumption has been tested, comparing the measured rate of up-going events and the rate estimated through Equation 4.1: analysing data from run 70515, the measured rate was found to be smaller or equal to the expected rate for different Λ cut. Therefore the proportionality can be considered verified.

The number of background events in coincidence with the burst and within 10° around its

position was evaluated to be of the order of 10^{-3} (see Table 4.1). The background PDF, $B(\alpha) = dN/d\Omega$, is assumed to be flat in solid angle within this cone.

4.2 Signal Probability Density Function

For the selected Gamma-Ray Burst, 5 $\times 10^8$ events due to neutrino interactions were generated in order to simulate the signal predicted by NeuCosmA from the collected γ input parameters: the generation is done through a Run By Run Monte Carlo simulation, with the option Local Point Mode True (LPMT), allowing to insert the local coordinates of the burst (transformed from equatorial through the ANTARES ASTRO library). The simulation refers to the ANTARES run corresponding to the trigger time: this is done in order to reproduce the trigger and calibration conditions of the selected run. The simulated events are then reconstructed (AAFit for both tracks and showers) to compute the acceptance of the detector. As in the case of the background, T3 (two first level hits in adjacent or next adjacent floors) or 3N (five first level hits in a 2.2 μs time window) triggers are asked for and to ensure well reconstructed directions (θ and ϕ) of the selected neutrino candidates, $\beta < 1^\circ$ is required. Since the narrow time window (a few tens of seconds) yields intrinsically low background in coincidence with the GRB, events selection regarding the quality parameter Λ can be relaxed with respect to searches for steady astrophysical point sources (as for instance was done in [13]), in which the cut over the Λ parameter is more stringent while it is possible to vary the angular cone to optimise the analysis. In this search, depending on the expected background and signal flux, the Λ criterion will be chosen *ad hoc* for GRB130427A.
The Point Spread Function (PSF), that describes the detector's angular response in terms of its pointing accuracy expressing the spread of the reconstructed tracks around the primary direction, has to be known in order to have the signal Probability Density Function. The PDF is a PSF normalized to the solid angle, therefore it expresses the probability to reconstruct an event at a certain angular distance. The PSF is found analysing MC events and determining for each of them:

1. $\Delta\theta = \theta_{MC} - \theta_{REC}$: the difference between the zenith angle of the primary particle (θ_{MC}) and that of the reconstructed particle (θ_{REC});

2. $\Delta\phi = \phi_{MC} - \phi_{REC}$: the difference between the azimuth angle of the primary particle (ϕ_{MC}) and that of the reconstructed particle (ϕ_{REC}).

To reproduce the expected neutrino flux from the GRB source, a weight has to be applied to each event, according to the flavor of the generated neutrino. This weight is given by the NeuCosmA code from the fluence obtained numerically with the GRB parameters reported in Table 3.3. This fluence is represented in Figure 4.2 for each neutrino flavor for the GRB130427A simulation: the predicted fluence is different between electronic and muonic/tauonic flavor because oscillations are taken into account, including matter effect (MSW) for neutrinos propagation through Earth. Once weights are calculated, they can be applied according to the description in Appendix A.
In analogy with optical astronomy, the PSF can be expressed in terms of the angular distances in the zenith and azimuth directions: in Figure 4.6 the zenith and azimuth distributions, obtained following the previously defined steps 1) and 2), for quality cuts $\Lambda > -5.5$ and $\beta < 1^\circ$ are illustrated. As can be seen, they are Gaussian distributions, peaked around the zero, that represents the burst's position; the signal PSF can be therefore straightforwardly obtained and it is drawn in Figure 4.7, for the same quality cuts. Its spherical symmetry and small aperture is a result of the reconstruction algorithm for tracks, AAFit. Its performances can also be seen in Figures 4.4, 4.5 and 4.3, that show results obtained analysing MC events. In Figures 4.4 and 4.5 plots of the Λ and β distributions are reported: tracks from $\nu_\mu - \overline{\nu}_\mu$ CC interactions and tracks from hadronic showers are shown separately, so that the efficiency of

quality cuts on each sample can be seen. In Figure 4.3 the space angle distribution between the generated and the reconstructed event in the $\Lambda - \beta$ space is shown, in order to see the effect of quality cuts on the reconstructed space angle.

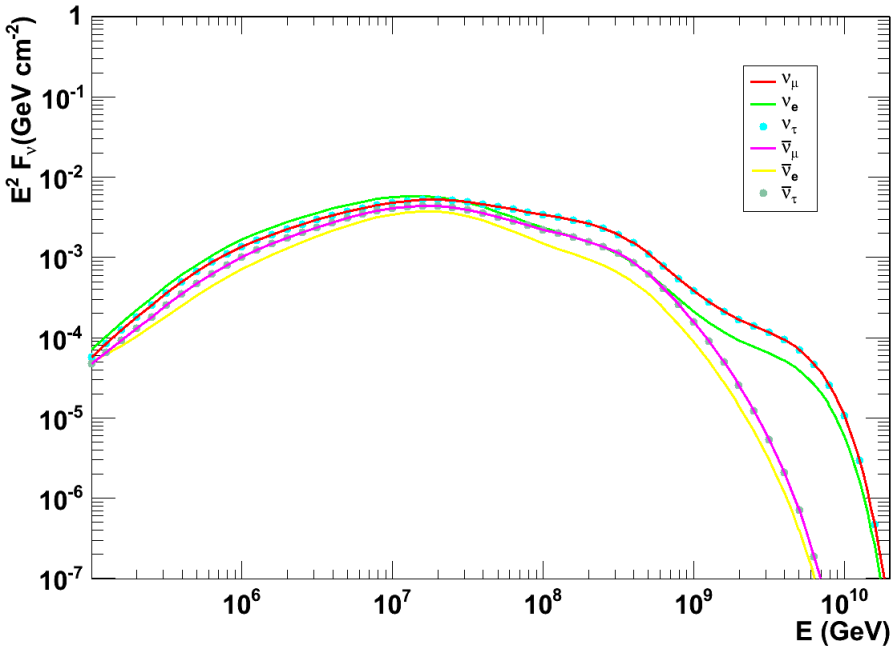

Figure 4.2. NeuCosmA expectations for all neutrino kinds from GRB130427A: the code input parameters are reported in Table 3.3. As can be seen different predictions are expected for ν_μ and $\overline{\nu}_\mu$, due to different production channels; moreover, matter effect acts on ν_e and $\overline{\nu}_e$ expectations.

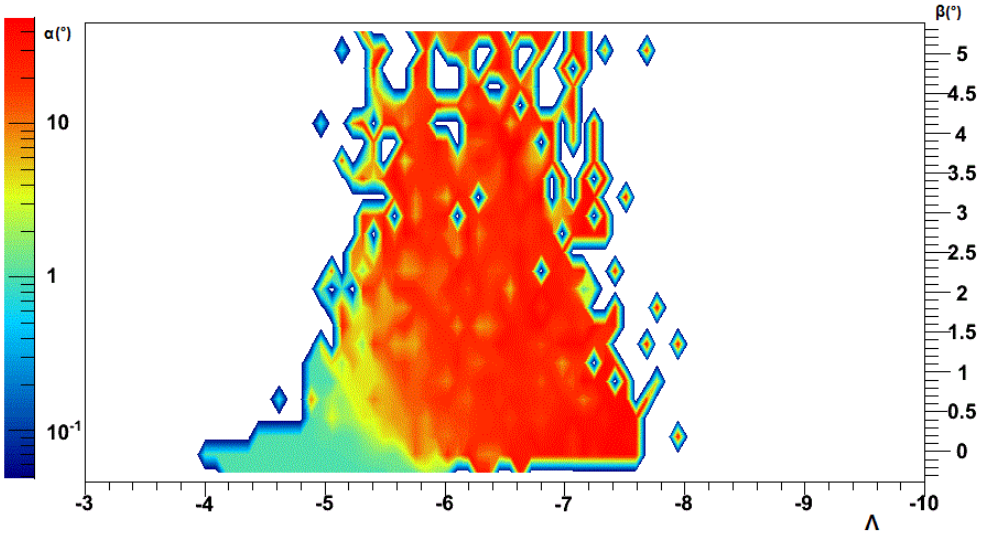

Figure 4.3. Distribution of Λ and β when no cuts are applied: the space angle α on the Great-Circle between the generated (θ_1, ϕ_1) and the reconstructed (θ_2, ϕ_2) direction is color-coded. It is defined as $\alpha = \arccos(\sin\theta_1 \sin\theta_2 \cos\phi_1 \cos\phi_2 + \cos\theta_1 \cos\theta_2 + \sin\theta_1 \sin\theta_2 \sin\phi_1 \sin\phi_2)$, with θ the zenith angle and ϕ the azimuth angle.

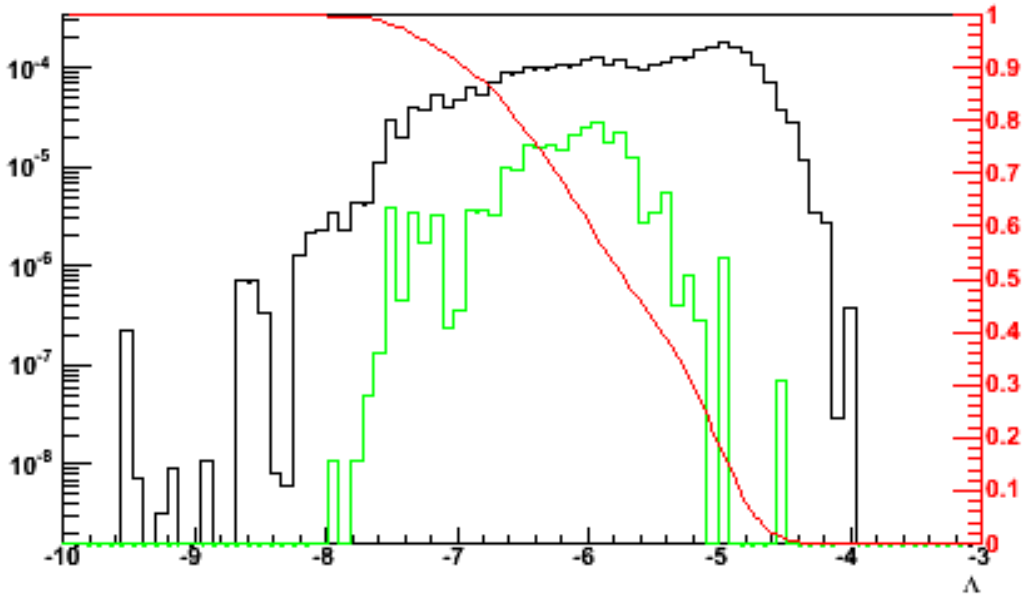

Figure 4.4. Λ distribution for tracks from $\nu_\mu - \overline{\nu}_\mu$ CC interactions (black) and tracks from hadronic showers (green); red curve and its scale on the right are for the cumulative distribution. No quality cuts are applied.

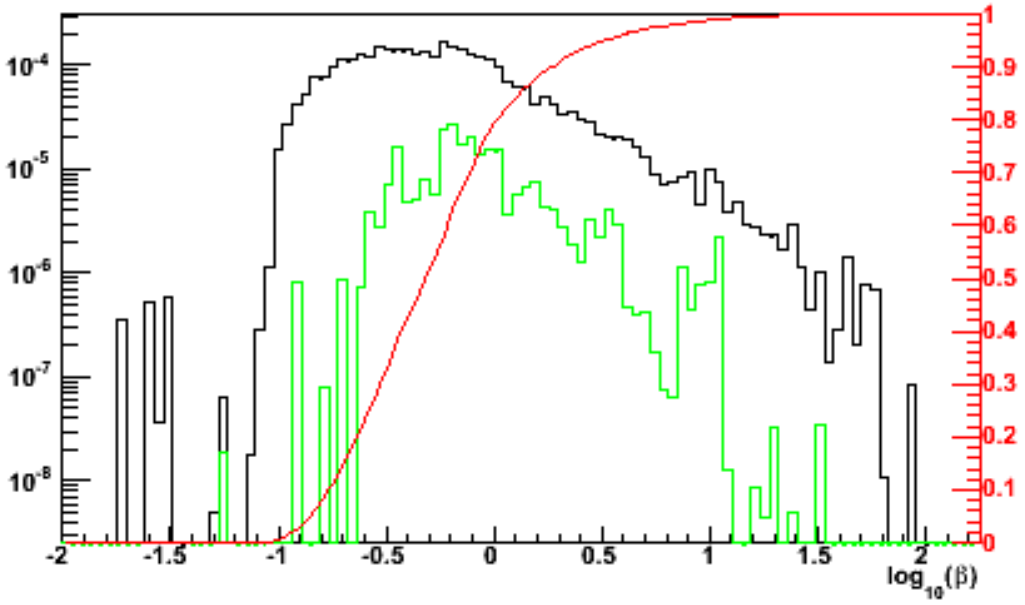

Figure 4.5. $\log_{10}\beta$ distribution for tracks from $\nu_\mu - \overline{\nu}_\mu$ CC interactions (black) and tracks from hadronic showers (green); red curve and its scale on the right are for the cumulative distribution. No quality cuts are applied.

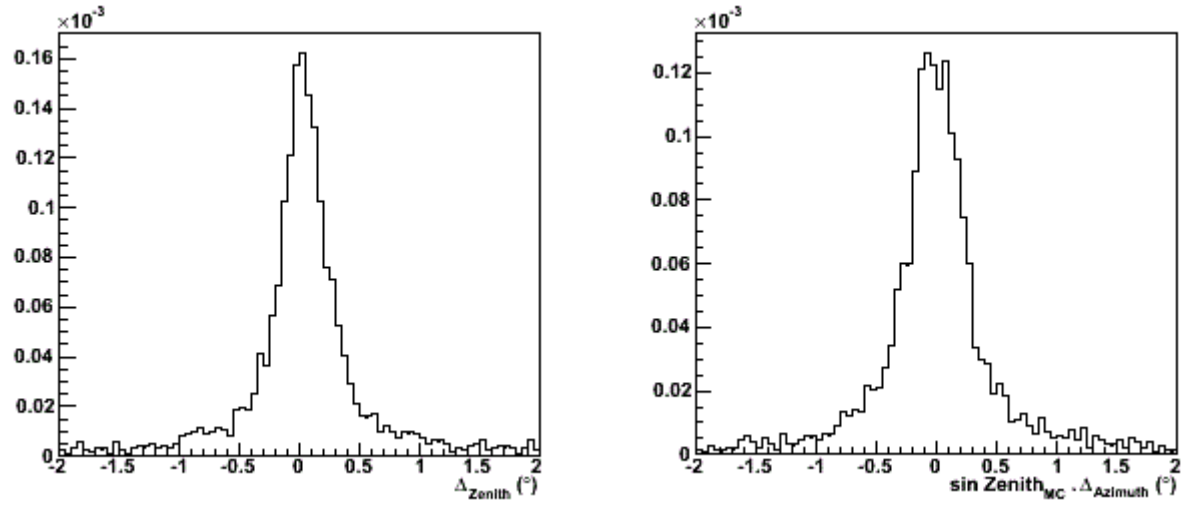

Figure 4.6. Distributions of $\Delta\theta$ (left) and $\Delta\phi \times \sin\theta_{\rm MC}$ (right), obtained with both tracks from $\nu_\mu - \overline{\nu}_\mu$ CC interactions and tracks from hadronic showers: cuts $\Lambda > -5.5$ and $\beta < 1°$ are here applied.

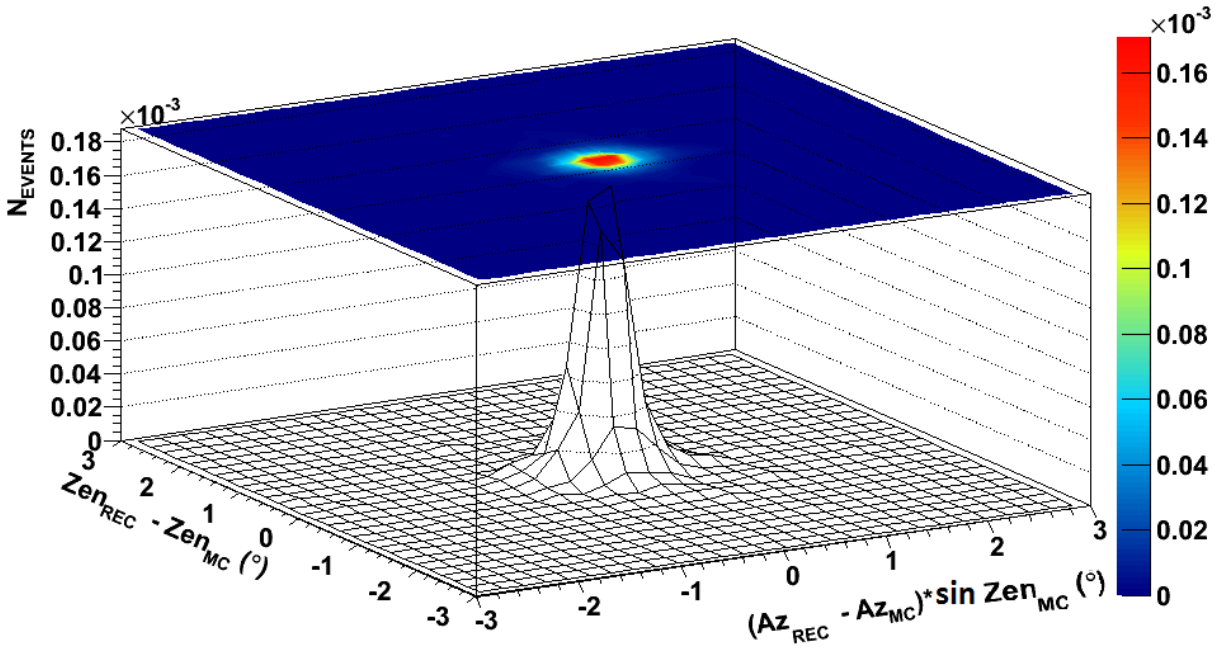

Figure 4.7. GRB130427A PSF, obtained with both tracks from $\nu_\mu - \overline{\nu}_\mu$ CC interactions and tracks from hadronic showers, with the cuts $\beta < 1°$ and $\Lambda > -5.5$; no satellite uncertainty is accounted for here, while GRB weight is applied to each event.

To account for the satellite's uncertainty $\Delta_{\rm err}$ on the direction of the GRB, the reconstructed position has to be additionally smeared with a Gaussian of the same width $\Delta_{\rm err}$. Normalizing each bin of the PSF to the subtended solid angle allows to obtain the signal PDF S(α), which describes the number of events N reconstructed inside the solid angle $d\Omega = 2\pi d \sin\alpha$ at a distance α from the burst:

$$S(\alpha) = \frac{dN(\alpha)}{d\Omega} \tag{4.2}$$

The number of selected events is also a function of the quality cut on Λ, therefore each cut is linked to a different PDF.
The signal PDF can be parametrised with a function that is flat for small values of α, since all directions that are very close to the true position of the source should have the same probability to occur; the fitting function is a Rayleigh distribution of the form

$$\log S(\alpha) = \log \frac{dN(\alpha)}{d\Omega} = \begin{cases} A & \text{if } \alpha \leq \alpha_0 \\ A - B\Big(1 - \exp(\frac{-(\log\alpha - \log\alpha_0)^2}{2\sigma^2})\Big) & \text{if } \alpha > \alpha_0 \end{cases} \tag{4.3}$$

with the free parameters A, B, α_0 and σ, where σ is the equivalent of the ANTARES reconstruction parameter β. Fit results are shown in Figure 4.9: the greater is the Λ cut, the smaller is the detector's median resolution, because only well reconstructed events are accounted for.
As shown, the fit is done accounting only events with an angular distance up to 10° from the burst position. The choice of search cone amplitude is due to a compromise between the number of reconstructed events inside the cone and the computation time for pseudo-experiments: in line of principle, the fit would have been done on the whole distribution. The effect of the angular cone cut on the expected distribution of signal events is shown through the cumulative distribution of Figure 4.8: about 85% of the events are reconstructed within 10° from the burst position.

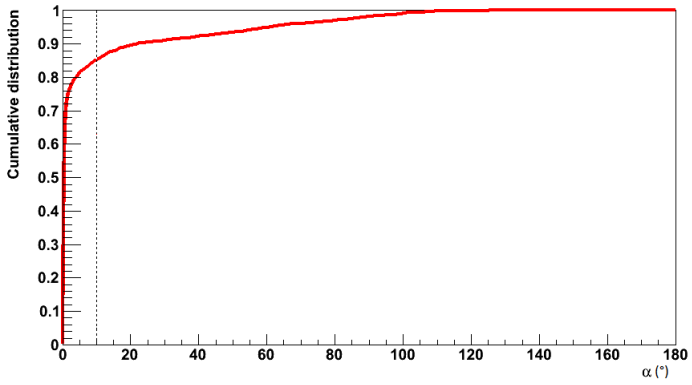

Figure 4.8. GRB130427A cumulative distribution of reconstructed events around the GRB's position: the vertical line at $\alpha = 10°$ corresponds to the half cone angle selected for the analysis, since it contains 85% of the expected signal events.

Within this angular search window, mainly signatures associated with tracks from $\nu_\mu - \overline{\nu}_\mu$ CC interactions contribute. Even if the defined search window (half cone angle $\alpha = 10°$) is much more extended than for usual point sources analyses, it is important to stress the fact that GRBs are transient sources, therefore the time window in which the coincident neutrinos search is performed is so small that the background contribution in it is almost null. So, the angular window can be chosen as a compromise between the contained signal events and the background introduced in this way.

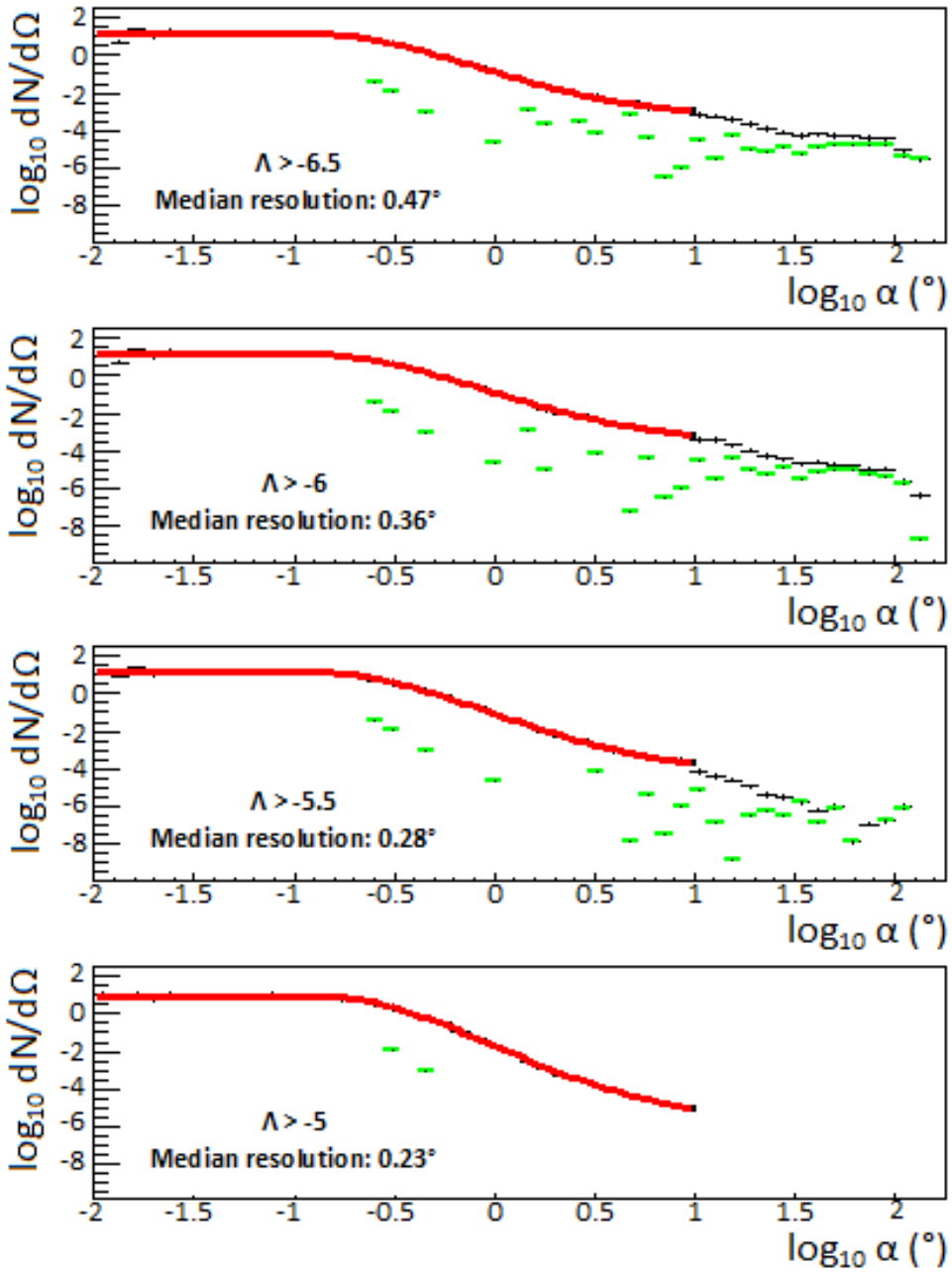

Figure 4.9. GRB130427A PDF, obtained with both tracks from $\nu_\mu - \overline{\nu}_\mu$ CC interactions (black) and tracks from hadronic showers (green) with $\beta < 1°$ and different Λ cuts; also shown are the number of expected events inside the 10° cone and the median resolution. Red curve is the functional fit, described in Equation 4.3, inside the defined angular window.

4.3 Pseudo-Experiments and Extended Maximum Likelihood Ratio

To mimic the signal and background contributions, special Monte Carlo simulations called pseudo-experiments have been performed. These allow to compute the significance of the measurement's result. A test statistic is needed in order to discriminate the background hypothesis from the signal one: an "extended maximum likelihood ratio" (see [25] and [27]) will be used through this work. It is defined as the ratio between the likelihood in the hypothesis of signal plus background and the likelihood in the background only hypothesis. The present search is un-binned, because in case of a small number of events a binning procedure would bring to small values of bin contents: therefore, likelihoods are not computed over bins but over events.
Signal and background events i with space angle α_i are drawn randomly from the normalized signal S(α) and background B(α) PDFs corresponding to each chosen cut on Λ (see Figure 4.9). For each pseudo-experiment with a total number of events $\mathrm{n_{tot}}$, a test statistic Q, defined as $Q = \log \mathcal{L}^{\max}_{\mathrm{s+b}} - \log \mathcal{L}_{\mathrm{b}}$, is calculated as follows (see [30]):

$$Q = \max_{\mu_s^{'} \in [0; n_{\mathrm{tot}}]} \Big(\sum_{i=1}^{n_{\mathrm{tot}}} \log \frac{\mu_s^{'} S(\alpha_i) + \mu_b B(\alpha_i)}{\mu_b B(\alpha_i)} - \mu_s^{'} \Big) \tag{4.4}$$

Poissonian fluctuations of the total number of events have to be taken into account: this introduces the second term in Equation 4.4, that gives the attribute of extended.
The expected number of background events μ_b is a fixed value, computed through Equation 4.1, while the signal contribution $\mu_s^{'}$ is scanned between 0 and $\mathrm{n_{tot}}$.
High values of Q indicate that the measurement is more compatible with the signal hypothesis (see Section 3.4). Such test statistic makes use of the information incorporated in the spatial distributions of the expected signal and background flux. While the background is uniformly distributed, the signal is expected to be centred at the Gamma-Ray Burst's position.
In the following, $h_{n_s}(Q) = (dN/dQ)_{n_s}$ denotes the distribution of Q values for n_s injected signal events with a Poisson-distributed number of background events with expectation value μ_b, as derived from the data. The significance of a measurement is determined by its p-value, which is given by the probability to yield Q values at least as high as that observed if the background-only hypothesis were true. Hence, using the background-only distribution $h_0(Q)$, the lowest Q value Q_p^{thres} that is necessary to claim a discovery with a certain p-value can be calculated via

$$P(Q \geq Q_p^{\mathrm{thres}} | \mu_b) = \int_{Q_p^{\mathrm{thres}}}^{\infty} h_0(Q)\, dQ = p \tag{4.5}$$

The probability distributions $h_{n_s}(Q)$ for different n_s are shown in Figure 4.10, with the threshold Q-values at different σ levels indicated by the gray dashed lines.

The probability distribution of Q values for any number of expected signal events μ_s is calculated via

$$P(Q|\mu_s) = \sum_{n_s=0}^{\infty} P(n_s|\mu_s) h_{n_s}(Q) \tag{4.6}$$

with the Poissonian distribution $P(n_s|\mu_s)$ giving the probability of observing n_s events from a mean number of expected events μ_s.

For each number of injected signal events n_s, 10^5 pseudo-experiments are generated to derive the signal distributions $h_{n_s}(Q)$, while more than 10^8 background-only pseudo-experiments to allow determining Q_p^{thres} at p-values as low as $p_{5\sigma}$.

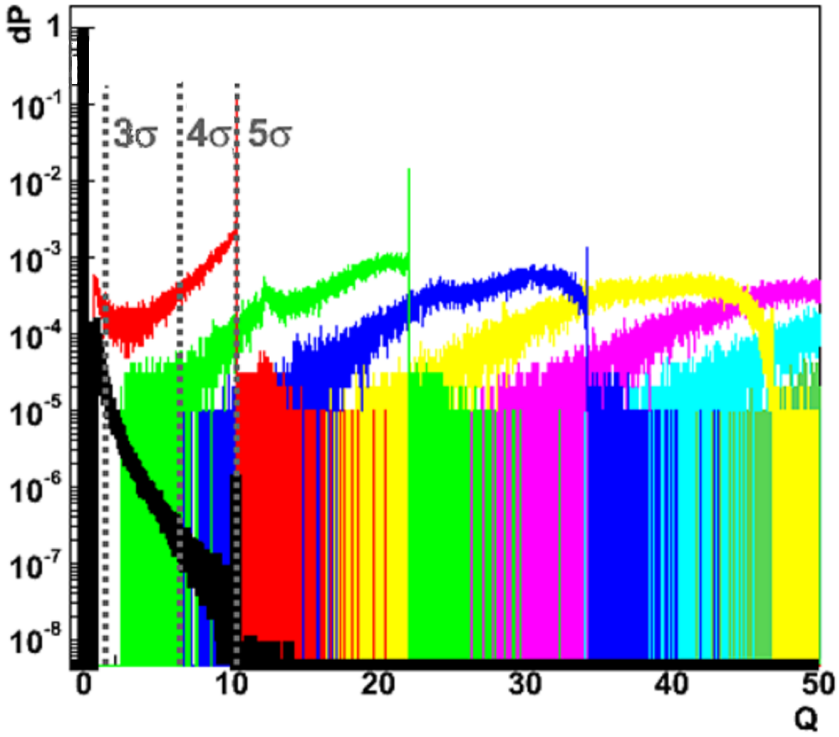

Figure 4.10. Probability distributions of Q-values, $h_{n_s}(Q)$, for different numbers of injected signal events n_s. Black is background only, $h_0(Q)$, red is $n_s = 1$, green is $n_s = 2$, blue is $n_s = 3$ and so on. Gray vertical lines indicate the threshold values Q_p^{thres} for different significances as calculated from $h_0(Q)$. This example shows $\Lambda > -6$ and $\mu_b = 9.87 \times 10^{-3}$ background events.

4.4 Search optimisation

Following the notation introduced in the previous section, the integral of $P(Q|\mu_s)$ gives the MDP (see also Section 3.4): it is the probability to make a discovery assuming that the model was correct. MDP is thus calculated as

$$MDP = P(Q \geq Q_p^{\text{thres}}|\mu_s) = \int_{Q_p^{\text{thres}}}^{\infty} P(Q|\mu_s)\, dQ = \sum_{n_s=0}^{\infty} P(n_s|\mu_s) \int_{Q_p^{\text{thres}}}^{\infty} h_{n_s}(Q)\, dQ \qquad (4.7)$$

The value of the Λ cut for the selected GRB was then chosen as the one maximizing the MDP for the value of μ_s predicted by the NeuCosmA model (see Section 1.6). Such optimal cut is naturally dependent on the significance level for which the MDP should be maximal. Figure 4.11 shows the discovery probability of GRB130427A for 3σ, 4σ, and 5σ versus an arbitrary number of signal events.

The distribution $P(Q|\mu_s)$ from Equation 4.4 is also used to set upper limits on the number of signal events when no discovery is made. When the search for correlated neutrino signatures in the ANTARES data returns a value Q_{meas} of the test statistic, a 90% confidence level (C.L.) upper limit $\mu_s^{90\%}$ on the signal strength can be set by rejecting all event expectations that lead to values $Q > Q_{\text{meas}}$ in 90% of all pseudo-experiments:

$$P(Q \geq Q^{\text{meas}}|\mu_s^{90\%}) = \int_{Q^{\text{meas}}}^{\infty} P(Q|\mu_s^{90\%})\, dQ = 0.9 \qquad (4.8)$$

When no event is found ($Q_{\text{meas}} = 0$), a 90% C.L. upper limit can be set at 2.3, the lowest possible value (see Section 3.4).

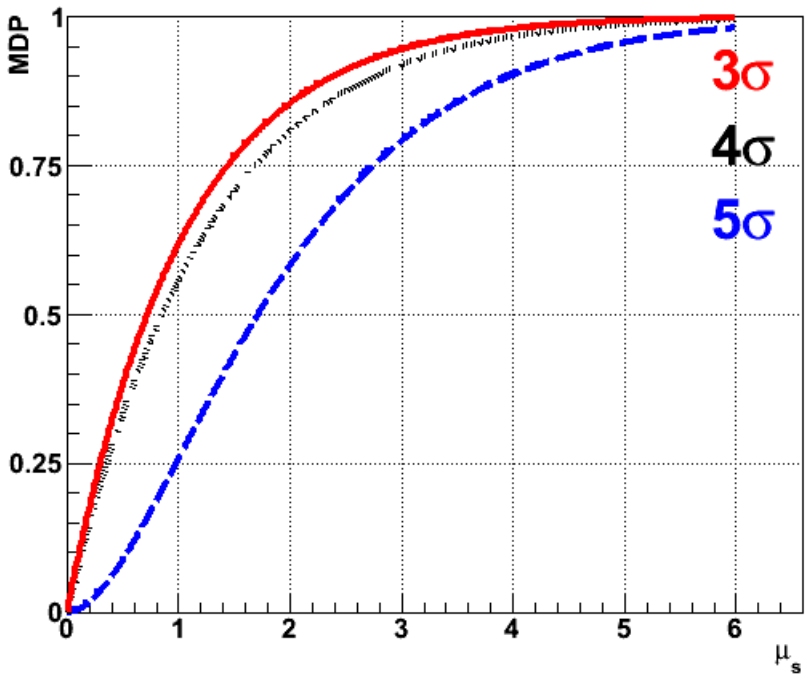

Figure 4.11. Model discovery potential (MDP) versus signal flux μ_s for 3σ (red solid line), 4σ (black dotted) and 5σ (blue dashed) for GRB130427A. Plot is for $\Lambda > -6$.

Using this procedure, the model discovery potential was calculated for the predicted signal flux μ_s and the final cut on Λ for GRB130427A was found. The probability to find evidence for an excess in the data at the 3σ level based on the NeuCosmA predictions is maximal when selecting signatures with $\Lambda > -6$, while a discovery of 5σ is most probable for $\Lambda > -5.3$. Table 4.1 summarizes the consequently expected number of background and signal events from the numerical NeuCosmA and the analytical Guetta models. Integrating the signal and background PDF, obtained for a certain Λ cut, inside the search cone allows to determine the expected number of signal and background events from the burst. With the selection criteria optimised for a 3σ significance, the expected background in the predefined search window of ~ 142 s and within 10° around the GRB's position is reduced to 10^{-2} events. The two models respectively predict 1.70×10^{-3} (NeuCosmA) and 2.05×10^{-2} (Guetta) signal neutrinos. Note that even if the background contribution exceeds the expected signal, the maximum likelihood ratio Q (Equation 4.4) can reliably distinguish between the flat background distribution and the signal that is peaked at the burst's location. With a chance of 0.5%, 3σ evidence of a neutrino signal associated with GRB130427A, as predicted from the NeuCosmA model, can be found in the ANTARES data.

Table 4.1. Optimized $\Lambda_{\rm cut}$ at the 3σ and 5σ level and the corresponding background and signal rates μ_b and μ_s, the median angular resolution m(α) and the probability MDP to discover an excess as predicted from the NeuCosmA model (see [58]) at the given significance for GRB130427A.

σ	$\Lambda_{\rm cut}$	μ_b	$\mu_s^{\rm NeuCosmA}$	$\mu_s^{\rm Guetta}$	m(α)	MDP
5	-5.3	1.37×10^{-4}	1.22×10^{-3}	1.45×10^{-2}	0.26°	1.08×10^{-3}
3	-6.0	9.87×10^{-3}	1.70×10^{-3}	2.05×10^{-2}	0.36°	4.32×10^{-3}

Selection criteria should be optimised to find 3σ evidence for a neutrino excess: this configuration indeed allows to place more stringent limits in case of a non-detection.

Chapter 5

GRB130427A: a Time-Resolved Analysis

In this chapter the innovative idea of a Time-Resolved analysis on neutrino emissions from a Gamma-Ray Burst will be presented. This technique is required since most GRBs manifest a multi-peak feature in their γ emission, in such a way that their spectrum is not adequately fitted by a single function. This is the case of GRB130427A, whose light curve exhibits an extremely bright phase, followed by a slow decay of the γ emission. A Time-Resolved (TR) analysis will be performed on this burst: resolving in time the source enables to treat independently each peak. The same analysis described in the previous chapter will be implemented on both peaks: as a result, an optimal Λ cut and an expected number of neutrino events will be found for each of them. The major assumption underlying this technique is the coincidence of gamma and neutrinos emission, that is also the basic idea of the photo-hadronic neutrino's production.
Therefore, in Section 5.1 the burst's Time-Resolved analysis of the γ spectrum from the *Konus-Wind* Collaboration is introduced; in Sections 5.2 and 5.3 the optimised analyses for neutrinos expectations from the first and the second pulse respectively are described; in Section 5.4 results from the unblind search in the defined time and space window are presented and in Section 5.5 a serendipitous search in an extended time window is discussed, in order to look for a precursor or delayed signal event.

5.1 Time-Resolved photons spectrum

GRB130427A manifested in its light curve a double-peak feature, as shown in Figure 5.1, where the burst's light curve in the 15 to 350 keV band is reported: two separated pulses are visible. The first pulse is the main one: it alone constitutes more than 95% of the burst γ-fluence and is actually released in one twelfth of the whole burst's duration.

Konus-Wind Collaboration had analysed the burst in TR mode, supplying the spectral parameters of the two peaks. The *Konus-Wind* light curve shows a multi-peaked emission complex started at the trigger time T_0, peaked at $\sim T_0$+8 s, and having a duration of $\sim$ 20 s. The emission is seen up to $\sim$12 MeV. This extremely bright phase of the event passes into a weaker decaying tail out to $\sim T_0$+120 s, when the second emission episode started. It shows a Fast Rise Exponential Decay (FRED) pulse, $\sim$100 times weaker in a peak count rate than the initial complex. The decaying emission is detectable in the 20-1200 keV band out to $\sim T_0$+250 s. Assuming z=0.34 and a standard cosmology model with $H_0 = 70$ km/s/Mpc, $\Omega_M = 0.27$ and $\Omega_\Lambda = 0.73$, the isotropic energy release is $E_{\rm iso} \sim 8.5 \times 10^{53}$ erg and the peak luminosity is $L_{\rm iso}^{\rm max} \sim 2.7 \times 10^{53}$ erg/s.
To analyse the two episodes in the same spectral band, I will use *Konus-Wind* information.

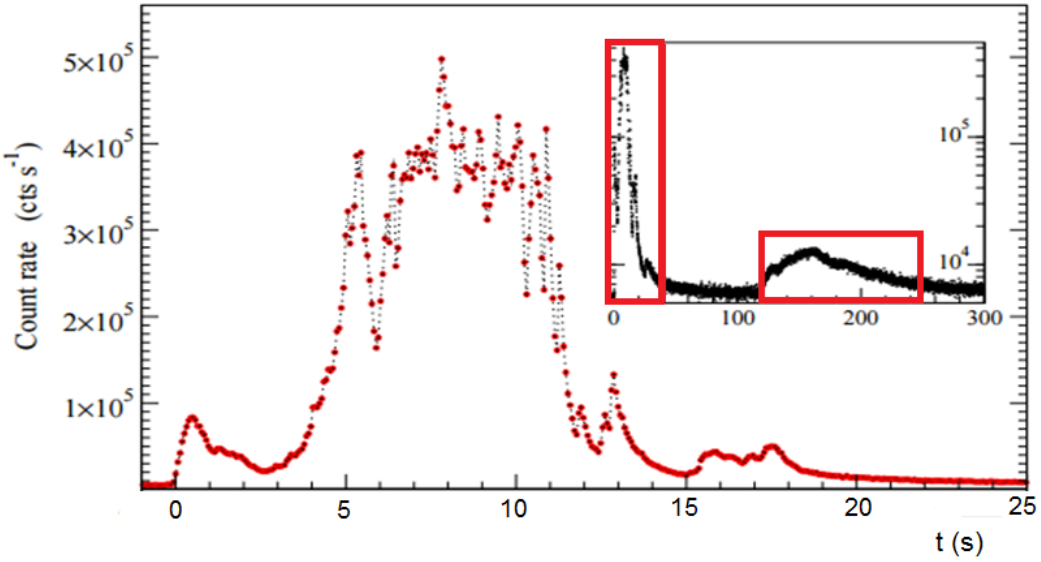

Figure 5.1. Details of the GRB130427A light curve in the 15 to 350 keV band: the central panel shows the first peak of the burst, while the upper insert shows the whole burst, with the red boxes representing the two peaks considered in the *Konus-Wind* Time-Resolved analysis, adopted in this thesis. (Figure from [67]).

Details of these bursts are reported in Table **??**.

Using parameters of Table **??** for the first and second peak, we can compute the NeuCosmA neutrino fluence and compare it to the previously calculated fluence of the whole burst (parameters of Table 3.3). The variability time scale used for both peaks is the same as before, $t_{\rm var} = 0.04$ s: indeed, even if this value is estimated for the first pulse only, it relates to the size of the emitting region, that is unlikely to change during the emission. Results are shown in Figure 5.2 for track-like events.

5.2 First peak analysis

When performing the analysis with the parameters on the first column of Table **??**, different cuts are found with respect to those presented in Table 4.1: they are presented in Table 5.1. For the first peak, the probability to find evidence for an excess in the data at the 3σ level based on the NeuCosmA predictions is maximal when selecting signatures with $\Lambda > -6.2$, while a discovery of 5σ is most probable for $\Lambda > -5.5$.

Table 5.1. First peak analysis: optimised $\Lambda_{\rm cut}$ at the 3σ and 5σ level and the corresponding background and signal rates μ_b and μ_s, the median angular resolution m(α) and the probability MDP to discover an excess as predicted from the NeuCosmA model (see [58]) at the given significance.

σ	$\Lambda_{\rm cut}$	μ_b	$\mu_s^{\rm NeuCosmA}$	$\mu_s^{\rm Guetta}$	m(α)	MDP
5	-5.5	6.74×10^{-5}	1.27×10^{-2}	8.15×10^{-2}	0.28°	1.15×10^{-2}
3	-6.2	4.07×10^{-3}	1.55×10^{-2}	9.94×10^{-2}	0.39°	1.78×10^{-2}

With respect to the search on the whole burst presented in Chapter 4, the number of background events is nearly one order of magnitude less: this is due to the fact that the search has been developed with a smaller time window (22.69 s versus the previous 142.24 s). The reason why the expected number of neutrino events is increased with respect to the previous search is due to the fact that the whole burst analysis was performed on the basis of the *Fermi* parameters of the photon spectrum, while the Time-Resolved analysis is performed

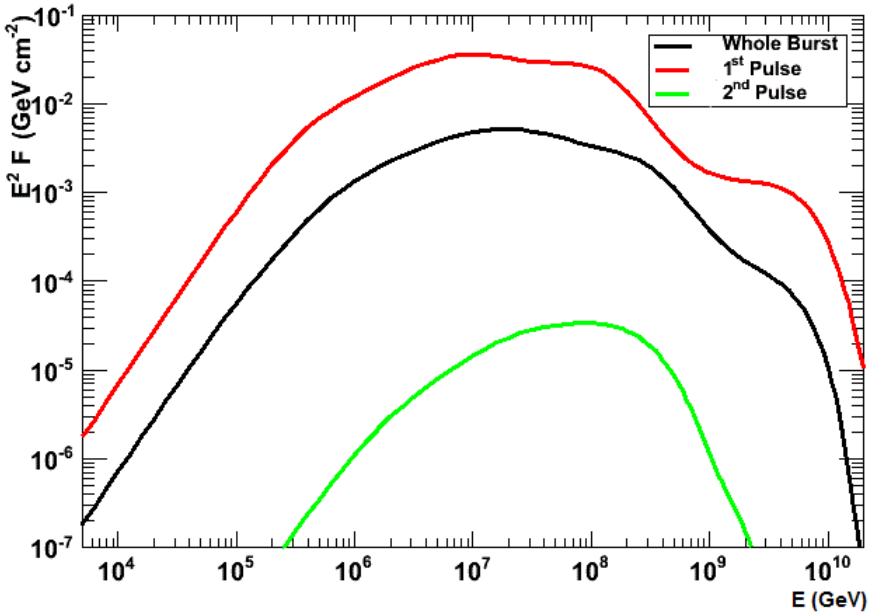

Figure 5.2. GRB130427A Time-Resolved NeuCosmA expectations for tracks: red curve represents the first pulse obtained from *Konus-Wind* gamma information, green the second pulse obtained from *Konus-Wind* gamma information, while black is the whole burst spectrum considered before from *Fermi* gamma information.

with *Konus-Wind* parameters of the gamma spectrum. Because *Konus-Wind* spectral range is greater than the *Fermi* one, the Time-Resolved analysis gives a more realistic estimation of the expected number of neutrino events. Moreover, different input parameters of the gamma spectrum also affect the neutrino yield and the detector PSF. The real gain of this search is the fact that the expected number of signal events exceeds the number of background events: therefore, also the chance to detect the signal at a 3σ level is now about 2%, as Table 5.1 shows, with respect to the previous value of 0.5%, presented in Table 4.1.

5.3 Second peak analysis

Reproducing the analysis with the parameters on the second column of Table **??**, other optimal cuts are found: they are presented in Table 5.2. For the second peak, the probability to find evidence for an excess in the data at the 3σ level based on the NeuCosmA predictions is maximal when selecting signatures with $\Lambda > -6.3$, while a discovery of 5σ is most probable for $\Lambda > -5.3$.

Table 5.2. Second peak analysis: optimised $\Lambda_{\rm cut}$ at the 3σ and 5σ level and the corresponding background and signal rates μ_b and μ_s, the median angular resolution m(α) and the probability MDP to discover an excess as predicted from the NeuCosmA model (see [58]) at the given significance.

σ	$\Lambda_{\rm cut}$	μ_b	$\mu_s^{\rm NeuCosmA}$	$\mu_s^{\rm Guetta}$	m(α)	MDP
5	-5.3	1.29×10^{-4}	1.95×10^{-6}	5.33×10^{-6}	0.25°	2.31×10^{-6}
3	-6.3	3.54×10^{-2}	2.87×10^{-6}	7.67×10^{-6}	0.42°	2.70×10^{-3}

As expected the second peak is of little contribution in terms of neutrino events with respect to the main one: as Table 5.2 shows, the expected number of signal events from the second peak is four order of magnitude less than the one expected from the first peak.
Therefore, the comparison has to be made between the first peak and the whole burst spec-

trum, that is between Table 4.1 and Table 5.1. The Time-Resolved analysis allows to increase the Model Discovery Potential.

After the capability of the analysis was demonstrated using Monte Carlo simulations and pseudo-experiments, it was decided to search the data of GRB130427A with the selection criteria being optimised to find 3σ evidence for a neutrino excess from the first peak. Even if this configuration lowers the detection probability at the 5σ level, it allows at the same time to place more stringent limits in case of a non-detection.

5.4 Results

The unblind ANTARES data were searched for neutrino signatures within the defined first and second peak burst's search windows (see Table **??**), selecting events that fulfilled the reconstruction quality parameters optimised for the detection at the 3σ level (presented in Tables 5.1 and 5.2). No excess over background could be found in the data recorded simultaneously with the prompt GRB emission, both from the first and from the second peak.

When an experiment fails to detect an expected flux, an upper limit on that flux can be derived from the experimental observation: since the absence of a neutrino event correlated in space and time with the GRB occurrence, according to the selected cuts, a 90% confidence level upper limit on the coincident neutrino emission can be placed. This limit can be computed following the bayesian statistical approach. If $\Phi_T(E)$ is the theoretical flux expected from the source, μ_s is the number of expected signal events, μ_b is the number of expected background events and $n_{\rm obs}$ is the number of observed events, the upper limits on the flux at 90% C.L. is computed through the following Equation:

$$\phi^{90\%}(E) = \phi_T(E)\frac{\mu_{90}(n_{\rm obs}, \mu_b)}{\mu_s} \tag{5.1}$$

where $\mu_{90}(n_{\rm obs}, \mu_b)$ is the upper limit on the signal strength. Therefore, an upper limit on the source flux can be found by scaling its predicted flux by the ratio of the signal upper limit to the signal expectation. When a theoretical model predicts a large number of events with very few of them seen, this model will be severely constrained by the experiment. Anyway, the result strictly depends on the analysis that have been developed, because the number of observed events changes according to the chosen quality cuts.

In the bayesian context, the result of the search is given as the pdf of the variable that is being look for, in this case the signal rate. It is first necessary to define the likelihood of the problem $\mathrm{L}(\mu_s|n_{\rm obs})$ and then the Bayes theorem has to be applied in order to evaluate the pdf of the signal rate. Let's start with the simple case of a search where $\mu_b = 0$, μ_b being the expected background; the likelihood, also previously defined in Equation 3.2, is

$$L(n_{\rm obs}|\mu_s) = e^{-\mu_s}\frac{\mu_s^{n_{\rm obs}}}{n_{\rm obs}!}$$

If we count $n_{\rm obs} = 0$ in the defined time search window, then $L(0|\mu_s) = e^{-\mu_s}$. In order to use the Bayes theorem we need to have the prior probability $\pi(\mu_s)$. It is difficult to define in a general sense a non-informative prior: however in this case we assume a prior that is flat for positive values of μ_s and 0 for negative values of μ_s. In this case the Bayes theorem simplifies to:

$$p(\mu_s|0) = \frac{L(0|\mu_s)\pi(\mu_s)}{\int L(0|\mu_s)\pi(\mu_s)d\mu_s}$$

Given a certain probability content (e.g. α=90%) the upper limit μ_s^{up} on the signal will be such that

$$\int_{\mu_s^{up}}^{\infty} p(\mu_s|0)d\mu_s = \int_{\mu_s^{up}}^{\infty} e^{-\mu_s} d\mu_s = e^{-\mu_s^{up}} = 1 - \alpha$$

For $\alpha = 90\%$, we find $\mu_s^{up} \equiv \mu_{90} = 2.3$. The same conclusion applies also if some background events are present, in case a measure results in $n_{\rm obs} = 0$.

The upper limit for the first peak results in

$$E^2 F_\nu \simeq 1 - 10\,\mathrm{GeV/cm^2} \tag{5.2}$$

in the energy range $2 \times 10^5 - 1 \times 10^7$ GeV, as shown in Figure 5.3. The energy range in which the upper limit was derived is chosen as the one where 90% of the signal flux is expected to be detected (therefore, convolving the expected neutrino fluence with the ANTARES effective area). In the most promising case of the first peak, the upper limit results to be about a factor 23 above the expected neutrino flux assuming the Guetta model and 148 assuming NeuCosmA .

For the second peak, instead, this limit is at the level of

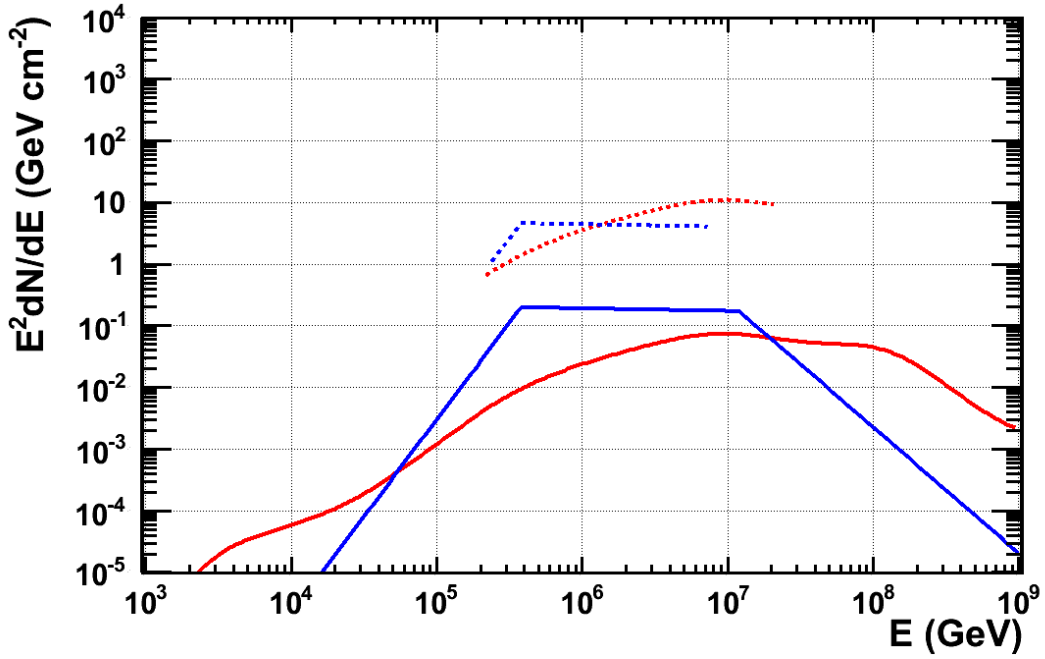

Figure 5.3. Plot of ANTARES 90% C.L. upper limit on the expected neutrino fluence from GRB130427A first peak for track events and Λ cut optimizing the 3σ search ($\Lambda > -6.2$): solid line is for NeuCosmA (red) and Guetta (blue) model, while dashed line is 90% upper limit in the energy range where 90% of the signal flux is expected to be detected.

$$E^2 F_\nu \simeq 1 - 100\,\mathrm{GeV/cm^2} \tag{5.3}$$

in the energy range $5 \times 10^5 - 5 \times 10^7$ GeV. It is about at the same level of the first peak limit, but it is a less stringent limit, since the expected flux from the second peak is much lower than the one from the first peak.

Moreover, no prominent high-energy signature or event multiplet was reported by the TAToO filters during ANTARES data acquisition (see [42]) within two days before and after the burst. Data of the ANTARES detector can therefore only confirm the non-observation of any neutrino signal as announced by IceCube (see [29]).

Having obtained an upper limit on the source flux, it is possible to compare this result with the previous upper limits obtained through the stacking of different GRBs from both ANTARES and IceCube Collaborations. A time-position stacking allows to consider the effect of a whole sample of sources, in order to increase the detection sensitivity through the requirement of a space and time coincidence. The small GRB time and space windows, indeed, along with the low atmospheric neutrino rate, make this a nearly background-free search, with a sensitivity that improves nearly linearly with the number of bursts observed. ANTARES limits were derived for 296 long GRBs occurred between the end of 2007 and 2011, as reported in [80], while IceCube limits were obtained using data from the IC40 and IC59 detector phases from 2008 to 2010 with a sample of 300 long GRBs, as reported in [7]. The ANTARES analysis was optimised for the numerical model NeuCosmA, resulting in an upper limit a factor 50 above the expectations; the IceCube analysis instead relied on the analytical Guetta model, resulting in an upper limit above the realistic scenario depicted through NeuCosmA of a factor 10. These results are reported in Figure 5.4, whose right-hand axis represents the limits translated into limits on the inferred quasi-diffuse neutrino flux limit, through

$$E^2\phi_\nu = E^2 F_\nu \times \frac{1}{4\pi} \times \frac{1}{\mathrm{N_{GRB}}} \times 667\mathrm{y}^{-1} \tag{5.4}$$

with the assumption that the analysed sample represents an average burst distribution and that the annual rate of long bursts is 667 per year (since only long bursts were included in these analyses).
These limits do not yet constrain realistic neutrinos emission models based on an internal shock scenario. Therefore, performing the stacking on the whole ANTARES 2007-2013 sample will allow to further reduce present limits.

The most recent IceCube analysis (see [1]) included a sample of 506 GRBs from 2008 to

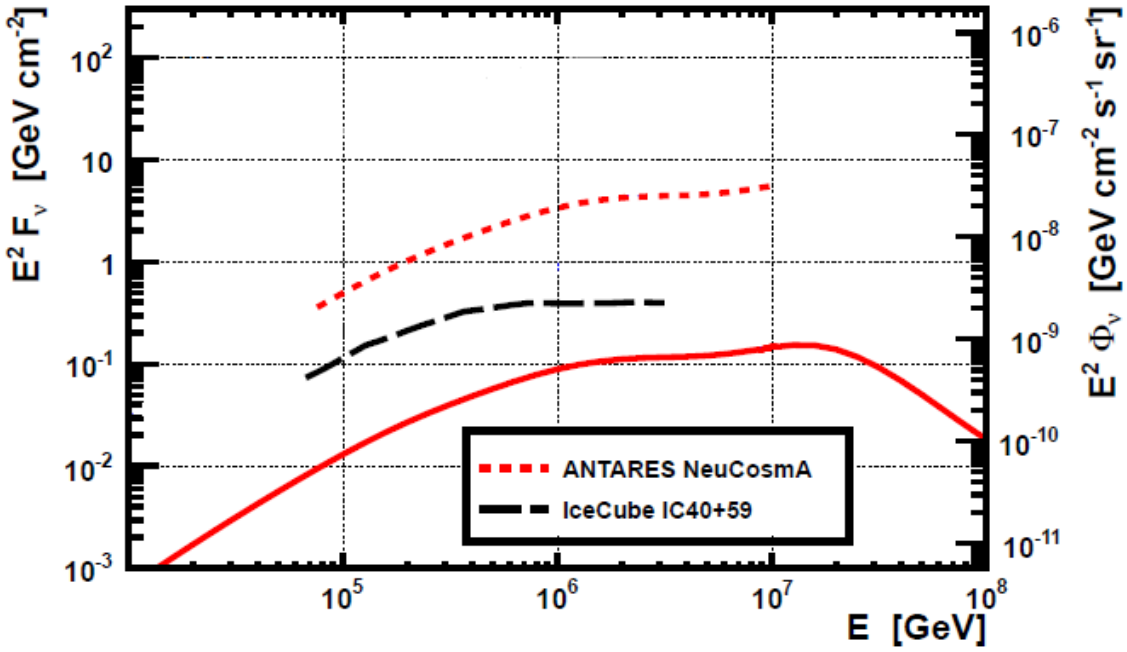

Figure 5.4. ANTARES limits on the sum of 296 GRBs muon neutrino spectra (red dashed line) and their total expected flux (red solid line), from [80]. The IceCube IC40+IC59 limit ([7]) on the neutrino emission from 300 GRBs is also shown in black dashed. The right-hand axis represents an inferred quasi-diffuse neutrino flux limit $E^2\phi_\nu$, computed through Equation 5.4.

2012: a single low-significance (p=0.46) neutrino, compatible with the atmospheric neutrino

background, was found in time-space coincidence with one of the bursts. With this result, IceCube is able to rule out part of the parameter space for f_p and Γ in regions that allow GRBs to be dominant UHECR sources: constraints on these parameters are reported in Figure 5.5, assuming the fireball model. However, these constraints do not account for a possible

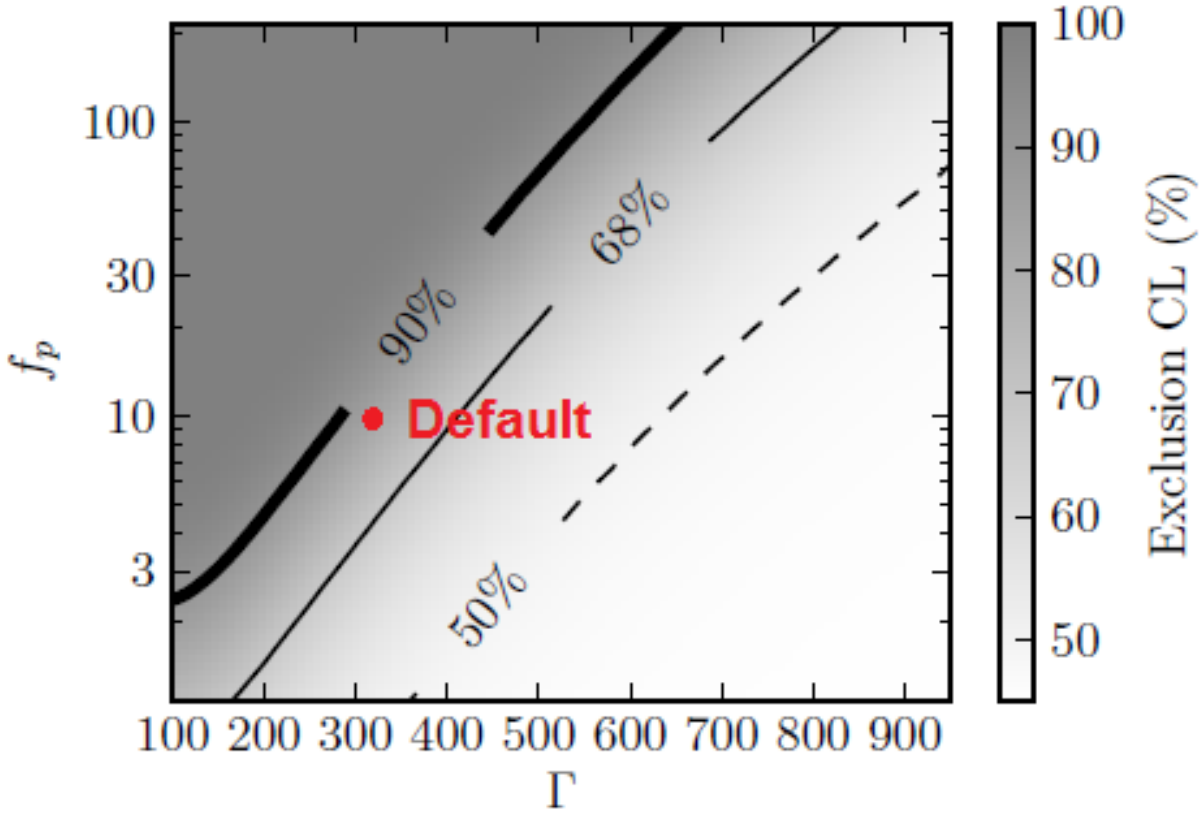

Figure 5.5. IceCube allowed region for the baryonic loading f_p and bulk Lorentz factor Γ under the NeucosmA model assumption (see [57]): as can be seen, default values assumed in this thesis are not yet excluded by IceCube analysis.

enhancement to the high energy neutrinos flux due to acceleration of secondary particles. Note that the parameters assumed in this work ($f_p = 10$ and $\Gamma = 316$) are not excluded by IceCube results, which are beginning to severely constrain the physics of Gamma-Ray Bursts.

5.5 A serendipitous search

Given the fact that no neutrino event has been detected during the first and the second emission episodes of GRB130427A within the ANTARES data, a search can be performed on a wider time window, to look for a precursor signal or a delayed one. Precursor neutrinos can be generated when the expanding fireball is still inside the progenitor star (see [77]): in this case, the accelerated protons interact with matter of the progenitor star or synchrotron photons. However, due to the large optical depth, the synchrotron photons cannot escape the fireball and, hence, no γ signal is observed. The time delay between the start of this neutrino emission and the prompt γ-ray signal is expected to be about 100 s. Another possible interpretation of precursor and delayed neutrinos can be found in Lorentz Invariance violation theories, as proposed by Amelino-Camelia (see [17]).
Because the NeuCosmA numerical calculation adopted during this thesis can only predict the prompt phase flux, a model independent search should be developed, for example re-

lying on the standard E^{-2} flux. Here I present results of a serendipitous search, that has been performed applying the selection criteria of the optimised 3σ search of the first peak, therefore $\Lambda > -6.2$ and $\beta < 1°$. The burst was assumed to have a whole duration like the one measured by *Konus-Wind*, $T90 = 250$ s; the time window is chosen in order to search for coincidences both during the whole burst's duration and 100 s before and after it. This search too gave no signal inside the defined angular and time window.

In the following chapter, I will discuss the detection potential of the KM3NeT telescope for neutrino signals from GRBs, demonstrating that the future telescope will be capable of discovering GRB neutrinos from single bright bursts similar to GRB130427A or put severe constraints on the parameter space upon which the model predictions are based.

Chapter 6

KM3NeT: Towards the Future

So far, having studied the performances of the operational ANTARES detector, the potential of the under construction next-generation neutrino telescope KM3NeT (KM3 stands for km^3, the typical size of the detector, and NeT stands for Neutrino Telescope) to detect high-energy neutrinos associated with Gamma-Ray Bursts will be studied in the following. The future detector will make use of the same detection techniques as the previous in-water experiments ANTARES and BAIKAL, while considerably exceeding the size of the largest currently running neutrino telescope IceCube at the South Pole. The KM3NeT Collaboration includes about 240 people from 42 institutes or universities from 20 different countries, mainly scientists from the old ANTARES, NEMO and NESTOR experiments: a picture of the involved countries is reported in Figure 6.1.

In its final configuration, the experiment will comprise six building blocks of 115 detection

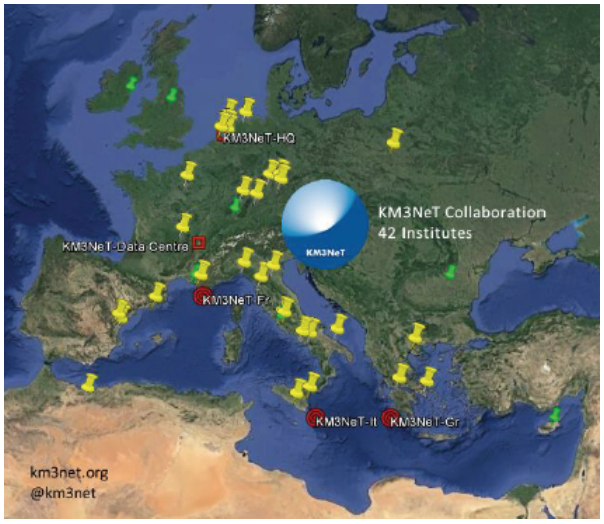

Figure 6.1. Member states of KM3NeT Collaboration.

units (DUs) each, which will be deployed in the Mediterranean Sea. The joined efforts of the ANTARES, NEMO and NESTOR Collaborations addressed the KM3NeT geometrical configuration towards a mixture of the old but improved technologies: the next-generation of neutrino telescopes will be composed of both ANTARES strings and NEMO towers. With respect to strings, towers are optimised for lower energies, having closer floors.

The two main KM3NeT projects are called ARCA & ORCA, standing for Astroparticle and Oscillation ReasearCh in the Abyss. ARCA is the KM3NeT-It project that is going to be deployed in the Italian Capo Passero site, while ORCA is the KM3NeT-Fr project for the French site of Toulon. Both projects are expected to be deployed in their first operational step (Phase1) within 2016. Phase1-ARCA will consist of 24 strings and 8 NEMO-like towers,

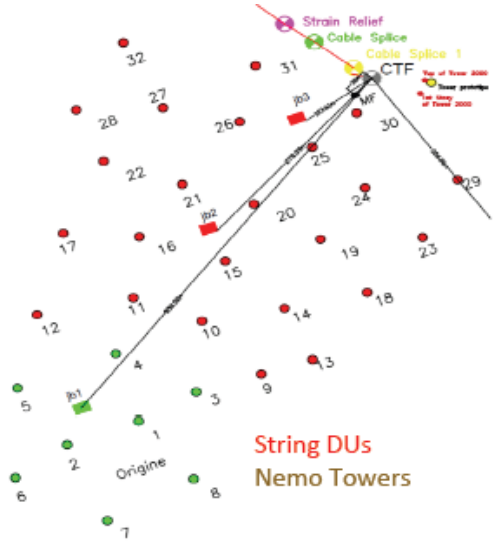

(a) KM3NeT-It footprint: 24 strings and 8 towers are intended to be deployed within 2016.

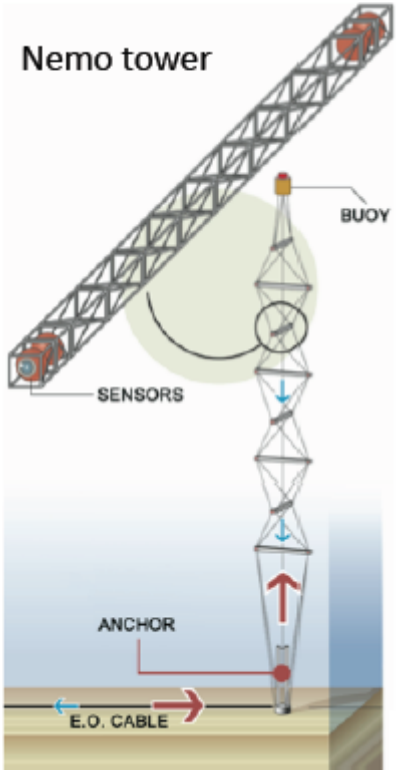

(b) Picture of a NEMO tower, also deployed in KM3NeT-It.

Figure 6.2. KM3NeT-It details.

while Phase1-ORCA will have 7 strings: the footprint of the Phase1 KM3NeT-It project can be seen in Figure 6.2, together with a scheme of the NEMO tower.

DUs will host several Digital Optical Modules (DOM), 17-inch high pressure resistant spheres equipped with 31 3-inch PMTs each, high-voltage bases and digitization electronics: the single DOM is equivalent, in term of photo-cathode area, to 3 ANTARES/IceCube OMs. A photo of a DOM, already tested in Toulon site, is presented in Figure 6.3. The PMTs inside the DOM will be looking from vertically downwards to about 45° upwards. This should substantially facilitate the rejection of the down-going particles background induced by cosmic-ray air showers and the random optical noise in the deep sea. In this way, the expected background in the data will be rejected more efficiently than for example with the ANTARES detector: therefore, KM3NeT will reach a better angular resolution. Moreover, because the PMTs read-out is performed individually, some gains will also come from the improved photo-electrons resolution.
With an instrumented volume of several cubic kilometres ($\sim 5 - 10\text{km}^3$) and a latitude on Earth ensuring optimal visibility of the Milky Way and in particular of the Galactic Centre, the final telescope will be able to confirm the diffuse neutrino flux as reported by IceCube (see [2] and [3]) and allow the Universe to be studied in the light of high-energy neutrinos with unprecedented detail. The efficiency of the planned KM3NeT detector to detect high-energy neutrinos is comprised in its effective area as shown in Figure 6.4. It was derived from Monte Carlo simulations, where the data selection criteria were optimised for the detection of point-like sources with a generic E^{-2} flux, as well as for Figure 2.37.
Note that depending on the final detector configuration, on potential improvements in the reconstruction algorithms and on the data selection of a specific analysis, the effective area

Figure 6.3. A KM3NeT Digital Optical Module: it contains 31 3-inch PMTs, pointing from vertically downwards to 45° upwards.

might change considerably.

The neutrino flux expected from GRBs depends crucially on the attributes of each of them, which are varying considerably from one burst to another. In order to quantify the expected signal that KM3NeT would detect from a burst of similar properties with respect to GRB130427A, the NeuCosmA fluence has to be convolved with the KM3NeT effective area of Figure 6.4: this is needed since the detector's energy domain and responsiveness has to be taken into account. The expected number of neutrinos ν^{exp} can be evaluated according to:

$$\nu^{\text{exp}} = \int dE A_{\text{eff}}(E)\Phi(E) \tag{6.1}$$

where Φ is the tracks flux $(\nu_\mu + \overline{\nu}_\mu + 0.1(\nu_\tau + \overline{\nu}_\tau))$ predicted by the model (NeuCosmA or Guetta), in GeV^{-1} m^{-2} and A_{eff} is the KM3NeT effective area in m^2.

In this way the expected number of muon neutrinos from GRB130427A detectable from KM3NeT is equal to:

$$\begin{aligned} \text{NeuCosmA}: &\quad \nu^{\text{exp}} = 1.02 \times 10^{-1} \\ \text{Guetta}: &\quad \nu^{\text{exp}} = 1.15 \end{aligned} \tag{6.2}$$

This is consistent with previous investigations that had estimated an increase in sensitivity of ∼50 for point-like sources with a generic E^{-2} spectrum with respect to its predecessor (see [59]).
Assuming a Poissonian distribution with mean value equal to this expectation, the probability to detect at least one event for NeuCosmA model with the KM3NeT detector from a burst like GRB130427A is

$$P(n > 1|0.102) = 0.10 \tag{6.3}$$

6.1 Neutrino expectations from Time-Resolved GRB130427A

Now, let's also consider the effects of a TR analysis, introducing the NeuCosmA fluence predicted for the first peak of the burst in Equation 6.1. The result is an expected number of muon neutrinos from the first peak equal to

$$\begin{aligned} \text{NeuCosmA}: &\quad \nu^{\text{exp}}_{\text{1st}} = 0.89 \\ \text{Guetta}: &\quad \nu^{\text{exp}}_{\text{1st}} = 5.44 \end{aligned} \tag{6.4}$$

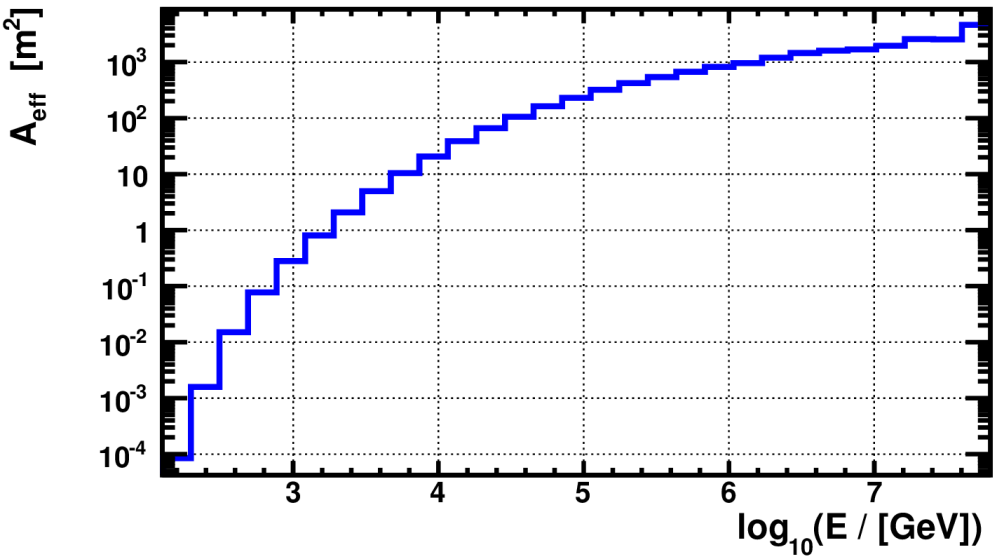

Figure 6.4. Preliminary effective area of the under-construction KM3NeT detector as a function of neutrino energy. Selection criteria are optimised for searches of point-like astrophysical sources emitting a generic E^{-2} spectrum. (Figure from [36]).

while from the second peak equal to

$$\begin{array}{rl} \text{NeuCosmA}: & \nu_{2\text{nd}}^{\text{exp}} = 1.85 \times 10^{-3} \\ \text{Guetta}: & \nu_{2\text{nd}}^{\text{exp}} = 4.61 \times 10^{-3} \end{array} \tag{6.5}$$

Again the first peak gives the main contribution: the Time-Resolved analysis predicts one detectable neutrino signal from the first peak of the burst, assuming NeuCosmA. Its detection chance is

$$P(n > 1|0.89) = 0.59 \tag{6.6}$$

Since this analysis is not optimised for the final configuration of the detector, it can be expected a higher detection probability.

Regardless of the individual GRBs sample for the next-generation neutrino telescopes, KM3NeT will certainly allow the detection of the neutrino flux from GRBs as predicted by state-of-the-art numerical calculations. In the case of a non-observation of such a signal, the parameter space upon which these predictions are based would be severely constrained, putting increasing tension on the hadronic acceleration model within the fireball paradigm.

Chapter 7

Summary and Conclusions

This work has been developed inside the ANTARES Collaboration with the aim of searching for high-energy muon neutrinos coming from Gamma-Ray Bursts: GRBs are short and intense pulses of soft γ-rays, lasting from a fraction of a second to several hundred seconds and coming from cosmological distances. They are most likely associated with the cataclysmic collapse of extremely massive stars or the coalescence of two compact objects into a black hole. Within relativistic outflows of material expelled from a central engine, electrons are thought to be accelerated in internal shocks, which serves to explain the gamma radiation that is observed at Earth. If protons are simultaneously accelerated in these outflows, their interactions with the local photon field would give rise to a flux of neutrinos that would accompany the electromagnetic signal. The first detection of such a signal would unambiguously state that GRBs are hadronic accelerators, a fact that cannot be proven beyond doubt by purely electromagnetic observations. The conclusive identification of astrophysical sources capable of accelerating hadrons to the energies exceeding 10^{18} eV would be essential to explain the puzzling flux of cosmic rays at ultra-high energies.
The already implemented conception of an underwater neutrino telescope has been presented in this thesis: the ANTARES detector is an example of such a technology, being deployed in the Mediterranean Sea. Fully operative since 2008 with twelve vertical lines, its detection principle relies on the physics of interactions between a neutrino and a quark: the production through the NC and the CC channels of charged secondaries, whose relativistic motion in water induces the emission of Cherenkov light, allows to trace this light thanks to a three dimensional array of photomultiplier tubes. The main target of all searches are astrophysical sources: so-called cosmic neutrinos are good messengers to look for, because they are not deflected by magnetic fields in their path from the source to us, so that they directly point to their emitting site; moreover, neutrinos are weakly interacting particles, so they are not absorbed even if travelling across cosmological distances. The expected neutrino flux, in agreement with what is foreseen by several models ($E_\nu^2\phi \simeq 10^{-8}\nu\mathrm{cm}^{-2}\mathrm{s}^{-1}\mathrm{sr}^{-1}\mathrm{GeV}^{-1}$ is the Waxman-Bahcall limit), are so faint to require an instrument with 1-10 km^3 dimensions. ANTARES is optimised for the detection of up-going neutrino events: these are favoured events because they allow to use the Earth as a shield against the large background flux of particles produced by cosmic ray interactions in the atmosphere. Indeed, if the signal is a muon produced by a cosmic muon neutrino, the background is composed of atmospheric muons and muons from atmospheric neutrinos: the first background component is therefore highly reduced when looking for up-going tracks, because up-going atmospheric muons cannot traverse the Earth and reach the detector. The second background component can be discriminated from the signal only through a statistical analysis.
The γ-source studied with this thesis is one of the most ever fluent and relatively close (z=0.34) GRB, called GRB130427A. The assumed neutrino production model is represented by the numerical calculation NeuCosmA, including full photo-hadronic interaction cross-

sections, energy losses of secondary particles and flavor mixing (see Section 1.6): the expected neutrino flux is given for each neutrino family and each weak charge. Because this simulation treats the particle physics governing the radiation processes in greater detail with respect to precedent analytical models, it is expected to predict the neutrino yield from Gamma-Ray Bursts more accurately. For the study of neutrino induced events, both signal and background interactions have been simulated using different event kinematics simulation codes developed within the ANTARES Collaboration for tracks and showers analyses.
Realistic background was estimated from the rate of recorded data over time, which is sensitive to different environmental conditions in the deep sea and consequently accounts for the variation of data-taking efficiency of the detector. The statistical analysis is built in order to maximize the chance of signal detection: a comparison between the expected signal and background Probability Density Functions, obtained considering track events from both $\nu_\mu - \overline{\nu}_\mu$ CC interactions and hadronic showers, is needed in order to discriminate the background only from the signal plus background hypothesis. Therefore, a strategy based on pseudo-experiments, simulating with high statistics a measurement's result, and on the consequent maximization of the Model Discovery Potential based on an extended maximum likelihood ratio is implemented. The time search window corresponds to the burst duration with an extension of 4 s; the angular search cone is centred on the burst's position and has a semi-aperture of 10°. The optimisation affects the tracks reconstruction quality. The expected number of signals from GRB130427A assuming NeuCosmA model is 0.002 at a 3σ level with a detection chance of about 0.5%.
This result can be optimised in the light of a Time-Resolved analysis, which means considering separately the single emission episodes observed during the burst. GRB130427A shows a double peak feature, where the first episode alone includes more than 95% of the γ fluence; therefore the same analysis is applied to each of the bursts. The present work is the first Time-Resolved analysis of GRB130427A. The main prediction from the Time-Resolved analysis consists in an increased discovery potential, thanks to a reduction of the background in the smaller time window. The expected number of signals from the first peak of GRB130427A assuming NeuCosmA model is 0.02 at a 3σ level with a detection chance of about 2%. An increased detection chance by a factor 4 has been achieved. However, no neutrino excess was identified in the ANTARES data within the about 22 s search time window of GRB130427A first peak, hence neutrino emission exceeding 1-10 GeV/cm^2 between $2 \times 10^5 - 1 \times 10^7$ GeV could be excluded with a 90% confidence level. Also no neutrino excess was identified in the second peak search window: in this case the 90% upper limit is less stringent.
The limit from the presented analysis is a factor 150 above the expected flux from GRB130427A: previous ANTARES limits on GRBs fluxes were a factor of 50 above expectations, although these were obtained through the time-position stacking of about 300 sources. Therefore, we expect to further reduce the current upper limit with a final analysis that will include the previous GRBs sample analysed by ANTARES for the years from 2007 to 2011 as well as the 120 GRBs reported in Appendix B.
Besides the Time-Resolved analysis, also a serendipitous search has been accomplished, in order to investigate the presence of a significant excess of precursor or delayed neutrinos, which could be interpreted as a manifestation of Lorentz Invariance violations. Defining a search time window of 100 s before and after the whole burst and using the same quality cuts of the first peak analysis, signals were searched for. No event has been found as well.
A major improvement that could be introduced in the present analysis would be to make use of the information concerning the event's energy. The ANTARES experiment has been designed to detect neutrinos with energies higher than about 100 GeV: due to the fact that the atmospheric neutrino energy is thought to be steeper than the astrophysical one, the astrophysical spectrum is expected to overcome the atmospheric one at energies higher than some TeV, so that improvements are expected from the events classification in energy, that is also expected to lead to a reduction in the number of background events. Energy information

should be therefore included in the PDF.
Moreover, it has been shown as the collection of more data with the under-construction neutrino telescope KM3NeT (see Chapter 6), as well as with a potential extensions of IceCube, will certainly allow the widely established fireball paradigm for Gamma-Ray Bursts to be probed in the near future. Indeed an improvement of a factor of 50 is expected in the number of signal events from a km^3 detector. These detectors constitute the future generation of neutrino telescope and will allow to put more stringent constraints on GRB emission models and on UHECRs origin.
At the moment, IceCube limits on prompt neutrino emission from Gamma-Ray Bursts with second-generation numerical code are such that no more than $\sim 1\%$ of the recently observed astrophysical neutrino flux is thought to be constituted by the prompt emission from GRBs that are potentially observable by existing satellites. In absence of an emerging signal in the coming years, limits from the current and future neutrino detectors will increasingly constrain GRBs as dominant sources of UHECRs.

Appendix A

GENHEN generation weights

Neutrino events simulation is made by GENHEN: as it has been stated in Subsection 2.4.1, GENHEN doesn't generate neutrinos fluxes and then simulate interaction in the detector proximity, as happens in the case of full simulations, but, in order to save calculation time and space on the disk, it simulates directly neutrinos interaction. The output is a neutrino, with energy E, that interacts in a given point (x_0, y_0, z_0) inside the generation volume V_{gen} while travelling in a certain direction (θ_0, ϕ_0). For each neutrino interaction generated, the output also gives the interaction result, that is the particles produced and their kinematics. Finally, GENHEN also attributes to each event two numerical values: a "generation weight" w_2 and a "global weight" w_3. These weights account for the assumption made by GENHEN during the event generation. As stated in [31], for event generation of neutrino interaction flat in cosine of the zenith and flat in $E^{-\gamma}$, w_2 contains

$$w_2 = V_{\text{gen}} I_\theta I_E E^\gamma \sigma(E) \rho N_A P_{\text{Earth}} F \tag{A.1}$$

where

- V_{gen} (m^3) is the can volume;
- I_θ (sr) is the angular phase space factor, that is the solid angle in which neutrinos have been simulated, flat in cosine of the zenith angle:

$$I_\theta = 2\pi(\cos\theta_{\text{max}} - \cos\theta_{\text{min}}) \tag{A.2}$$

- I_E is the energy phase space factor:

$$I_E = \int_{E_{\text{min}}}^{E_{\text{max}}} E^{-\gamma}\, dE = \begin{cases} \frac{E_{\text{max}}^{1-\gamma} - E_{\text{min}}^{1-\gamma}}{1-\gamma} & \text{if} \gamma \neq 1 \\ \ln \frac{E_{\text{max}}}{E_{\text{min}}} & \text{if} \gamma = 1 \end{cases} \tag{A.3}$$

- E^γ takes into account that generation has been done flat in $E^{-\gamma}$; $I_E E^\gamma$ has GeV units;
- $\sigma(E)$ is the total neutrino cross section for neutrino energy E (in m^2);
- P_{Earth} is the probability for neutrino to penetrate the Earth and reach the detector, defined in Equation 2.3; it depends on energy and zenith angle;
- ρN_A is the number of target nucleons per m^3;
- F (s/year) is the number of seconds in a year.

Therefore w_2 has the following units: GeV m^2 sr s/year. It encompasses the ability of the experiment to detect neutrinos of a certain energy and from a certain direction.
The global weight is instead defined as:

$$w_3 = \phi w_2$$

where ϕ is the differential flux of neutrinos before penetrating the Earth in GeV^{-1} m^{-2} sr^{-1} s^{-1}. Therefore, w_3 has the simple unit $year^{-1}$, that can easily be understood as "rate per year". The functional form of the differential flux should be adequately chosen to reproduce the desired situation: $\phi \propto E^{-3}$ for atmospheric neutrinos, $\phi \propto E^{-2}$ for cosmic neutrinos and so on.
Moreover, in data analyses made with RBR simulations, events has to be weighted with the lifetime (in year) of the run and the number of generated events for it, according to:

$$w = w_3 \frac{\text{lifetime}}{N_{\text{gen}}}$$

In the case of the GRBs analysis the differential flux is taken from the numerical integration of NeuCosmA, as a function of neutrino energy: the model was presented in Section 1.6. This model supplies a different fluence for each neutrino type (therefore, six fluences): in this way, a different weight is applied to each of them. To take into account the ν_τ's contribution to track events, the weight to muon neutrino+antineutrino is incremented by a ten percent of the tau neutrino+antineutrino weight, according to:

$$w_{\nu_\mu + \overline{\nu}_\mu} = w_{\nu_\mu} + w_{\overline{\nu}_\mu} + 0.1(w_{\nu_\tau} + w_{\overline{\nu}_\tau})$$

Appendix B

Gamma-Ray Bursts 2012-2013 catalogue

Table B.1. Selected GRBs from *Swift*, *Fermi* and *Konus-Wind* catalogues for the years 2012 and 2013: first column represents the GRB name in the *Fermi* notation of year, month, day and fraction of the day; then the burst's right ascension RA and declination DEC, in degrees, followed by the radial error $\Delta_{\rm err}$ in arcsec; afterwards, the burst's duration $T90$ in seconds, the photons spectral indices α and β with their transition energy E_γ, in KeV; finally fluence F_γ in erg/cm^2 and redshift z.

GRB name (yymmddff)	RA (°)	DEC (°)	$\Delta_{\rm err}$ (arcsec)	$T90$ (s)	α	β	E_γ (keV)	F_γ (erg/cm^2)	z
12010209	276.23	24.71	1.8	28.42	-1.19	-2.19	335.6	1.34×10^{-5}	2.15
12010241	341.15	-23.16	12888	20.22	-1.43	-2.43	354.93	2.55×10^{-6}	2.15
12010738	246.4	-69.93	1800	23.04	-0.99	-1.99	228.59	6.53×10^{-6}	2.15
12011870	124.86	-7.18	78	37.83	-0.91	-1.91	55.65	2.66×10^{-6}	2.94
12011922	139.65	-61.33	7200	41.73	-0.86	-1.86	1171.6	5.94×10^{-6}	2.15
12011935	65.96	-33.92	15912	16.38	-1.08	-2.08	163.54	2.61×10^{-6}	2.15
12012110	235.67	-39.34	28296	18.43	-0.79	-1.79	94.88	1.95×10^{-6}	2.15
12012230	96.58	16.53	9684	16.70	-0.71	-1.71	185.10	2.60×10^{-6}	2.15
12013069	150.04	-17.45	13284	27.78	-0.75	-1.75	82.68	6.61×10^{-6}	2.15
12020381	339.3	-46.59	24372	10.24	-1.27	-2.27	198.18	1.10×10^{-6}	2.15
12020405	292.58	-3.57	3600	49.09	-1.17	-2.75	166.22	9.6×10^{-5}	2.15
12021360	183.49	5.76	15120	13.82	-0.96	-1.96	112.39	2.68×10^{-6}	2.15
12021790	298.73	32.7	5400	2.62	-1.02	-2.02	299.47	4.86×10^{-6}	2.15
12022211	340	-36.41	20520	29.44	-0.98	-1.98	145.01	2.45×10^{-6}	2.15
12022489	331.06	10.18	12924	29.18	-0.95	-1.95	585.65	2.60×10^{-6}	2.15
12030406	127.15	-61.12	3600	9.98	-1.90	-2.90	25.10	5.05×10^{-6}	2.15
12030424	277.28	-46.22	3600	5.38	-0.65	-1.65	1502.03	1.14×10^{-5}	2.15
12031600	57.016	-56.288	2102.4	26.62	-0.82	-1.82	707.86	1.63×10^{-5}	2.15
12032316	211.1	-45.23	13644	4.35	-0.89	-1.89	233.27	1.41×10^{-6}	2.15
12041291	38.91	7.06	10080	101.18	-0.81	-2.12	32.58	7.03×10^{-6}	2.15
12052138	197.016	-52.742	96	91.13	-0.14	-1.14	188.48	3.11×10^{-6}	2.15
12052844	295.13	6.5	21528	16.38	-1.43	-2.43	415.55	3.79×10^{-6}	2.15
12070372	339.356	-29.7244	3.6	8.96	-1.08	-2.08	321.39	8.33×10^{-6}	2.15
12070780	291.06	-34.44	3600	40.96	-1.24	-2.25	98.04	9.36×10^{-5}	2.15
12070988	318.4	-50.1	1656	27.33	-1.11	-2.11	490.54	1.37×10^{-5}	2.15
12071009	120.39	-31.14	17136	131.84	-1.38	-2.38	79.78	5.34×10^{-6}	2.15

Table continues in the next page

Table continues from the previous page

GRB name (yymmddff)	RA (°)	DEC (°)	$\Delta_{\rm err}$ (arcsec)	$T90$ (s)	α	β	E_γ (keV)	F_γ (erg/cm^2)	z
12071111	94.69	-71	158.4	44.03	-0.98	-2.80	1318.66	$1.94 \times 10{-}4$	2.15
12071671	308.23	12.31	15912	234.50	-0.76	-1.84	85.10	1.47×10^{-5}	2.49
12071914	204.29	-43.45	4932	75.01	-0.70	-1.89	88.31	1.35×10^{-5}	2.15
12072768	37.76	16.36	3600	10.50	-1.19	-2.19	87.32	9.23×10^{-6}	2.15
12080192	245.73	-47.37	8604	479.24	-1.13	-2.13	310.88	3.34×10^{-5}	2.15
12080403	233.951	-28.768	60	0.81	-0.89	-1.89	135	1.45×10^{-6}	0.5
12081101	43.658	-31.675	5040	0.45	-0.29	-1.29	1294	2.45×10^{-6}	0.5
12082721	222.74	-71.89	6012	5.06	-0.79	-1.79	577.52	3.37×10^{-6}	2.15
12083021	337.87	-80.04	12456	16.06	-0.76	-1.76	214.83	7.52×10^{-6}	2.15
12083070	110.03	17.53	12204	49.67	-0.99	-1.99	225.76	5.66×10^{-6}	2.15
12090565	355.96	16.99	6480	195.59	-0.25	-2.59	76.8374	1.96×10^{-5}	2.15
12090893	230.64	-25.79	1656	66.95	-0.97	-1.97	220.98	5.16×10^{-6}	2.15
12090907	275.74	-59.45	0	112.07	-0.83	-1.92	195.01	9.85×10^{-6}	3.93
12091126	172.03	-37.51	1080	69	-1.01	-2.72	1200	1.97×10^{-4}	2.15
12091399	213.66	-14.508	60	130.05	-1.07	-1.63	271.87	2.03×10^{-5}	2.15
12091617	205.81	36.66	1080	53.44	-0.98	-1.98	344.10	1.71×10^{-5}	2.15
12091905	298	-38.07	5832	118.02	-0.94	-1.94	280.74	2.07×10^{-5}	2.15
12091930	213.42	-46.31	4032	22.53	-0.78	-2.09	149.39	1.79×10^{-5}	2.15
12092187	96.42	-64.77	11520	5.63	-0.59	-1.59	124.74	2.48×10^{-6}	2.15
12092293	234.75	-20.18	0.36	182.28	-1.58	-2.58	60.35	8.21×10^{-6}	3.1
12092642	59.72	-37.2	13536	60.16	-1.03	-2.03	271.23	4.38×10^{-6}	2.15
12101272	33.42	14.58	24408	0.45	-0.50	-1.50	586.88	1.27×10^{-6}	0.5
12102332	313.86	-4.38	17136	0.51	-0.88	-1.88	1335.68	7.73×10^{-7}	0.5
12102703	4.31	-47.54	9396	166.92	-1.03	-2.03	277.54	7.39×10^{-6}	2.15
12103195	170.772	-3.513	60	242.44	-0.98	-1.98	194.52	1.45×10^{-5}	2.15
12110462	72.14	14.08	14580	59.14	-0.92	-1.92	124.91	4.45×10^{-6}	2.15
12110933	6.84	-42.57	37332	22.14	-0.93	-1.93	360.73	5.34×10^{-6}	2.15
12122191	214.26	33.55	15192	38.91	-1.44	-2.44	103.3	5.04×10^{-6}	2.15
12122329	50.11	21.37	9864	11.01	-0.35	-1.35	133.03	7.02×10^{-6}	2.15
12122541	310.45	-34.83	5400	58.50	-1.23	-2.16	164.47	6.96×10^{-5}	2.15
13010472	174.09	25.92	8784	26.37	-1.40	-2.40	137.73	5.67×10^{-6}	2.15
13010920	17.45	19.24	13392	8.96	-0.95	-1.95	88.52	2.54×10^{-6}	2.15
13011571	171.09	22.62	10008	13.57	-0.78	-1.78	224.41	2.72×10^{-6}	2.15
13011708	341.24	2.81	22212	78.85	-0.78	-1.78	343.54	2.85×10^{-6}	2.15
13012183	211.31	-49.49	4104	178.69	-0.93	-2.17	164.921	4.34×10^{-5}	2.15
13012774	251.05	-17.07	30456	0.45	-0.03	-2.4	700	4.9×10^{-7}	0.5
13013151	189.63	-14.48	3600	147.46	-0.78	-2.45	156.02	3.92×10^{-5}	2.15
13020996	33.59	-27.58	3600	9.92	-0.67	-1.67	176.44	5.90×10^{-6}	2.15
13021506	43.486	13.387	90	143.75	-1.40	-2.40	3368.08	1.86×10^{-5}	0.60
13021826	69.31	-69.13	8208	37.12	-1.46	-2.46	368.72	9.43×10^{-6}	2.15
13022096	306.2	31.74	4104	6.4	-0.84	-1.84	69.90	7.24×10^{-6}	2.15
13022821	240.75	-55.21	4608	15.42	-1.23	-2.23	243.48	1.75×10^{-5}	2.15
13040628	157.78	-62.05	7524	7.94	-0.64	-1.64	84.81	2.92×10^{-6}	2.15
13040633	109.66	-27.86	27576	88.83	-1.25	-2.25	157.67	3.21×10^{-6}	2.15
13042532	18.99	-72.22	10296	66.43	-1.27	-2.27	277.31	4.72×10^{-5}	2.15
13042732	**173.14**	**27.71**	**4.68**	**138.24**	**-0.79**	**-3.06**	**830**	2.46×10^{-3}	**0.34**
13050497	91.63	3.83	4.68	73.22	-1.16	-2.12	538.31	1.29×10^{-4}	2.15

Table continues in the next page

Table continues from the previous page

GRB name (yymmddff)	RA (°)	DEC (°)	$\Delta_{\rm err}$ (arcsec)	$T90$ (s)	α	β	E_γ (keV)	F_γ (erg/cm^2)	z
13050534	137.06	17.49	90	88	-0.69	-2.03	631	3.13×10^{-4}	2.27
13050595	344.47	-70.47	5400	50.24	-0.77	-1.77	1043.96	9.87×10^{-6}	2.15
13051087	105.71	-9.87	17928	29.44	-1.47	-2.47	133.50	3.21×10^{-6}	2.15
13051505	283.436	-54.283	96	0.26	-0.32	-1.32	496.49	1.09×10^{-6}	0.5
13051855	289.72	-4.15	9720	3.46	-0.83	-1.83	980.53	1.76×10^{-6}	2.15
13052319	39.49	-63.07	7668	5.38	-0.30	-1.30	55.22	2.71×10^{-6}	2.15
13061499	324.18	-33.89	4392	9.28	-1.43	-2.43	99.42	6.72×10^{-6}	2.15
13061540	274.96	-68.16	174	304	-0.87	-1.87	33.2	2.1×10^{-6}	2.15
13062261	312.74	24.46	39276	0.96	-0.53	-1.53	174.69	4.32×10^{-7}	0.5
13062348	20.72	-77.78	180	22.22	-1.64	-2.64	36.70	2.46×10^{-6}	2.15
13062659	24.89	4.93	14508	28.16	-1.04	-2.04	106.80	4.82×10^{-6}	2.15
13062853	6.29	-5.07	6156	21.50	-1.38	-2.38	180.24	8.87×10^{-6}	2.15
13070848	17.47	0.003	144	14.08	-1.19	-2.19	132.86	2.53×10^{-6}	2.15
13072058	338.03	-9.4	3600	199.17	-1.16	-2.44	42.49	10.00×10^{-5}	2.15
13072769	330.80	-65.54	2.16	12.99	-1.29	-2.29	173.86	8.16×10^{-6}	2.15
13073024	133.75	-60.36	12384	27.90	-1.12	-2.12	60.17	2.12×10^{-6}	2.15
13080341	220.26	-2.49	4.68	7.62	-1.06	-2.06	143.33	2.82×10^{-6}	2.15
13080402	280.03	-76.15	8208	0.96	-0.73	-1.73	516.31	1.77×10^{-6}	0.5
13081118	192.89	-17.04	12096	44.80	-1.25	-2.25	127.34	6.38×10^{-6}	2.15
13081246	7.41	-79.18	144.7	31.5	-1.33	-2.33	200	1.52×10^{-5}	2.15
13081566	112.37	-2.15	3600	37.89	-0.90	-2.36	82.19	1.18×10^{-5}	2.15
13082167	314.1	-12	360	87.04	-1.07	-2.10	304.67	5.61×10^{-5}	2.15
13082830	259.80	28.22	952.45	136.45	-0.58	-2.21	232.67	3.72×10^{-5}	2.15
13090643	279.39	-53.38	27360	8.19	-0.24	-1.24	294.76	8.24×10^{-7}	2.15
13091917	297.35	-11.73	19152	0.96	-0.55	-1.55	116.32	3.68×10^{-7}	0.5
13091998	242.22	-48.29	32688	17.41	-0.83	-1.83	1315.26	3.36×10^{-6}	2.15
13092853	306.91	-44.19	11736	132.99	-0.64	-1.64	139.15	1.95×10^{-5}	2.15
13100245	75.14	-75.70	72	39.1	-0.36	-1.36	34	6.2×10^{-7}	2.15
13100684	139.36	-0.87	21096	41.98	-0.78	-1.78	423.36	1.84×10^{-6}	2.15
13101174	32.53	-4.41	3.6	77.06	-0.96	-1.96	274.19	8.88×10^{-6}	2.15
13101451	15.05	21.43	24984	30.21	-1.14	-2.14	157.17	1.95×10^{-6}	2.15
13103065	61.45	-62.8	27972	53.25	-1.12	-2.12	175.30	1.65×10^{-6}	2.15
13103148	29.61	-1.58	46.8	7.42	-1.11	-2.11	119.65	4.38×10^{-6}	2.15
13110508	70.97	-63.01	90	112.64	-1.26	-2.26	265.94	2.38×10^{-5}	1.69
13110886	156.50	9.66	1.60	18.50	-1.04	-2.42	239.58	3.53×10^{-5}	2.15
13111037	9.81	8.16	14256	27.33	-0.70	-1.70	138.51	3.27×10^{-6}	2.15
13111348	157.99	-41.52	4356	60.55	-0.56	-1.56	160.55	2.30×10^{-5}	2.15
13111776	213.27	-2.47	7668	93.95	-0.49	-1.49	162.84	1.44×10^{-5}	2.15
13111895	349.86	-66.83	410.04	85.25	-0.82	-1.82	326.92	6.75×10^{-5}	2.15
13112354	53.24	-20.88	30024	3.14	-0.77	-1.77	374.06	4.08×10^{-7}	2.15
13112747	49.4	-5.67	14652	59.65	-0.91	-1.91	131.97	4.27×10^{-6}	2.15
13120290	169.66	21.25	8064	86.02	-1.00	-1.95	21.69	1.24×10^{-5}	2.15
13120493	309.67	-69.67	15912	29.95	-0.38	-1.38	234.59	1.65×10^{-6}	2.15
13120954	136.5	-33.2	3240	13.57	-0.59	-1.59	301.27	1.37×10^{-5}	2.15
13121470	183.94	-6.34	3600	80.07	-1.78	-4.09	267.21	7.22×10^{-5}	2.15
13122927	85.23	-4.40	5.04	12.99	-0.73	-1.73	379.92	2.64×10^{-5}	2.15
13123119	10.59	-1.65	0.30	31.23	-1.21	-2.30	178.15	1.52×10^{-4}	0.64

Table ends from the previous page

Bibliography

[1] Aartsen M.G. et al.(IceCube Collaboration), 2015, E-Print: arXiv 1412.6510v2

[2] Aartsen M.G. et al.(IceCube Collaboration), 2013, Phys. Rev. Lett. 111, 021103

[3] Aartsen M.G. et al.(IceCube Collaboration), 2014, Phys. Rev. Lett. 113, 101101

[4] Abbasi R. et al.(IceCube Collaboration), 2010, ApJ 710, 346

[5] Abbasi R. et al.(IceCube Collaboration), 2011, Phys. Rev. Lett. 106, 14110

[6] Abbasi R. et al.(IceCube Collaboration), 2011, Phys. Rev. D 84, 082001

[7] Abbasi R. et al.(IceCube Collaboration), 2012, Nature 484, 351

[8] Ackermann M. et al.(Fermi Collaboration), E-Print: arXiv 1311.5623v2

[9] Ackermann M. et al.(Fermi Collaboration), 2014, Science 343, 42

[10] Adrian-Martinez S. et al.(ANTARES Collaboration), 2012, ApJ 760, 53

[11] Adrian-Martinez S. et al.(ANTARES Collaboration), 2013, JCAP, 006, E-Print: arXiv 1302.6750

[12] Adrian-Martinez S. et al.(ANTARES Collaboration), E-Print: arXiv 1508.01180

[13] Adrian-Martinez S. et al.(ANTARES Collaboration), 2014, Astrophys. J., Lett. 786, L5

[14] Aglietta M., Badino G., Bologna G., et al., 1987, Europhysics Letters 3, 1315

[15] Aguilar J.A. et al.(ANTARES Collaboration), 2004, Astropart. Phys., Vol. 23, No. 1, 131-155

[16] Aguilar J.A. et al.(ANTARES Collaboration), 2007, Nucl. Instr. and Meth. A, 570, 107

[17] Amelino-Camelia G. et al., 1998, Nature, 393, 763

[18] Amram P. et al.(ANTARES Collaboration), 2003, Astropart. Phys., Vol. 19, No. 2, 253-267

[19] Andres, E. et al., 2000, Astropart. Phys., 13, 1

[20] Antonioli P., Ghetti C., Korolkova E.,Kudryavtsev V. and Sartorelli G., 1997, Astrop. Phys., Vol. 7, No. 4, 357-368

[21] Bailey. D.J.L., 2002, "GENHEN: software documentation", ANTARES Internal Note

[22] Bailey. D.J.L., 2002, "KM3: User Guide", ANTARES Internal Note

[23] Bakker B., Master Thesis at FNWI University of Amsterdam

[24] http://gammaray.nsstc.nasa.gov/batse/grb/skymap/

[25] Barlow R., 1990, Nucl. Instr. Meth. A 297, 496

[26] Barthelmy S.D., Baumgartner W.H., Cummings J.R. et al., 2013, GCN Circular 14470

[27] Bini C., Material of the course "Data analysis for experimental particle physics" at La Sapienza University of Rome, available at http://www.roma1.infn.it/people/bini/

[28] Bionta R.M., Blewitt G., Bratton C.B., et al., 1987, Phys. Rev. Lett. 58, 1494

[29] Blaufuss E., 2013, GCN Circular 14520

[30] Bogazzi C., 2014, Ph.D. Thesis at NIKHEF, Amsterdam, ISBN 978-90-8593-183-6

[31] Brunner J., 1999, "Updated tag list for the new ANTARES event format", ANTARES Internal Note

[32] Bustamante M., Bearwal P. and Winter W., 2013, E-Print: arXiv 1302.6163v2

[33] Bustamante M., Bearwal P., Murase K. and Winter W., 2014, E-Print: arXiv 1409.2874v1

[34] Carminati G., Margiotta A. and Spurio M., 2009, Nuclear Instruments and Methods in Physics Research, A, Vol. 602, No. 1, 95-97

[35] Cavallo G. and Rees M.J., 1978, MNRAS, 183, 359

[36] Coniglione R., 2013, Private Communication, on the estimated KM3NeT effective area.

[37] De Bonis G., PhD Thesis at La Sapienza University of Rome, available at http://www.roma1.infn.it/people/capone/Thesis/Thesis_list.htm

[38] De Jong. M., 2005, "The ANTARES Trigger Software", ANTARES Internal Note

[39] De Jong. M., 2009, "The TriggerEfficiency program", ANTARES Internal Note

[40] Dionisi C., Longo E., Material of the course "Nuclear and subnuclear physics" at La Sapienza University of Rome, available at http://www.roma1.infn.it/people/dionisi/

[41] Domogatsky G.V. et al., 1991, Nucl. Phys. Proc. Suppl., 19, 388

[42] Dornic D. et al.(ANTARES Collaboration), 2011, E-Print: arViv 1110.6809v1

[43] Dornic D., Brunner J., Basa S. et al., 2011, Nucl. Instr. Meth. A 626, 183

[44] Fermani P., PhD Thesis at La Sapienza University of Rome, available at http://www.roma1.infn.it/people/capone/Thesis/Thesis_list.htm

[45] Fermi E., 1949, Physical Review 75, 1169

[46] Ferrari V., Material of the course "Gravitational waves, neutron stars and black holes" at La Sapienza University of Rome, available at http://www.roma1.infn.it/people/ferrari/

[47] Folger F., 2013, "The Dusj shower reconstruction project", ANTARES Internal Note

[48] Gandhi R. et al., 1996, Astropart. Phys., 5, 81-110

[49] Ghisellini G., 2001, E-Print: arXiv astro-ph/0111584v1

[50] Golkhou V.Z., Butler N.R., 2014, E-Print: arXiv 1403.4254v2

[51] Golkhou V.Z., Butler N.R., Littlejohns O.M., 2015, E-Print: arXiv 1501.05948v1

[52] Greisen K., 1966, Phys. Rev. Letters, 16, 748

[53] Guetta D., Hooper D., Alvarez-Muniz J., Halzen F., Reunveni E., 2004, Astropart. Phys. 20, 429

[54] Hanada H. et al., 1998, Nucl. Instr. and Meth. A, 408, 425

[55] Hill G.C., Rawlins K., 2002, E-Print: arXiv astro-ph/020935v1

[56] Hirata K.S., Kajita T., Koshiba M., et al., 1988, Phys. Rev. D 38, 448

[57] Hümmer S., Baerwald P., Winter W., 2012, Phys. Rev. Lett. 108, 231101

[58] Hümmer S., Rüger M., Spanier F., Winter W., 2010, ApJ 721, 630

[59] KM3NeT Consortium 2011, Technical Design Report for a Deep-Sea Research Infrastructure in the Mediterranean Sea Incorporating a Very Large Volume Neutrino Telescope, ISBN 978-90-6488-033-9

[60] Learned J.G., Mannheim K., 2000, Annual Review of Nuclear and Particle Science 50, 679

[61] Levan A.J. et al.(Hubble Collaboration), 2014, E-Print: arXiV 1307.5382v2

[62] Levan A.J., Cenko S.B., Perley D.A., Tanvir N.R., 2013, GCN Circular 14455

[63] `http://lhc.web.cern.ch/lhc/`

[64] `http://www.ligo.caltech.edu/`

[65] Longair M.S., "High Energy Astrophysics", III edition

[66] Markov M.A., Zheleznykh I.M., 1961, Nuclear Physics, 27(3), 385-394

[67] Maselli A. et al.(Swift Collaboration), 2014, E-Print: arXiv 1311.5254v3

[68] Meszaros P., 2006, E-Print: arXiv astro-ph/06052084v5

[69] Mücke A., Engel R., Rachen J.P. et al., 2000, Comput. Phys. Comm. 124, 290

[70] `http://mwmw.gsfc.nasa.gov/`

[71] `http://apod.nasa.gov/htmltest/jbonnell/www/grbhist.html`

[72] `http://nobelprize.org`

[73] Palioselitis D., Ph.D. Thesis at Universiteit Van Amsterdam

[74] Perrina C., Master thesis at La Sapienza University of Rome, available at `http://www.roma1.infn.it/people/capone/Thesis/Thesis_list.htm`

[75] Piran T., 2004, E-Print: arXiv astro-ph/0405503v1

[76] Ramirez H.Y., Ph.D. Thesis at Universitat de Valencia

[77] Razzaque S., Meszaros P. and Waxman E., 2003, Phys. Rev. D, 68, 083001

[78] Salamida F., 2011, Proceedings of the 32nd International Cosmic Ray Conference, vol 2, 146-148

[79] Schmid J. et al.(ANTARES Collaboration), 2013, E-Print: arXiv 1311.4069v1

[80] Schmid J., Ph.D. Thesis at Friedrich-Alexander-Universität Erlangen-Nürnberg available at http://www.ecap.physik.uni-erlangen.de/members/schmid/

[81] Schwetz T., Tortola M., Valle J.F.W., 2010, E-Print: arXiv 0808.2016v3

[82] Sonbas E., MacLachlan G.A., Dhuga K.S., Veres P., Shenoy A., and Ukwatta T.N., 2014, E-Print: arXiv 1408.3042v3

[83] Spurio M. et al.(ANTARES Collaboration), 2014, E-Print: arXiv 1409.4552

[84] Vecchi M., PhD Thesis at La Sapienza University of Rome, available at http://www.roma1.infn.it/people/capone/Thesis/Thesis_list.htm

[85] http://www.virgo.infn.it/

[86] Waxman E., Bahcall J., 1997, Phys. Rev. Lett. 78, 2292

[87] Waxman E., Bahcall J., 1998, E-Print: arXiv hep-ph:9807282v2

[88] Waxman E., 2001, E-Print: arXiv astro-ph/0103186v1

[89] Winter W., 2012, Advances in High Energy Physics, Article ID:586413

[90] Zatsepin, G. T., Kuz'min, V. A., 1966, JEPT Letters, 4, 78

[91] Zhu S., Racusin J., Kocevski D. et al., 2013, GCN Circular 14471

List of Figures

List of Tables

Acknowledgments

I thank Prof. Antonio Capone for his accurate guidance through this work and for the opportunity to take part to the ANTARES working group. I would also like to thank my colleagues Giulia De Bonis, Irene Di Palma, Paolo Fermani and Chiara Perrina for sharing with me their expertise and for their encouragement. I am grateful to the members of the ANTARES Collaboration Bruny Baret, Damien Dornic, Julia Schmid and Damien Turpin for useful discussions and suggestions.

Moreover, this work has been possible thanks to my family, particularly to my mother. And, lastly, a special thank to Francesco Maria Rossi, for his lovely and patient support.

Ringraziamenti

Ringrazio il Professor Antonio Capone per la sua attenta guida nel corso di questo lavoro e per l'opportunità concessami di entrare a far parte della Collaborazione ANTARES. Vorrei inoltre ringraziare i miei colleghi Giulia De Bonis, Irene Di Palma, Paolo Fermani e Chiara Perrina per aver condiviso con me le loro competenze e per il loro incoraggiamento. Sono anche grata a Bruny Baret, Damien Dornic, Julia Schmid e Damien Turpin per le utili discussioni.

Inoltre, questo lavoro è stato possibile grazie alla mia famiglia, in paricolar modo a mia madre. E, infine, un ringraziamento speciale va a Francesco Maria Rossi, per il suo amorevole e paziente supporto.